Proceedings of

MMM
Third International Conference
Multiscale Materials Modeling
September 18-22, 2006, Freiburg, Germany

Symposium 7
Theoretical and experimental investigations of materials with multiple functions

Peter Gumbsch
Editor and Conference Chair

Organized by Fraunhofer-Institute for Mechanics of Materials.
Hosted by University of Freiburg.

IWM
Fraunhofer Institut
Werkstoffmechanik

ALBERT-LUDWIGS-
UNIVERSITÄT FREIBURG

Imprint

Papers published in this volume constitute the proceedings of the Third International Conference on Multiscale Materials Modeling. Papers were selected by the program committee for oral or poster presentation. They are published as submitted, in the interest of timely dissemination.

Contact
Fraunhofer Institute for Mechanics of Materials IWM
Woehlerstraße 11
79108 Freiburg
Germany
Phone + 49 761 5142 0
Fax + 49 761 5142 110

The complete proceedings of the conference are available at

Fraunhofer Information-Centre for Regional Planning and Building Construction IRB
P.O. Box 80 04 69, D-70504 Stuttgart
Nobelstrasse 12, D-70569 Stuttgart
Fon +49 (0) 7 11/9 70-25 00
Fax +49 (0) 7 11/9 70-25 07
E-Mail irb@irb.fraunhofer.de
URL www.irb.fraunhofer.de
ISBN-10: 3-8167-7206-4
ISBN-13: 978-3-8167-7206-4

Foreword

Computational modeling of materials behavior by multiscale materials modeling (MMM) approaches is becoming a reliable tool to underpin scientific investigations and to complement traditional theoretical and experimental approaches of component assessment. At transitional (microstructural) scales continuum approaches begin to break down and atomistic methods reach inherent limitations in time and length scale. Transitional theoretical frameworks and modeling techniques are developed to bridge the gap between the different length scales.

Industrial success in high technology fields relies on the possibility to specifically engineer materials and products with improved performance. The success factor is the ability to make these material related developments timely at relatively low-costs. This demands not only the rapid development of new or improved processing techniques but also better understanding and control of material chemistry, processing, structure, performance, durability, and their relationships. This scenario usually involves multiple length and time scales and multiple processing and performance stages, which are usually only accessible via multi-scale / multi-stage modeling or simulation.

In high-payoff, high-risk technologies such as the design of large structures in the aerospace and nuclear industries, the effects of aging and environment on failure mechanisms cannot be left to conservative approaches. Increasing efforts are now focused on advancing MMM approaches to develop new material systems components and devices. Appropriate validation experiments are crucial to verify that the models predict the correct behavior at each length scale. Thus, one of the advantages of these MMM approaches is that, at each scale, physically meaningful parameters are predicted and used in models for subsequent scales, avoiding the use of empiricism and fitting parameters.

Recent interest in nanotechnology is challenging the scientific community to design nanometer to micrometer size devices for applications in new generations of computers, electronics, photonics or drug delivery systems. These new application areas of multiscale materials modeling require novel and sophisticated science-based approaches for design and performance evaluation. Theory and modeling are playing an increasing role to reduce development costs and manufacturing times. With the sustained progress in computational power and MMM methodologies, new materials and new functionalities are increasingly more likely discovered by MMM approaches than by traditional trial and error approach. This is part of a paradigm shift in modeling, away from reproducing known properties of known materials towards simulating the behavior of hypothetical composites as a forerunner to finding real materials with these novel properties.

The MMM 2006 conference provides an international forum for the scientific advances of multiscale modeling methodologies and their applications.

I would like to thank the members of the international advisory committee, the local program committee and particularly the organizing team, the symposium organizers and the session chairs and the University of Freiburg for their engagement and support. Without their hard work and their devotion of time and ressources, the Third International Conference Multiscale Materials Modeling would not have been possible.

Finally, I would like to thank our conference sponsors for their financial support: The German Research Foundation DFG, Accelrys Inc., Plansee S.E. and the Ministry of Science, Research and Art, Baden-Württemberg.

Peter Gumbsch
Conference Chair

Conference Committee

International Advisory Committee

Prof. Bacon, David	University of Liverpool, UK
Dr. Baskes, Michael	Los Alamos National Laboratory, USA
Prof. Busso, Esteban	Imperial College, London, UK
Prof. Cale, Timothy S.	Rensselaer Polytechnic Institute, Troy, USA
Dr. Diaz de la Rubia, Tomas	Lawrence Livermore National Lab., USA
Prof. Ghoniem, Nasr	University of California, Los Angeles, USA
Prof. Guo, Xiao	Queens College, London, UK
Prof. Iwata, Shuichi	University of Tokyo, Japan
Prof. Kratochvil, Jan	Technical University, Prague, Czech Republic
Prof. Kremer, Kurt	Max Planck Institute, Mainz, Germany
Dr. Kubin, Ladislas	ONERA-LEM, Chatillon, France
Dr. LeSar, Richard	Los Alamos National Laboratory, USA
Prof. Meguid, Shaker	University of Toronto, Canada
Prof. Needleman, Alan	Brown University, Providence, USA
Prof. Odette, Robert	University of California, Santa Barbara, USA
Prof. Ortiz, Michael	California Institute of Technology, USA
Prof. Pettifor, David	Oxford University, UK
Prof. Phillips, Robert	California Institute of Technology, USA
Prof. Raabe, Dierk	Max Planck Institute, Düsseldorf, Germany
Prof. Shibutani, Yoji	Osaka University, Japan
Dr. Soneda, Naoki	Komae Research Laboratory, Tokyo, Japan
Prof. Suresh, Subra	Massachusetts Institute of Technology, USA
Prof. Tomita, Yoshihiro	Kobe University, Japan
Prof. Van der Giessen, Erik	University of Groningen, Netherlands
Prof. Walgraef, Daniel	Free University of Brussels, Belgium
Dr. Wolf, Dieter	Argonne National Laboratory, USA
Prof. Yip, Sidney	Massachusetts Institute of Technology, USA
Dr. Zinkle, Steve	Oak Ridge National Laboratory, USA

Organizing Committee

M. J. Alava	Helsinki University of Technology, Finland
D. Dimiduk	The Ohio State University, USA
M. Dao	Massachusetts Institute of Technology, USA
M. Doi	University of Tokyo, Japan
C. Elsässer	Fraunhofer IWM, Germany
E. v. d Giessen	University of Gronigen, Netherlands
N. Gov	The Weizmann Institute of Science, Israel
H. J. Herrmann	University of Stuttgart, Germany
R. James	University of Minnesota, USA
K. Kremer	Max Planck Institute for Polymer Research, Germany
J. Korvink	IMTEK, University of Freiburg, Germany
J. Li	The Ohio State University, USA
S. Müller	Max Planck Institute for Mathematics in the Sciences, Germany
A. Paxton	Queen’s University, Belfast, UK
M. Payne	University of Cambridge, UK
D. Raabe	Max Planck Institute fuer Eisenforschung, Germany
N. Soneda	Central Research Institute of Electric Power Industry, Japan
M. Zaiser	University of Edinburgh , UK
S. Zapperi	University of Rome, Italy
F. Willaime	Commissariat a l’Energie Atomique (CEA), France
B. Wirth	University of California, Berkely, USA

Contents

Symposium 7

Symposium 7

Theoretical and experimental investigations of materials with multiple functions

A study of the semi-coherent ceramic $SrTiO_3/SrZrO_3$ interface by first-principles DFT calculations

J.M. Albina[1,2], **M. Mrovec**[1,2], **B. Meyer**[3], **C. Elsässer**[1,2]

[1]Fraunhofer Institute for Mechanics of Materials IWM, Wöhlerstr. 11, 79108 Freiburg, Germany; [2]IZBS, University of Karlsruhe, Kaiserstr. 12, 76131 Karlsruhe, Germany; [3]Theoretical Chemistry, Ruhr-University Bochum, 44780 Bochum, Germany

ABSTRACT

First-principles electronic-structure calculations based on the density functional theory and by means of the mixed-basis pseudopotential method were carried out for $SrTiO_3/SrZrO_3$ (001) interfaces. $SrZrO_3$ can be grown epitaxially on a (001)-oriented surface of a $SrTiO_3$ single crystal with a cube-on-cube orientation relationship. The lattice mismatch of 5% between the two perovskites is accommodated by the formation of a square network of misfit dislocations at the interface. In order to estimate the effect of these dislocations on the interface stability with respect to cleavage, we developed a theoretical model for semi-coherent interfaces in ceramics, which is inspired by recent work of Benedek et al. for intermetallics. In this approach the semi-coherent interface with an arbitrary misfit is described as a combination of bits of coherent interfaces, which mimic the local structures present in the coherent regions and at the cores of misfit dislocations. We present results for different geometrical translation states and chemical interface terminations, and we discuss the results in relation to experimental observations by Ernst et al. using high-resolution transmission electron microscopy.

1. Introduction

Ceramic compounds with perovskite-type crystal structures have become important functional components in various modern electronic devices. Understanding the electronic and crystalline structure at interfaces in such materials is a crucial issue for their function, integration and miniaturization. Electronic and structural properties of coherent, i.e., lattice matched interfaces in epitaxial thin-film or multilayer systems can be well predicted by atomistic first-principles computation methods [1]. However, a proper theoretical description of semi-coherent interfaces containing misfit dislocations is still a challenging task because of severe size limitations for atomistic interface models.

Experimental observations of Ernst et al. [2] by high-resolution transmission electron microscopy (HRTEM) of a $SrZrO_3$ (SZO) film grown epitaxially on a $SrTiO_3$ (STO) substrate revealed an atomically sharp interface with a square network of misfit dislocations. The issue we intend to address is how to model such a semi-coherent interface by atomistic first-principles theory. For this purpose we adopt in the following a strategy, which was developed by Benedek et al. for intermetallics [3,4], to semi-coherent STO/SZO interfaces by using a suitable set of atomistic STO/SZO supercell models.

2. Method

Our calculations were performed within the framework of first-principles density-functional theory (DFT) [5,6]. The local density approximation (LDA) was used for exchange and correlation [7]. The self-consistent Kohn-Sham equations for atomistic supercell models with periodic boundary conditions were solved numerically by means of a mixed-basis pseudopotential (MBPP) method [8-12]. Interactions between ionic cores and valence electrons were treated by norm-conserving non-local ionic pseudopotentials [13]. This MBPP approach has been employed, e.g., for twin boundaries in ceramics like $SrTiO_3$ [14] and for metal/ceramic interfaces like $SrTiO_3$/Pd [15]. More computational MBPP details for perovskite interfaces are given in these papers.

3. Semi-coherent STO/SZO Interface

The experimental HRTEM observations indicate atomically sharp interfaces with coherent regions separated every approx. 8 nm by misfit dislocations with pure edge character [2]. From the lattice parameters of STO (expt. 3.905 Å, calc. 3.844Å) and SZO (expt. 4.109 Å, calc. 4.081 Å) it follows that 19 primitive unit cells of SZO match 20 cells of STO to accommodate the misfit. A corresponding atomistic square lattice model of the semi-coherent interface would therefore comprise $20 \times 20 = 400$ unit cells of STO.

While for such a description of this interface the system size is too large for direct first-principles calculation, the atomistic model proposed by Benedek et al. mimics the semi-coherent interface by means of only a small set of representative unit cells. For the STO/SZO interfaces we restricted our model to five representative “key cells” as illustrated in Fig. 1. This strongly simplifies the study of the semi-coherent interface. The model comprises 289 equal key cells located in a coherent region (a), 38 cells at the dislocation core (b), 1 cell where dislocation lines cross each other (c), 68 cells which describe a “transition” between a fully coherent position (a) and a pure dislocation core (b) (d), and finally 4 “corner” cells around the cross point (c) (e), whose energy is estimated as an average of the energies of their eight neighbor cells (“1×a + 4×b + 1×c + 2×d”).

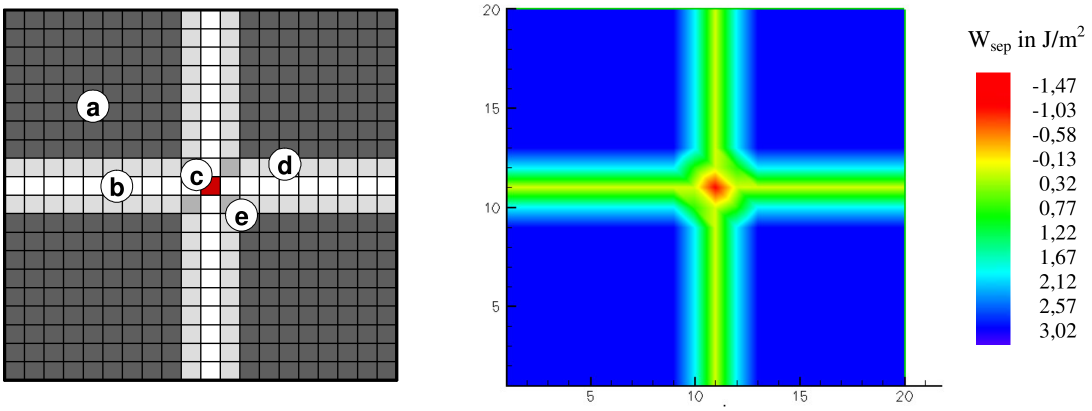

Figure 1. Left: Square-lattice model for the semi-coherent STO/SZO interface. The locations of the five kinds of “key cells” a-e are indicated. Right: Contour plot of the local variation of the interfacial work of separation for the TiO_2/SrO-terminated STO/SZO interface.

For the five kinds of “key cells” a-e the interfacial works of separation W_{sep} were calculated [1] using interface supercells which are illustrated in Fig. 2. The STO/SZO supercells a-c are composed of fourteen atomic layers, i.e. seven alternating layers of SrO and TiO_2 for the STO slab and seven alternating layers of SrO and ZrO_2 for the SZO slab. Fig. 2a and 2b show supercells located in the coherent region (a) and along a misfit dislocation (b), respectively. Fig. 2c depicts the intersection (c) of two dislocation lines. The supercell for the transition (d) from the coherent region (a) to the dislocation core (b) is illustrated in Fig. 2d The layers in this case are piled up with axially more extended lateral displacements, and therefore a larger supercell with sixteen layers was employed. For all supercells the lateral lattice parameter was fixed to the bulk lattice parameter of STO as substrate. The axial lattice parameter was optimized for the coherent "key cell" (a) and then fixed for the other "key cells". Relaxation of all atomic positions was done for all supercells.

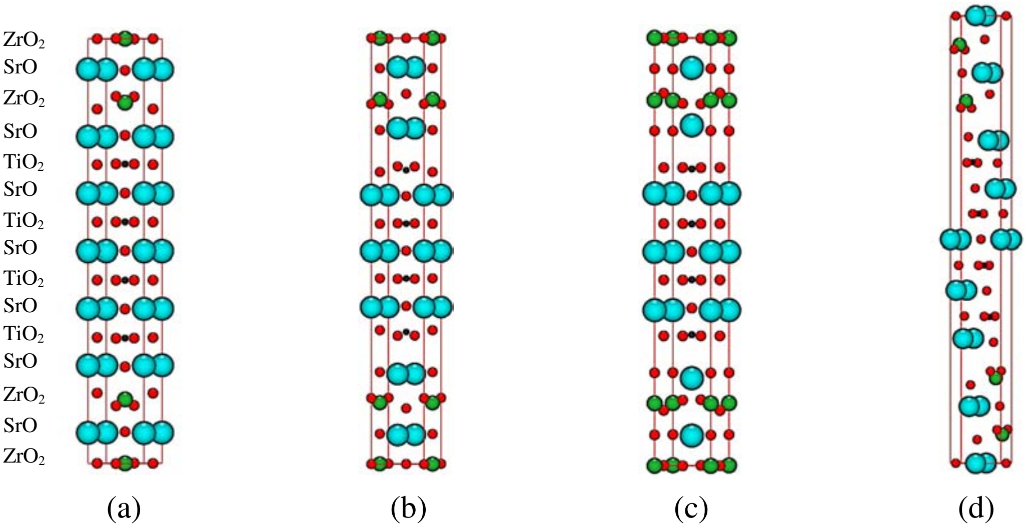

Figure 2. Supercell models for the "key cells" of a TiO_2-SrO termination: (a) coherent region; (b) along the dislocation line; (c) at the intersection of two dislocation lines; (d) the transition between (a) and (b).

Two possible locations for "glide" planes of the misfit dislocations, between terminating TiO_2 of STO and SrO of SZO, and between terminating SrO of STO and ZrO_2 of SZO, respectively, were considered [2]. The resulting calculated W_{sep} for the individual coherent cells (a)-(d) and the estimated W_{sep} for the cell (e) are listed in Table 1 together with the W_{sep} for the two whole semi-coherent interface models, which were estimated as area-weighted average energies according to Fig. 1.

Table 1 Works of separation in J/m^2 for lateral translations (cf. Fig. 1 and 2)

STO/SZO	(a)	(d)	(b)	(c)	(e)	average
TiO_2 - SrO	3,02	1,94	-0,17	-1,47	0,59	2,50
SrO - ZrO_2	1,96	0,95	0,63	-0,99	0,67	1,52

5. Discussion and Conclusion

As expected, the "key cell" located in the coherent region (a) is clearly the most stable one with the highest W_{sep} value. The least stable, even unstable configuration is (c) at the intersection of dislocation lines (c). The cell located at the dislocation core (b) is unstable for a TiO_2-SrO termination and stable for a SrO-ZrO_2 termination. The transition case (d) gives values between the coherent region (a) and the dislocation core (b).

Altogether, the comparison of the W_{sep} for the coherent case (a) as well as the average W_{sep} for the semi-coherent model, which is approx. 20%-25% lower, shows that the more stable interface termination is TiO_2-SrO with approx. 40% higher W_{sep} than SrO-ZrO_2. Our result is therefore in accordance with Ernst et al. [2] who conclude from their HRTEM image analysis that rather a TiO_2 layer terminates the STO substrate crystal than a SrO layer.

In summary, the theoretical model by Benedek et al. for intermetallics [3,4] was extended in our work to investigate by first-principles theory the interfacial stability of the semi-coherent STO/SZO ceramic interface in terms of the work of separation W_{sep} [1]. The present model uses a very narrow stripe for representing the core of misfit dislocations. This is a reasonable first approximation but still not yet like in the experimental HRTEM observations [2]. To become more realistic, the model eventually needs to include some more intermediate key cells to account for the spatial extension of the edge dislocation cores.

Acknowledgements

This work was supported by the German Research Foundation (project El 155/17-1 in the DFG priority program 1157 "Integrated electroceramic functional structures"), and by the European Commission through contract No NMP3-CT-2005-013862 (INCEMS).

References

[1] M.W. Finnis, *The theory of metal-ceramic interfaces*, J. Phys.: Condens. Matter 8 (1996) 5811

[2] F. Ernst, A. Recnik, P. A. Langjahr, P. D. Nellist, M. Rühle, *Atomistic structure of misfit dislocations in $SrZrO_3/SrTiO_3$ interfaces*, Acta mater. 47 (1999) 183-198

[3] R. Benedek, D. N. Seidman, C. Woodward, *The effect of misfit on heterophase interface energies*, J. Phys.: Condensed Matter 14 (2002) 2877

[4] R. Benedek, D. N. Seidman, C. Woodward, *Interface energies for carbide precipitates in TiAl*, Interface Sci. 12 (2004) 57

[5] P. Hohenberg, W. Kohn, *Inhomogeneous electron gas,* Phys. Rev. 136 (1964) B864-B871

[6] W. Kohn, L. J. Sham, *Self-consistent equations including exchange and correlation effects,* Phys. Rev. 140 (1965) A1133-A1138

[7] J. P. Perdew, A. Zunger, *Self-interaction correction to density-functional approximations for many-body systems,* Phys. Rev. B 23 (1981) 5048-5079

[8] C. Elsässer, N. Takeuchi, K. M. Ho, C. T. Chan, P. Braun, M. Fähnle, *Relativistic effects on ground state properties of 4d and 5d transition metals,* J.Phys.: Condens. Matter 2 (1990) 4371-4394

[9] K. M. Ho, C. Elsässer, C. T. Chan, M. Fähnle, *First-principles pseudopotential calculations for hydrogen in 4d transition metals: I. Mixed-basis pseudopotential method for total energies and forces,* J. Phys.: Condens. Matter 4 (1992) 5189-5206

[10] B. Meyer, K. Hummler, C. Elsässer, M. Fähnle, *Reconstruction of the true wavefunctions from the pseudowavefunctions in a crystal and calculation of electric field gradients*, J. Phys.: Condens. Matter 7 (1995) 9201-9217

[11] F. Lechermann, F. Welsch, C. Elsässer, C. Ederer, M. Fähnle, J. M. Sanchez, B. Meyer, *Density-functional study of Fe_3Al: LSDA versus GGA*, Phys. Rev. B 65 (2002) 132104:1-4

[12] B Meyer, F. Lechermann, C. Elsässer, M. Fähnle, *Fortran90 Program for Mixed-Basis Pseudopotential Calculations for Crystals*, Max- Planck-Institut für Metallforschung, Stuttgart

[13] D.Vanderbilt, *Optimally smooth norm-conserving pseudopotentials*, Phys. Rev. B 32 (1985) 8412

[14] S. Hutt, S. Köstlmeier, C. Elsässer, *Density functional study of the $\Sigma 3$ (111) [$1\underline{1}0$] symmetrical tilt grain boundary in $SrTiO_3$,* J. Phys.: Condens. Matter 13 (2001) 9349-9360

[15] T. Ochs, C. Elsässer, *Thin Pd films on $SrTiO_3$ (001) substrates: ab initio local-density-functional theory,* Z. für Metallkd. 93 (2002) 406-416

Atomic Scale Simulation Of Helium Bubble In Aluminum

Ao Bingyun[1], Wang Xiaolin[1], Yang Jianyu[2], Hu Wangyu[2], Xia Jixing[2]
[1]China Academy of Engineering Physics, P. O. Box 919-71, Mianyang 621900, China
[2]Department of Applied Physics, Hunan University, Changsha 410082, Hunan, China

ABSTRACT

We have performed a molecular dynamics (MD) technique to calculate the formation energies of small He_nV_m clusters in Al using embedded atom method (EAM), Baskes-Melius potential and Lennard-Jones potential for describing the interactions of Al-Al, Al-He and He-He, respectively. The binding energies of an interstitial He atom and an isolated vacancy to a He_nV_m cluster are also obtained from the calculated formation energies of the clusters. All the binding energies mainly depend on He-vacancy ratio (n/m) of clusters rather than the clusters size. The results indeed show that He atoms can increase the binding energy of a vacancy to a He_nV_m cluster, and decrease the binding energies of a He atom to the cluster, namely, He atom acts as a catalyst for the formation of He_nV_m clusters.

1. Introduction

The behavior of He in metals is a topic of considerable current interest from both fundamental and technological points of view. The presence of He in the matrix considerably modifies the properties of metals, which has been studied by many researchers [1]. Despite the many years of research regarding He effects with direct and indirect techniques in metals there are still many unknowns, specially regarding the initial stages of nucleation of such defects as bubbles and voids. In terms of Trinkaus's classification of He bubbles by size, the lowest size class is usually indicated by He_nV_m clusters, which may play an important role in the nucleation of He bubbles [2]. Although there are many atomistic studies on small He_nV_m clusters in metals, the atomistic behaviors of the clusters have not been studied in detail [3-5].

In order to obtain further knowledge about the initial stages of He_nV_m cluster or He bubble nucleation in metals, the MD simulations are performed to investigate the behaviors of He_nV_m clusters. The purpose of this paper is to extend these calculations for the formation energies of He_nV_m clusters and investigate the role played by vacancies and He atoms during bubble and void formation in metals.

2. Computational method

The relatively straightforward way to address the atom-level behaviors of He in metals is to use the MD technique. Of critical importance for a successful performance of MD is a precise and computer efficient description of interatomic interactions. For the atomic interaction three potentials are employed in the present calculations. To describe the interaction between Al atoms, a potential based on the EAM is used [6]. The interaction potential for He-He is the Lennard-Jones potential which has been widely used to study the He effects in metals. He-Al potential is obtained by fitting the free-electron He-Al pair potential [7]

3. Results and discussion

3.1 Formation energies of He_nV_m clusters

The formation energies of He_nV_m clusters are the foundation of calculating the defect binding energy. Fig.1 shows the formation energies of He_nV_m clusters are in dependence on number of He atoms. It can be seen that for He in Al, the formation energies of He_nV_m clusters slowly increase with the introducing of He until He to vacancy ratio is greater than 1, which indicates the lowest energy configuration occurs when there is one vacancy per He atom.

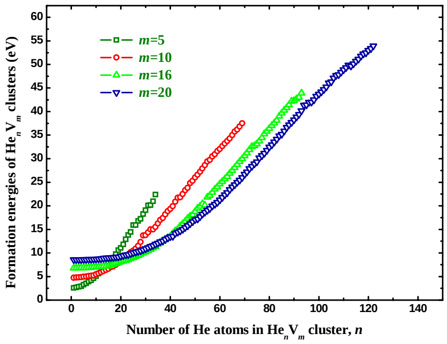

Figure 1. He_nV_m formation energy as a function of the number of He atoms.

3.2 Binding energies of a He atom, an Al atom and a vacancy to He_nV_m clusters

The binding energies of a He atom and a vacancy to a He_nV_m cluster have been calculated. These binding energies are graphed in Figs 2 and 3, respectively. As shown in the two figures, the binding energies show a strong dependence on He density.

He binding energy represents the energy required to bind the *n*th He atom in a He_nV_m cluster. Notes that for the small ratio of He/V the binding energy approximately equals to the formation energy of interstitial He (the energy is 1.25 eV). It shows that He is most strongly bound to the large nearly empty voids, because He exists in a nearly free state. The high binding energies also explain the formation of He bubbles. The binding energy of an interstitial He atom to He_nV_m clusters gradually decreases with increasing He density, followed by an increase at He density greater than 5 He/V. As illuminated by Morishita et al [8], the change in the dependence of the energies on the He density at greater than 5 He/V may be because of the athermal SIAs production and associated effective decrease in the He density. In other words, the collective motion of He atoms in the cluster produces bubble pressure large enough to push the Al atoms off from their normal lattice sites and spontaneously creates addition vacancies and SIAs, therefore increasing the bubble volume and thus lowering the He density. The results indicate that the maximum He/V ratio is about 5. This athermal behavior may effectively increase the number of vacancies in the cluster, consequently, reduce the the actual He density of the cluster.

The binding energy of a vacancy to He$_n$V$_m$ clusters gradually increases with increasing He density, followed by a slowly decrease at high He density greater than 5 He/V, which is consistent with He binding energy curve in Fig. 3, where the dependence of the binding energy on He density changes when the ratio is greater than 5. The calculated binding energy of a vacancy to the high-density He$_n$V$_m$ clusters surprisingly reaches 3.5 eV, suggesting that a vacancy in the He$_n$V$_m$ cluster energetically difficult to be detrapped from the clusters even at high temperature, especially in the cases of n/m greater than 3.

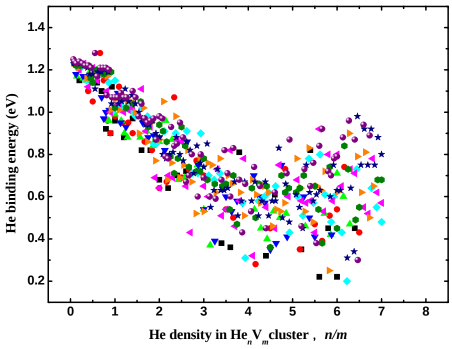

Figure 2. The binding energy of a He atom.

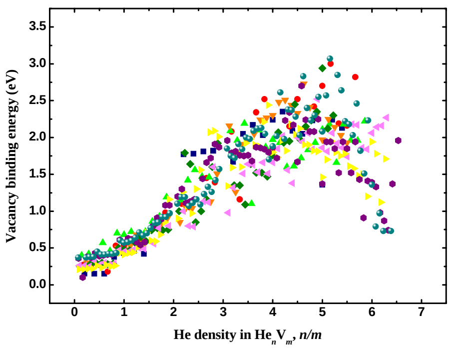

Figure 3. The binding energy of a vacancy.

4. Conclusion

In this paper, the formation energies and the binding energies of He$_n$V$_m$ clusters in Al have been calculated by using MD technique. The main results of these calculations are that the vacancy binding energy increases with the He density, but He binding energies decrease with the He density. All the binding energies mainly depend on the He-vacancy ratio of the clusters rather than the clusters size. From the results we can conclude that He atoms can easily trapped at vacancies which can act as nucleation centers for bubble formation. That is to say, He atoms can stabilize He$_n$V$_m$ clusters.

References

[1] H. Trinkaus and B. N. Singh, J. Nucl. Mater. **323**, 229 (2003).
[2] H. Trinkaus, Radiat. Eff. **78**, 189 (1983).
[3] K. O. Jensen and R. M. Nieminen, Phys. Rev. B **36**, 8219 (1987).
[4] J. M. Cayphas, M. Hou and L. Coheur, J. Nucl. Mater. **246**, 171 (1997).
[5] M. J. Caturla, T. D. de la Rubia and M. Fluss, J. Nucl. Mater. **323**, 163 (2003).
[6] W. Y. Hu, H. Q. Deng, X. J. Yuan and M. Fukumoto, Euro. Phys. J. B **34**, 429 (2003).
[7] M. I. Baskes and C. F. Melius, Phys. Rev. B **20**, 3197 (1979).
[8] K. Morishita, R. Sugano and B. D. Wirth, J. Nucl. Mater. **323**, 243 (2003).

Functionalized molecular monolayers contacted to Silicon surfaces

Fabrizio Cleri[1,2] and Sara Letardi[2]

[1]Institut d'Electronique, Microelectronique et Nqnotechnologie, Université de Science et Technologie de Lille, Av. Poincaré, BP 60069, Villeneuve d'Ascq F59652 , France
(fabrizio.cleri@isen.fr)
[2]Ente Nuove Tecnonogie, Energia e Ambiente, Unità Materiali e Nuove Tecnologie, Centro Ricerche Casaccia, CP 2400, 00100 Roma A.D., Italy
(sara.letardi@casaccia.enea.it)

ABSTRACT

We used a combination of *ab-initio* force relaxation and empirical molecular dynamics simulations, to study the atomic structure of a dense monolayer of benzene-terminated alkyl chains chemisorbed onto the (100) Si surface. We find a transition to a free-rotor phase at about 400 K, with the chains raising to a nearly perpendicular orientation to the surface. At the same temperature, other internal degrees of freedom of the molecules are activated. Above the transition an increase in free-surface roughness is observed..

1. Introduction

Because of their relevance in hybrid organic-inorganic devices, such as OLEDs, molecular electronics and other technological applications, self-assembled monolayers (SAM) are a long-standing subject of intense research in materials science. SAMs are interesting in various fields thanks to the relative ease of assembly of well-ordered and dense layers of alkyl chains of well-controlled length, $(CH_2)_n$, and the possibility of changing basic structural, chemical and electronic properties of the monolayer by changing the functional group attached to the alkyl chain. For example, a simple termination of the alkyl chain with a CH_3 or OH group changes the wetting capability of an alkyl monolayer from hydrophobic to hydrophilic.

In the area of molecular electronics studies, a widely studied class of SAM is the thiol-terminated alkane chains on Au (see e.g. [1-3]). On the other hand, there is an increasing interest about the integration of advanced molecular electronic functionalities with conventional microelectronics, and therefore on the adsorption of SAMs on Si surface.

Although the molecular chains in a SAM show a rather well defined inclination angle with respect to the surface, the atomic scale details of the inclined structure are not known [4,5]. Moreover, a direct experimental information on the individual molecules is extremely difficult to achieve, and the corresponding theoretical treatments of the anchoring of molecules to a metallic or semiconductor surface are far from complete.

For such reasons a longer-term objective of our studies is a comprehensive and in-depth characterization of the interaction between alkyl-based SAMs and Si surfaces. To this purpose, we are carrying out a combined multiscale simulation program, including a combination of *ab-initio* electronic and atomic structure simulations and classical molecular dynamics simulations at finite temperature.

2. Computational details

We choose to simulate a monolayer of duodecyl-phenyl-acetate molecules, $CH_3(CH_2)_{11}COOCH_2$(1,phenyl), adsorbed on the (001) unreconstructed Si surface. This molecule, shortly called DPA, is composed by a fat acid chain (CH_2-CH_3) linked to a phenyl ring by a carboxilic group. The interatomic interactions are taken from the Charmm force field [6], which treats explicitly the non-polar hydrogens.

To obtain the C-Si bonding data, missing from Charmm, we performed a series of *ab-initio* calculations of a periodically repeated supercell containing one DPA molecule and an elementary portion of the (100) Si surface (see Fig. 1a). We used the ABINIT plane-waves DFT code, with Local-density approximation (LDA) and pseudopotentials to describe core electrons. The best compromise for a common set of pseudopotentials for both the Si and the molecule was obtained with the Troullier-Martins soft, norm-conserving scheme for all the elements but hydrogen, written in the Kleinmann-Bylander separable form, and using the Ceperley-Alder LDA functional. For the C-Si bond bending and stretching terms we took the same parameters of the C-C interaction, and rescaled the relevant parameters by the Si/C mass ratio, while using the DFT-calculated values of the equilibrium bond length and bond angle.

The Si surface is composed by 4 (001) layers. Van der Waals interactions between the molecules and the Si surface were include by following the prescription of Ref. [8], i.e., by summing the independent-atom spherical contributions.

The initial configuration of the monolayer on the surface was produced by taking the cubic (001) Si (with 8 atoms) as a unit cell. One DPA molecules was linked to a surface Si atoms, with a 50% site occupation. (Fig. 1a). This planar unit cell is replicated 8x8 times in the x and y direction. The density of molecules on the surface is of one molecule per 29 Å^2, well in the range of the best lipid monolayers obtained by chemical synthesis. To avoid the interaction along *z*, a large void buffer was interposed above and below the SAM+surface system.

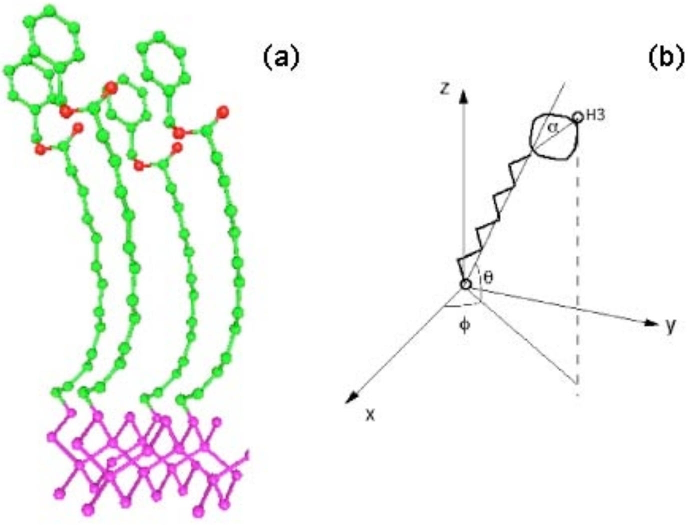

Figure 1 – (a) Schematic of a 2x2 unit cell of the Si(100) surface with 4 DPA molecules attached. Note that the (100) offers 2 sites per unit cell, so this corresponds to 50% occupation. (b) Definition of the structural quantities for a single molecule on substrate.

Electrostatic interactions were simplified by a truncated-and-shifted Coulomb potential, with a 10 Å cut-off. A few runs of comparison with the full Ewald summation of periodic image forces did not gave significant discrepancies with respect to the (simpler and faster) truncated potential approach.

The SAM+Si system was equilibrated by molecular dynamics with a modified version of the DLProtein code, at temperatures between 100 K and 500 K. Each subsequent temperature simulation was restarted from the previous, lower temperature run. At each temperature, the system was initially thermalized by velocity rescaling for 10 ps, under constant-{NVT} conditions. Subsequently, the system was left free to evolve under constant-{NVE} conditions, for about 100 ps. During this second part of the run, thermal-averaged quantities are calculated..

3. Results

We calculated and analyzed a number of structural quantities (see Fig. 1b). The chain inclination, or „tilt“ angle, $\theta' = \pi/2 - \theta$, is the angle formed by the principal axis of inertia of the CH_2-CH_3 chain with respect to the normal to the (001) Si surface. The head inclination angle, α, is the angle formed by the vector C1-H3 with respect to the principal axis of inertia of the CH_2-CH_3 chain (C1 is carbon at the base of the phenyl ring, H3 is the topmost hydrogen atom of the same ring). The precession direction, ϕ, is the angle formed by the projection in the XY plane of the principal axis of inertia of the DPA molecule with respect to the x axis. Finally, the average monolayer height, *d*, is calculated by averaging the time-evolution of the z coordinate of the H3 topmost hydrogen in each phenyl ring.

We find that the average inclination of the molecules on the Si surface (Fig. 2) decreases upon increasing temperature. Similar to the results obtained methyl-terminated alkyl chains [7], up to about T=400 K the tilt angle decreases smoothly, going from $\theta'=38°$ to $\theta'=28°$. In the interval 400-500 K, instead, there is a sharp drop from $\theta'=28°$ to $\theta'=15°$. Above such temperatures, the distribution is also broadened, and a consistent fraction of molecules have inclination angles close to zero.

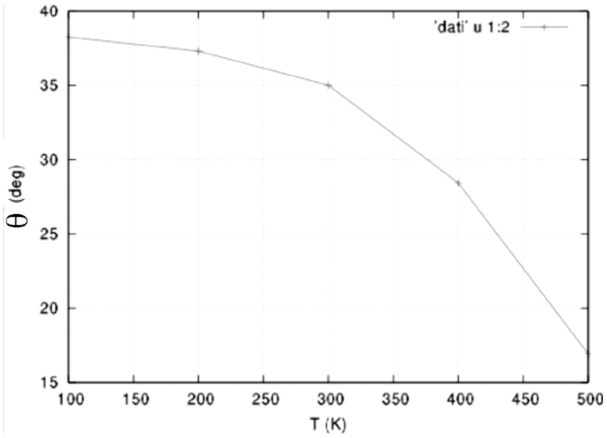

Figure 2 – Average tilt (inclination) angle as a function of temperature.

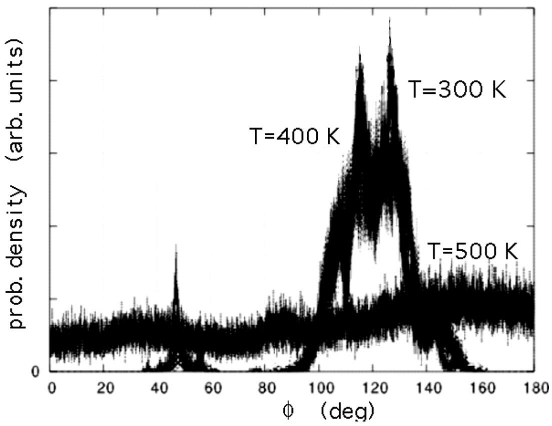

Figure 3 – Probability disribution for the precession angle ϕ at different temperatures.

The precession angle distribution as a function of temperature (Figure 3) shows a well defined value $\phi=110$-$120°$ up to T=400 K, i.e., until the chain inclination θ' is such that steric hindrance between the long, parallel alkyl chains does not allow a free rotation around the principal axis of inertia. At high temperature a few molecules are counter-oriented with respect to the majority, as shown by a small peak around $\phi=50°$. However, when the temperature is raised at 500K, corresponding to the sharp transition to inclination angles of $\theta'=15°$ or less to the surface normal, the DPA molecules are free to spin around the principal axis of inertia, approximately perpendicular to the Si (001) surface, as shown by the flat distribution of tilt angles over the whole $\phi=0°$-$180°$ range.

By analyzing the behavior of the angle α, we find that at any temperature the phenyl head is rather free to rotate around the CH_2-CH_3 backbone, while maintaining a rather constant inclination with respect to the *z* direction. At temperatures above the sharp transition of the inclination angle θ, when the molecule becomes almost perpendicular and free to spin around the *z* axis, also the phenyl head can oscillate more freely. Such a behavior should have a visible effect on the apparent roughness of the DPA monolayer as a function of temperature.

Indeed, the monolayer height appears to increase constantly with temperature and goes smoothly from 21.4 Å at 100 K to 23 Å at 500K. A similar behavior was also registered in previous studies [7,8]. The *d* statistics T>400 K are much more noisy. In other words, the increased mobility of the phenyl heads at higher temperatures does not involve an abrupt change in the average monolayer height, but only a larger dispersion of the roughness values.

4. Conclusions

We carried out molecular dynamics simulations of a fully dense monolayer of phenyl-terminated alkyl chains attached on a Si (001) surface). We studied the temperature dependence of several structural parameters of the monolayer in the range T=100 to 500 K.

We found that the inclination angle of the molecule backbone with respect to the Si surface decreases smoothly at lower temperature, and experiences a sort of phase transition between 400 and 500 K. At such temperatures, the molecules become almost straight with respect to the surface, and appear to spin freely around their major axis. Correspondingly, the phenyl heads, which at any temperature are rather free to rotate around the molecule backbone, increase their mobility by fluctuating also in the z direction. Such a behaviour is reflected also in the surface roughness, which increases as well above T=400K, while the average height of the monolayer does not show discontinuities but increases smoothly.

In the future we aim at obtaining also a better characterization of both the average and pointwise roughness of the top surface of the SAM monolayer, since this could be of great interest for the subsequent process of deposition of metal layers, to form the metallic contacts. Moreover, we are carrying out further MD simulations of incomplete layers, with phenyl coverages going from 50% to 100%. Another important variable in the experiments is the size of the head. In fact, the phenyl termination is only one of the possibilities, other types of p-conjugated heads including thiophene and poly-thiophenes, anthracene, pyrene, and so on. To study extreme cases, we are currently running these same MD simulations with a much bigger termination, such as an anthracene head composed of three adjacent phenyl rings.

Acknowledgements

FC acknowledges support from the ANR-2005 Project MEMO of IEMN-CNRS. FC and SL acknowledge support from the TANO project (L. 295 1997) between STMicroelectronics and ENEA.

References

[1] N. Camillone, T. Y. B. Leung and G. Scoles, Surf. Sci. **373**, 333 (1997).
[2] R. Baathia and B. J . Garrison. Langmuir **13**, 765 (1997); ibid. p. 4038.
[3] S. Letardi and F. Cleri, J. Chem. Phys. **120**, 10062 (2004).
[4] L. Zhang, K. Wesley and S. Jiang, Langmuir **12**, 1227 (1996); Langmuir **17**, 6275 (2001).
[5] D. Kruger, H. Fuchs, R. Rousseau, D. Marx and M. Parrinello, J. Chem. Phys. **115**, 4776 (2001).
[6] A. D. MacKerell et. al., J. Phys. Chem. B **102**, 3586 (1998); A. D. MacKerell and N. Banavali, J. Comp. Chem., **21**, 86 (2000).
[7] S. Vemparala et al., J. Chem. Phys. **121**, 4323 (2004).
[8] L. Zhang et al., J. Chem. Phys. **117**, 1804 (2002).
[9] S. May, Y. Kozlovski, A. Ben-Shaul and M. M. Kozlov, Eur. Phys. J. E **14**, 299 (2004).

Development of a classical force field for the simulation of solvated proteins on oxidised and hydroxylated silicon surfaces

Danny Cole [1], *M. C. Payne* [1], *L. Colombi Ciacchi* [2]

[1] *Department of Physics, Cavendish Laboratory, J J Thomson Avenue, CB3 0HE, Cambridge, United Kingdom*
[2] *Fraunhofer Institute for Mechanics of Materials IWM, Woehlerstraße 11, 79108, Freiburg, Germany*

The key to the successful implantation of Si-based MEMS devices is the surface's ability to induce a positive cellular response when in contact with living tissue. This response is, in turn, regulated by the binding modes of extra-cellular matrix proteins, such as fibronectin, to the surface.

Si is known to form a hydroxylated and partially deprotonated surface in the presence of water. Starting from the structure of the hydroxylated native oxide on Si(001), as obtained in a series of ab-initio molecular dynamics simulations, we have developed a classical force field which describes the structural and electrostatic properties of the oxidised surface in contact with water solutions. The used potential combines a Stillinger-Weber form for bulk-Si with a non-bonded potential originally developed for SiO_2 isomorphs [1], and is able to describe the whole range of Si^{n+} species present in the native oxide layer. The parameters of the potential are fit to reproduce the ab-initio oxide structure. Using this force field, we have simulated the layered structure of water in contact with quartz, amorphous SiO_2, and the native oxide on Si(001). Moreover, we have performed dynamical simulations to investigate the binding mode of a fibronectin unit on the oxidised surface.

[1] P. Vashishta, R.K. Kalia, and J.P. Rino. Phys. Rev. B 41:12197, 1990

Use of Multi-scale modelling to predict the degradation of metals in real environments

Ivan Cole

CSIRO, private bag 33, 3169, Clayton sth MDC, Australia

The degradation of metals in real environments is a complex being controlled by process accross a wide range of scales. A multi-scale model has been developed that looks at processes from the macro (continental) to micron scale. The model defines the production of marine aerosols in the open ocean and on surf beaches and their transport across lanforms, the deposition of aerosols onto structures and components , the physical conditions that pertain on this surfaces (temperature, RH, wetting and presence of salts), the effect of natural processes on cleaning such surfaces and the degradation of the surfaces due to these physical conditions. The model incorporates an understanding of:

i) the role of white caps and the dynamics of breaking surf in controlling areosol formation

ii) The fluid dynamics of aerosol transport and entrapment

iii) The role of air turbulence in controling aerosol deposition

iV) The dynamics of heating and cooling of surfaces

v) The movement of rain drops across metal surafes

vi) The velel of attachment and retention of aerosols

vii) The development of moisture layers

viii) the corrosion processes that occur under moisture layers

The model is presently being extended to include the surface chemical and electrochemical recations that control both the faradaic processes and the precipitation and oxide growth reactions that occur on the surfaces. The model has been used to estimate the degradation and lifetime of infrastructure across Australia and in South-East Asia.

Methodology of thermo-mechanical tests, for the characterization of the stiffness increment of a multilayer piezoelectric actuator under the effect of temperature increment

Louay ELSOUFI [1,2], *Mohamed ZOAETER* [1], *Willy CHARON* [2], *Rémy LACHAT* [2], *Khaled KHALIL* [3]

[1] *Lebanese University, LPM laboratory, Houda building, 3rd floor, Rafik Fattal street, Azmi, 13-5789, Beyrouth, Lebanon*

[2] *University of Technology of Belfort, Montbeliard, M3M laboratory, 90000, Belfort, France*

[3] *Centre Universitaire de Technologie (CUT), 732 Deddeh - Koura, Lebanon*

The smart structures in form of shell will find many applications in the field of transport. Many functional constraints prohibit to control the structure by elements reported on surfaces of the object, the piezoelectric actuators and sensors necessary for the control of the structures will thus be integrated into this one, i.e., in material even the material of the wall. The current development of the integrated smart structures is primarily carried out in supports with thermoset materials, which constitutes an obstacle to their development in the automobile sector where the parameter of recycling is dominating; that is why we propose the use of thermoplastic materials. Unfortunately, the current processes of achieving models in active thermoplastic materials are not directly exploitable for the integration of components fragile and sensitive to the temperature such as the piezoelectric actuators and sensors.

The objective of this work is to propose a thermo-mechanical testing method of characterization of the behavior of a piezoelectric actuator, with the aim of physically interpreting the increase of the stiffness of this actuator with a systematic increase of the temperature, by finite elements modeling using ROBOT Millenium software.

A Multiscale Stability Criterion for Multilattice Crystals

Ryan S. Elliott

University of Minnesota, 110 Union St. S.E., 55455 Minneapolis, USA

The evaluation of crystal structure stability is a critical component of the study of multifunctional materials that exhibit solid-to-solid phase transfor- mations such as shape memory alloys (SMA's). These materials experience an instability that has a characteristic length-scale on the order of the lattice spacing. The remarkable behavior of SMA's (i.e., the shape memory effect and pseudo-elasticity) is the result of the complex interaction between this nanoscopic instability and the material's macroscopic elastic properties. In this work, a crystalline stability criterion is proposed which provides an im- portant new tool for conducting a detailed multiscale investigation of these materials.

The discrete nature of crystalline materials implies that their stability properties are dependent on the length-scale of an applied perturbation. The proposed stability criterion uses a primitive unit-cell description of the multi- lattice crystal to obtain its phonon frequencies as a function of deformation. The transition of one such phonon frequency from a real quantity to a purely imaginary quantity indicates the onset of an instability that results in a change of the crystal's structure. The phonon's wavelength identifies a new length-scale that governs the resulting phase transformation. Special care is taken to correctly evaluate the crystal's stability with respect to uniform (infinite wavelength) perturbations. This requires that perturbations be de- scribed by the Cauchy-Born rule which includes uniform deformations and any coupled internal atomic shifts.

Our, the stability criterion proposed here investigates perturbations of all scales which retain the crystalline nature of the material, that is, per- turbations which take a crystal to another crystal. This technique is ideally suited for use in multiscale modeling methods which rely on some form of the Cauchy-Born Rule, and currently there is an ongoing effort to develop a quasicontinuum (QC) method for complex (multilattice) crystalline materials based on this approach.

Multi-scale Analysis of Portevin-Le Chatelier effect in annealed and solution-treated Al-4%Cu alloys

Jinghong Fan [1,2], *Qingchuan Zhang* [3]

[1] *Alfred University, School of Engineering, Alfred, 14802 New York, USA*
[2] *ChongQing University, RCMM, ChongQing 400044, China*
[3] *University of Science and Technology of China, CAS Key Laboratory of Mechanical Behavior and Design of Materials, Hefei 230027, China*

The experimental findings on the Portevin-Le Chatelier (PLC) effect in annealed and solution-treated Al-4%Cu alloys [1] are discussed from multiscale points of view. By using the MD/GP simulation method, it is found that the aluminum atoms are attracted by the copper atom to formulate a close cluster centered by this solution atom. A micro/mesoscale model based on dislocation pile-ups at the barriers is then developed to describe the stress serration amplitude, frequency and the initiation critical strain of the PLC effects. Furthermore, the PLC band formulation is described by the constitutive equation based on the theory of non-local internal state variables. The across atom/micro/meso/macroscopic analysis offers new insight to the attracting new findings on the PLC effect.

Reference

[1] Huifeng Jiang, Qingchuan Zhang, Xiaoping Wu, Jinghong, Fan, "Spatiotemporal aspects of the Portevin-Le Chatelier effect in annealed and solution-treated Al-4%Cu alloys", Scripta Materialia (in print).

Modelling Ferroic Functional Elements

S. Gemming[1,2], **R. Ermrich**[2], **W. Alsheimer**[2], **G. Seifert**[2]

[1] **Institute of Ion Beam Physics and Materials Research, FZ Rossendorf,**
POB 510119, 01314 Dresden, Germany; s.gemming@fz-rossendorf.de.
[2] **Fachbereich Chemie, Technische Universität Dresden,**
01062 Dresden, Germany.

ABSTRACT

The present study aims at the modelling of an organic field-effect transistor generated by the self-assembly of field-sensitive molecules on the surfaces of ferroic oxides. Electronic-structure-based methods for the microscopic properties of the surface, the molecules, and the respective interactions are combined with classical modelling on the self-assembly of larger adsorbate arrays on a scale-hopping basis.

1. Introduction

Ferroelectric surfaces exhibit a spontaneous net polarisation [1], which has been investigated experimentally by surface-sensitive spectroscopy and theoretically by continuum methods, the Landau-Devonshire approach and shell model studies. This polarisation may be employed for the self-assembly of functional nanostructures and for the switching of these functional elements. The theoretical modelling of such functional elements comprises three key steps:
(A) the determination of structural and electronic properties of the surface,
(B) the tailoring of the adsorbed components for self-assembly and for switching,
(C) the calculation and modification of the device properties.
The present study combines electronic-structure calculations based on the density-functional theory (DFT) with classical Monte-Carlo-Ising (MCI) modelling of the pattern formation on defective two-dimensional lattices. Full DFT and time-dependent DFT-based tight-binding (DF-TB) calculations provide information on the local electric field on-top of a stepped oxide (A) and on the influence of such fields on the optical absorption of organic molecules (B) in sections 2. and 3. The local interaction strengths enter into a classical Ising Hamiltonian with anisotropic coupling constants across the step edge and on-site Schwoebel barrier contributions at the sites adjacent to the step edge to address the key step (C) in section 5. In this way, the properties of an array of prototypical organic field effect transistors shall be explored, which contain a field-sensitive organic molecule as switchable element and the spontaneous surface polarisation of a ferroic substrate is employed for switching.

2. Stepped $BaTiO_3$ surfaces

The ground-state geometries and electronic structures of the substrate, the vici-

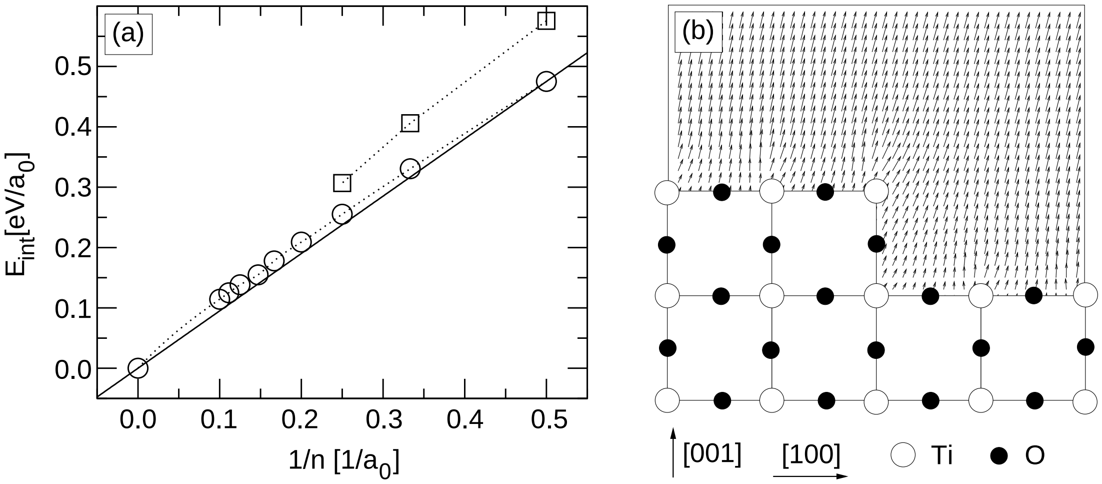

Figure 1: Panel (a): Step interaction energy E_int in eV/a_0 as a function of the inverse step distance in 1/a_0, where a_0 is the $BaTiO_3$ lattice constant (circles: DF-TB, squares: DFT). Panel (b): Electric field [10^9 V/m] above the (401) surface.

nal, stepped $BaTiO_3(n01)$ surfaces ($n = 0$ to 4) were investigated by local density-functional band-structure calculations [2] with the program package ABINIT [3] and extended to larger system sizes up to n = 10 with the density-functional-based tight binding method[3]. Norm-conserving pseudopotentials, a plane-wave basis (E_{cut} = 823 eV) in the DFT calculations, and a local basis set for the tight-binding approach were employed. The Monkhorst-Pack k-point sampling of the surface supercells was chosen to be compatible with the 12 × 12 × 12 mesh of the bulk oxide (56 k-points). The electric field above the surface was obtained by solving Poisson's equation for the calculated charge distribution numerically on a dense mesh.

The interaction energy E_{int} between adjacent steps was calculated as difference of the total energies of the stepped system and stoichiometric amounts of the planar $BaTiO_3(001)$ surface and TiO_2 in the rutile phase as $E_{int} = E_{step} - nE_{surf} - E_{TiO2}$. Fig. 1(a) depicts E_{int} as a function of the vicinal index n of the $BaTiO_3(n01)$ surface. The reciprocal value of n is used here, because the long-range elastic interactions between 1D defects, e.g. dislocation lines, decays proportional to the inverse distance of the defects. The nearly constant slope of the E_{int} curve suggests, that also adjacent steps experience predominantly long-range elastic interactions. In the limit of infinitely large terraces E_{step} approaches nE_{surf}, and E_{int} converges to zero. Fig. 1(b) depicts the electric field above a $BaTiO_3(401)$ surface, in a (010) cut plane through Ti and O atoms. Directly at the step edge the unscreened electric field reaches values of 10^9 V/m and changes direction such that the major component is perpendicular to the surface. From about 5 Åon the local field changes even out, and the far-field is perpendicular to the nominal surface plane (401). Thus, the local changes of the electric field become important at typical adsorbate-substrate distances of 2 to 4 Å, and the step is a promising candidate for guiding self-assembly and switching. The goal for step B is to explore molecules, which exhibit a change of the electronic properties at an external field strength of up to 10^9 V/m.

3. Oligothiophenes - tunable field-sensitive molecules

Conjugated organic polymers such as the α-oligothiophenes investigated here are promising candidates, because they exhibit a polarisable aromatic π-electron system, which can undergo electronic transitions in the optical spectral range. For this reason they have already a high application potential in organic transistors, batteries, LEDs, sensors, or optical switches. In order to assess their potential as gate element in the presently suggested O-FET device, the change of the excitation energies ω_I in an external electric field was calculated with the time-dependent version of the DF-TB method [3] for the six smallest members of the oligothiophene series.

The left panel of Fig. 2 shows the change of the excitation energy of the thiophene monomer in an external electric field parallel (E_x,E_y) or perpendicular (E_z) to the plane of the molecule. The solid curves are obtained from TD-RDFTB calculations, the dashed reference curve is the HOMO-LUMO difference in a field E_z calculated by a full DFT formalism [3]. The strongest field sensitivity is obtained with an external field E_x perpendicular to the dipole moment of the molecule. The excitation energy ω_I exhibits a clear minimum at an electric field of 2.5 10^{11} V/m along E_x, and then increases again to values even higher than the zero-field excitation energy. Since the estimated maximum of the unscreened electric field above a stepped $BaTiO_3$ surface is of the order of 10^9 to 10^{10} V/m, only the initial negative slope and the red-shifted part of this curve are of interest in the present context. An even smaller red-shift is obtained if the electric field is directed along the short extension of the molecule, E_y. For E_z the minimal basis employed in the TD-RDFTB scheme does not allow for a polarisation of the orbitals perpendicular to the molecular plane. However, the full DFT reference curve indicates that the red shift along E_z is smaller than for E_x for the small field strengths discussed here. On the whole, the thiophene monomer is not sensitive enough towards the small external electric field at a ferroic surface to be an optimal candidate for an O-FET gate element.

A stronger sensitivity is obtained for the higher members of the oligothiophene series, shown in Fig. 2(b). With increasing chain length the excitation energy ω_I shifts to lower values already at zero external field. Thus it is possible to tune the colour of the oligothiophenes by varying the number of monomers. Again, the strongest changes of the ω_I values occur, if the external electric field is aligned parallel to the chain direction (E_x) as shown in Fig. 2. From bithiophene on, the higher density of states in the HOMO and LUMO regions of the spectrum provides more than one transition channel, and a non-linear dependence between the excitation energy and the field strength is obtained. Hence, the curve of $\omega_I(E)$ exhibits several local extrema at energies, which depend on the chain length. The effects are two-fold: first, an enhanced slope at the curve onset is obtained, which implies a hence to a better sensitivity towards small field changes than the one obtained for the monomer. Therefore, at the typical field strength at an unscreened ferroic surface (up to 10^9 V/m) especially the longer oligomers promise a good applicability in the device. Second, an additional, sharp local minimum of the excitation energy at low fields E_x occurs, which suggests, that the longer oligothiophenes may also be employed as bistable switches at higher field strengths.

4. Self-organized coverage of stepped surfaces

For a bottom-up generation of O-FET arrays a self-assembly process of the switchable molecules on the ferroic surface is suggested, which employs steps, the typical surface defects on ferroic oxides, as template. Hence, the coverage of stepped $BaTiO_3$ surfaces with organic molecules was simulated with an Ising Hamiltonian on a periodically repeated 2D square lattice with a straight step. The spin-up / spin-down states correspond to the presence / absence of an adsorbate. The interactions between neighboring and next-neighbouring adsorbates are described by the coupling constants J_{12} and J_{13}, and across the step the coupling constants are scaled geometrically (J'_{12} and J'_{13}). The adsorbate-substrate interaction is modeled with an on-site term H. Adjacent to the step this term is augmented by a Schwoebel barrier, $H_s > 0$, which is attractive along the step and repulsive on-top of the edge:

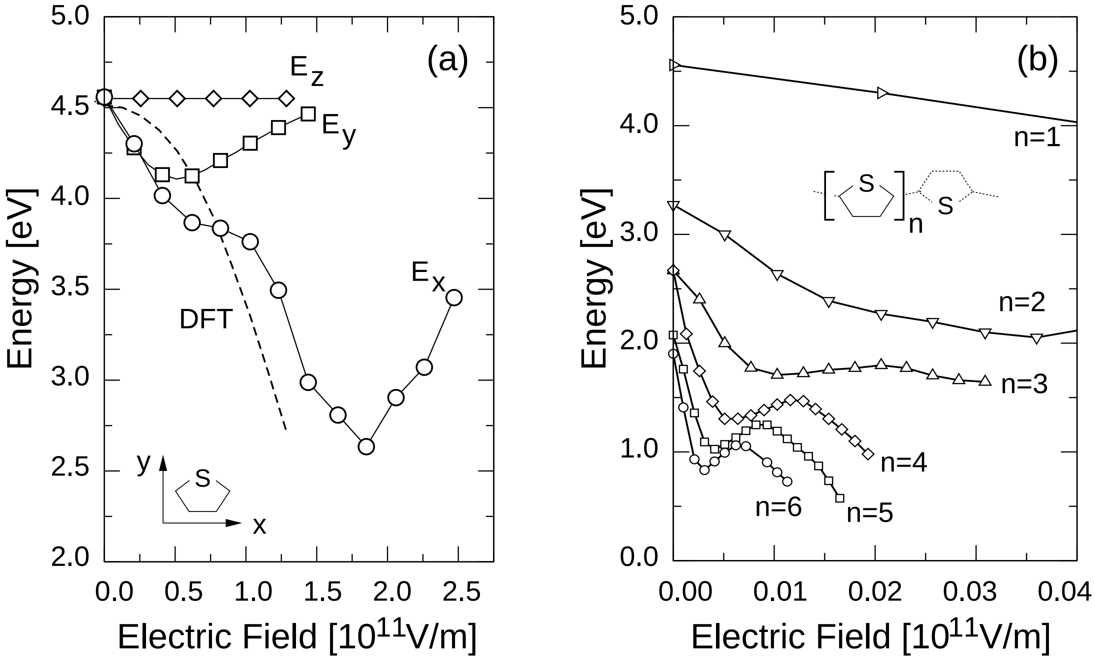

Figure 2: Change of the optical properties of oligothiophene molecules in an applied external electric field. Panel (a) depicts the excitation energy ω_I of the thiophene monomer as a function of the field strength applied in the three high-symmetry directions. Panel (b) gives a comparison of ω_I as a function of E_x for the first six members of the polythiophene series.

$$\mathrm{H} = \sum_{i,j} J_{ij} s_i s_j + \sum_{i',j'} J'_{i'j'} s_{i'} s_{j'} + \sum_{i',j} J s_{i'} s_j + \sum_{i} H s_i + \sum_{i'} (H \pm H_s) s_{i'}, \qquad (1)$$

where i sums over terrace sites, i' over step sites, j over neighbours with regular couplings J_{ij} and j' over neighbours with coupling J'_{ij}. This modified two-dimensional Ising model has been solved numerically with the standard Metropolis scheme for prototypical values of the coupling constants and the adsorbate-substrate interaction [4]. A systematic study was carried out to analyse the interplay of the different parameters of the MCI model concerning the criticality of the order-disorder transition, and to assess the resulting adsorption patterns on the surface. The major part of the simulations were carried out on a quadratic grid with a size of $N^2 = 2500$ sites, but also grids with $N = 20, 100,$ and 200 were employed to investigate final-size effects. The cluster sizes were evaluated with the help of the Hoshen-Kopelman cluster recognition algorithm [5], and the cluster size distribution statistics was determined from averaging over 2.5 10^5 to 5 10^5 Monte-Carlo steps, which corresponds to at least 100 spin flips per site.

Starting from the standard two-dimensional Ising model the additional terms were added successively. For the standard two-dimensional square lattice with nearest neighbour interactions J_{12} and the on-site term H the Onsager solution for the critical transition temperature $T_c = 2.329 k_B^{-1}$ [6] and the well-established scaling laws were reproduced [6]. The inclusion of next nearest neighbour interactions J_{13} only changes the absolute value of T_c, but not the scaling behaviour. Also the geometrical scaling of J_{12} and J_{13} at the step edge has no influence on the scaling behaviour of the order-disorder transition. As described in more detail in [7] only the local modification of H by the Schwoebel barrier induces a second, low-temperature order-disorder transition, where the anti-parallel ordering of the occupancies in the vicinity of the step prevails over the regular low-temperature ordering, which leads to complete coverage on the non-defective substrate.

Fig. 3 (a) shows the typical cluster size distributions of the standard 2D Ising model (only $J_{12} = 1$) as a function of the temperature for a model system with 50 × 50

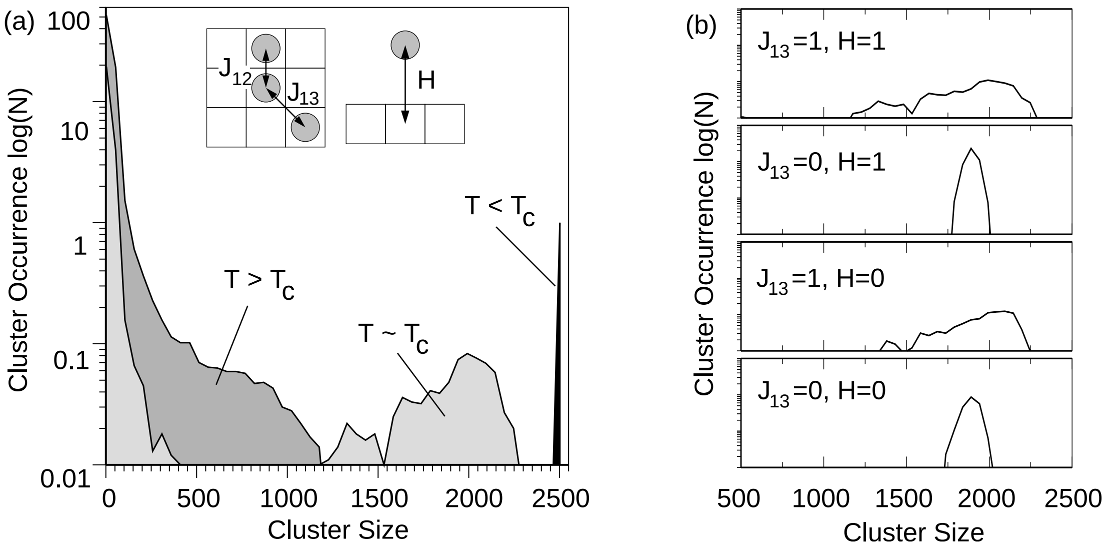

Figure 3: Cluster size distribution (a) for the standard 2D Ising model on a square lattice at temperatures $T = 0.1T_c$ (black), $T = T_c$ (dark gray), $T = 2T_c$ (light gray), (b) for the stepped system at $T = T_c$ and different combinations of J_{13} and H.

sites. To better visualise the distribution of the more rarely occurring big clusters the cluster size is given on a logarithmic scale. At a low temperature of $T \approx 0.1T_c$ one big cluster covers the whole substrate (Fig. 3, black shaded peak at cluster size 2500). At an elevated temperature of $T \approx 2T_c$ very small clusters and predominantly monomers are obtained (Fig. 3 , area shaded in light grey). Only for temperature values close to T_c intermediate cluster sizes are observed together with a large number of monomers (Fig. 3, area shaded in grey). The most common large cluster encloses an area A of roughly 80% of all sites (2250 sites), and the width w of the corresponding peak of the distribution amounts to ±8%. This finding leads to the conclusion that self-organisation, ripening, and coarsening processes may be employed for the formation of nanostructured thin films, if the temperature can be kept close to the critical ordering temperature.

As discussed in detail in ref. [8] for the planar, non-stepped surface, the additional lateral and vertical interactions were introduced in a stepwise manner, and the effect on the critical order-disorder temperature and the cluster size distribution was monitored. The additional lateral interactions J_{13} with the diagonally distant next-nearest neighbours cause an increase of the value of T_c. This finding reflects the stronger bonding within the cluster which counteracts the order-disorder-transition. Similarly, for an enhanced substrate interaction H the transition temperature increases, and if both ordering factors $J_1$3 and H are included, the critical transition temperature is even further increased, again reflecting a stronger tendency of the adsorbate system to form ordered clusters. However, the transition type changes from second-order to first-order, when $H \neq 0$. Large, well-ordered adsorbate clusters cover up to 90% of the substrate even at elevated temperature, if either the lateral interactions or the vertical adsorbate-substrate attractions dominate the system. If lateral and vertical interactions compete even more cluster seeds are pinned. This leads to the formation of more, but smaller clusters with a bimodal, broad cluster size distribution and optimum cluster sizes of 70% and 88% surface coverage in the critical temperature regime close to T_c.

The presence of a surface step between two terraces modifies these findings slightly, because the local modifications of J_{ij} and H in the vicinity of the step can act as additional cluster seed. Already for the simplest model with only J_{12} interactions, the maximum size of the large clusters is increased to $A = 88\%$ with a small distribution width of $w \approx \pm 4\%$. T_c, on the other hand, is only slightly decreased as a finite-size effect and tends towards the value of the planar system in the limit of infinitely large terraces. Thus, the step acts as an ordering element, which is similar to the joint presence of J_{13} and H in the planar system, but at a considerably lower temperature. If either J_{13} or H are introduced in the MCI model, the same competition between pinning at the step and pinning due to enhanced lateral or vertical interactions is observed as the one discussed above. In both cases the maximum of the most prominent peak of the cluster size distribution is shifted to a smaller covered area A, and additional peaks with lower intensity occur. For the inclusion of J_{13}, the ideal large cluster size is $A_1 = 70 \pm 4\%$, flanked by two narrower peaks at $A_2 = 52 \pm 2\%$ and $A_3 = 82 \pm 2\%$. If only H is added as above, again a peak triplet is obtained with a ideal cluster size of $A_1 = 82 \pm 4\%$, and two narrower peaks at $A_2 = 70 \pm 2\%$ and $A_3 = 90 \pm 2\%$. Although of equal magnitude, the lateral interaction J_{13} interferes with the pinning by the step more severely than the vertical interaction H. This finding can be explained by the fact that at the step J_{12} and J_{13} act between sites with different vertical interactions $H \pm H_s$, thus the influence of the step is spread also to the neighbouring sites of the step sites. On the other hand, H is modified only at the step sites, thus the step influence is smaller. In both cases, T_c does not differ from the respective value of the planar system.

The introduction of both J_{13} and H to the stepped system increases the different ideal possibilities for cluster formation. Thus, only one very broad peak is obtained in the cluster size distribution which covers the region $56\% < A < 96\%$ with a maximum at $A = 80\%$ and a large width of approximately $w = 16\%$. Thus, the surface step can be regarded as a locally strongly ordering element, which may be employed for the assembly of molecules, but the assembly conditions are determined by the relative values of J_{13} and H.

5. Conclusions

The present investigation demonstrates a scale-hopping approach in the simulation of ordered O-FET arrays, where the single functional element consists of an electric-field sensitive, polarisable organic molecule, which is adsorbed on a ferroic oxide, that exhibits a switchable spontaneous polarisation on the surface.

Density-functional investigations (DFT) on titanate ceramics confirm that the rich defect chemistry of these materials strongly influences the structural, electronic, and elastic properties at and near surfaces. The study focusses on the influence of structural defects, which are always present even on nominally flat, clean, and stoichiometric surfaces of $BaTiO_3$. Strong structural relaxations were obtained, which can compete with the ferroelectric distortion. Thus the direction of the electric field above a defective surface differs from the one above a planar surface at distances, which are typical in adsorbate-substrate systems, and reaches unscreened field strengths of up to 10^9 V/m.

This field shall be employed to switch the electronic properties of a polarisable organic molecule, in the present case of oligothiophenes. Density-functional-based tight-binding calculations (DF-TB) provide access to the geometric and electronic properties of larger model systems within a quantum-mechanical framework, hence they were employed to assess the members of the oligothiophene series for the potential as switchable gate element of the O-FET. By calculating the response of the electron energy levels to an external electric field, a strong field-induced change of the optical properties is obtained for the longer members of the series. Thus, possible candidates as functional adsorbates at the expected field above the $BaTiO_3$ steps have been suggested on the basis of the DF-TB modelling.

Finally, the prerequisites for self-organisation of such planar functional units on-top of a vicinal bAtIo$_3$ surface have been evaluated with the help of an extended Monte-Carlo-Ising model (MCI). Large, well-ordered adsorbate clusters are formed even at elevated temperature, if the lateral interactions dominate over the vertical adsorbate-substrate attraction and/or if extended anchor sites such as steps exist on the surface. Competing vertical and lateral interactions lead to the pinning of smaller cluster seeds, whereas larger, but more irregular clusters are formed if the vertical interaction dominates.

Acknowledgments

The authors acknowledge support from the Deutsche Forschungsgemeinschaft via the Schwerpunktprogramm 1157 and from the German-Israel-Foundation.

References

[1] (a) L. M. Eng, F. Schlaphof, S. Trogisch, A. Roelofs, R. Waser, “Status and future aspects in nanoscale surface inspection of ferroics by scanning probe microscopy”, Ferroelectrics **251**, 11 (2001); (b) W. C. Yang, B. J. Rodriguez, A. Gruverman, R. J. Nemanrich, “ Polarization-dependent electron affinity of LiNbO$_3$ surfaces” Appl. Phys. Lett. **85**, 2316 (2004); (c) H. Kessler, H. Balke, “A continuum analysis of charge induced ferroelectric domain wall motions”, J. Mech. Phys. Sol. **54**, 86 (2006); (d) H. Zhang, Z. Yin, M. S. Zhang, “Phase structures and stability in barium titanate ferroelectric ultrathin films”, Phys. Lett. A **310**, 479 (2003); (e) S. Dorfman, D. Fuks, E. Kotomin, “Comparative study of [001] surface relaxations of perovskite titanates”, Thin Sol. Films **318**, 65 (1998).

[2] P. Hohenberg, W. Kohn, “Inhomogeneous Electron Gas”, Phys. Rev. **B136**, 864 (1964); W. Kohn, L. J. Sham, “Self-consistent equations including exchange and correlation effects”, Phys. Rev. bf A140, 1133 (1965).

[3] (a) www.abinit.org; the ABINIT code is a common project of the Universite Catholique de Louvain, Corning Inc., and other contributors; (b) M. Elstner, D. Porezag, G. Jungnickel, J. Elsner, M. Haugk Th. Faruenheim, S. Suhai, G. Seifert “Selfconsistent-charge density-functional tight-binding Method for Simulations of Complex Materials Properties” Phys. Rev. B **58**, 7260 (1998); (c) A. di Carlo, m. Gheorghe, P. Lugli, M. Sternberg, G. Seifert, Th. Frauenheim, “Theoretical tools for transport in molecular nanostructures”, Physica B bf 314, 86 (2002); (d) Gaussian; Gaussian 03, Revision C.02, M. J. Frisch, G. W. Trucks, H. B. Schlegel, G. E. Scuseria, M. A. Robb, J. R. Cheeseman, J. A. Montgomery, Jr., T. Vreven, K. N. Kudin, J. C. Burant, J. M. Millam, S. S. Iyengar, J. Tomasi, V. Barone, B. Mennucci, M. Cossi, G. Scalmani, N. Rega, G. A. Petersson, H. Nakatsuji , M. Hada, M. Ehara, K. Toyota, R. Fukuda, J. Hasegawa, M. Ishida, T. Nakajima, Y. Honda, O. Kitao, H. Nakai, M. Klene, X. Li, J. E. Knox, H. P. Hratchian, J. B. Cross, V. Bakken, C. Adamo, J. Jaramillo, R. Gomperts, R. E. Stratmann, O. Yazyev, A. J. Austin, R. Cammi, C. Pomelli, J. W. Ochterski, P. Y. Ayala, K. Morokuma, G. A. Voth, P. Salvador, J. J. Dannenberg, V. G. Zakrzewski, S. Dapprich, A. D. Daniels, M. C. Strain, O. Farkas, D. K. Malick, A. D. Rabuck, K. Raghavachari, J. B. Foresman, J. V. Ortiz, Q. Cui, A. G. Baboul, S. Clifford, J. Cioslowski, B. B. Stefanov, G. Liu, A. Liashenko, P. Piskorz, I. Komaromi, R. L. Martin, D. J. Fox, T. Keith, M. A. Al-Laham, C. Y. Peng, A. Nanayakkara, M.

Challacombe, P. M. W. Gill, B. Johnson, W. Chen, M. W. Wong, C. Gonzalez, and J. A. Pople, Gaussian, Inc., Wallingford CT, 2004.

[4] N. Metropolis, S. Ulam, "The Monte-Carlo Method", J. Am. Stat. Assoc. **44**, 335 (1949).

[5] J. Hoshen, R. Kopelman, "Percolation and cluster distribution. 1. Cluster multiple labelin technique and critical concentration algorithm", Phys. Rev. B **14**, 3438 (1976).

[6] (a) L. Onsager, Phys. Rev. 65 (1944) 117; (b) C. N. Yang, Phys. Rev. 85 (1952) 808; (c) C. Domb, P. Sykes, Proc. R. Soc. Lond. A 240 (1957) 214.

[7] C. Olbrich, Bachelor thesis, Technische Universitt Chemnitz, 2004.

[8] C. Loppacher, U. Zerweck, L. M. Eng, S. Gemming, G. Seifert, C. Olbrich, K. Morawetz, M. Schreiber, "Adsorption of PTCDA on a partially KBr covered Ag(111) substrate", Nanotechnology **17**, 1568 (2006).

Advancing Multiscale Materials Modeling In The Nanotechnology Consortium

Gerhard Goldbeck-Wood

Accelrys Ltd, 334 Cambridge Science Park, Cambridge, CB4 0WN, UK,
gerhard@accelrys.com .

ABSTRACT

The Accelrys Nanotechnology Consortium is a global collaborative initiative aimed at advancing modeling and simulation tools for the development of advanced materials and devices. This initiative was started by Accelrys in July 2004, and is funded entirely by Accelrys and Consortium members. Membership currently stands at 21 organisations, a mixture of large corporations, small enterprises, government labs and universities from the US, Europe, South Africa, and Japan. In addition, advisors and collaborators provide input and new code developments which are further enhanced at Accelrys and delivered to Members in an integrated fashion. Software delivered to the Members so far within Materials Studio ® [1] includes new nanostructure builder tools for nanotubes and clusters, the linear scaling ONETEP method [2], and the new GULP 3.0 classical code [3], which includes a wide range of forcefield technology. Current developments include a forcefield fitting interface for GULP, a new adsorption tool, and the development of a hybrid simulations environment for QM/MM simulations.

1. Background and aims

Numerous reports have highlighted that ‘fundamental understanding’ and multiscale modeling and simulation are crucial for the advancement of nanotechnology, and for achieving a more rational approach to the development of nanomaterials and devices [4]. Roadmaps call for a development of modeling tools to meet those challenges, but the question remains as to what concrete steps can be taken to actually develop useful new technology and deliver new tools to a wider audience of users.

In order to address these needs on a truly international basis, the Nanotechnology Consortium was started on 1 July 2004 as an initiative led by Accelrys. The aim of the Consortium is to ensure that Members can access leading-edge modeling and simulation software technology and steer the development of the technology to meet their R&D needs.

Setting up the Consortium, Accelrys, academic advisors, and customers recognize that today’s advanced materials and nanotechnology research poses new challenges at the atomistic and molecular scale, but that at the same time there are developments of software technology which can be brought to bear strongly on these challenges. The Consortium was set up to meet the challenges and realize the opportunities in software technology to impact on Members’ research success.

The objectives of the Consortium stated translate in concrete terms in:

- Enabling the investigation of systems of a scale and complexity which has so far been out of reach.
- Making it easier and more time-efficient to set up calculations for such systems.

- Enabling generally complex tasks to be bundled into a streamlined workflow which can be automated.

2. Progress to date

In relation to the above goals, the Consortium has made rapid progress, concentrating first of all on three major development areas, namely:

- Ease of constructing complex nanostructures. This development resulted in the release of new Nanotube and Nanocluster Builders.
- Accessing much larger systems, of O(1000) atoms, with quantum accuracy. The new ONETEP [2] linear scaling DFT method has been implemented.
- Accessing a wider range of materials and properties, as well as the ability for very large systems, of O(100,000) atoms, in classical simulations. A new version of the GULP [3] code has been implemented to address this area.

Further progress is underway to address member requirements for hybrid simulations and for studying adsorption. In addition, there are ongoing enhancements to the functionality in the modules delivered already, in particular ONETEP and GULP.

3. Nanostructure Builders

One of the initial developments of the Consortium were new Builders for Nanotubes and Clusters. The Nanotube Builders support the building of single-wall nanotubes (SWNT), multi-wall nanotubes (MWNT) and nanoropes (bunches of nanotubes).
The Nanocluster Builder supports the construction of clusters of specified shapes. Starting from a 3d-periodic model, the user chooses one of these shapes, the relevant size parameter values, and the base plane used for cutting. There are options for capping broken bonds, and for cutting either by clipping atoms or molecules. Also supported are vacancy concentrations in the cluster, and substitution of each of the atomic species by a different element. Substitution gradients along certain symmetry directions of the shape are defined, with linear, quadratic and exponential functional forms supported.

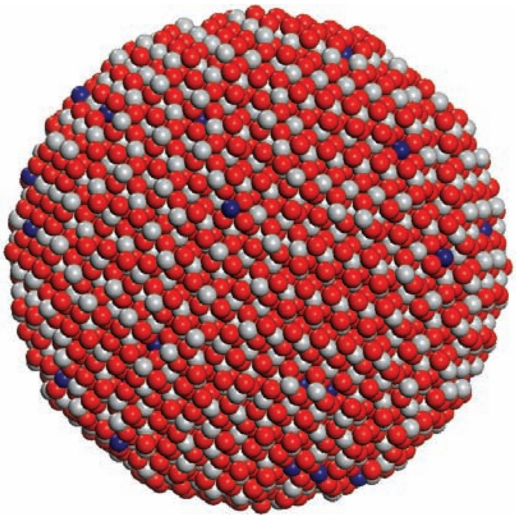

Figure 1: TiO_2 nanoparticle, with Vanadium substitutions

4. ONETEP

ONETEP [2] is a completely new, breakthrough technology based on density functional theory. ONETEP stands for Order N Electronic Total Energy Package, and due to its linear scaling capability allows high accuracy studies of systems much larger than has been possible with existing codes, but at the same time is a very robust technology well suited to industrial applications.

ONETEP has already been validated for a wide range of systems and applications, including basic validation for example on the precision on hydrogen-bond interactions, elastic constants calculation, density of states in insulating and conducting nanotubes etc, as well as applications on systems for which DFT calculations have been pretty much out of reach up to now, such as large nanotube, proteins, DNA, and zeolite systems.

Currently ONETEP in Materials Studio enables total energy and geometry optimization calculations, and electronic density as well as potential analysis. Development of further functionality is progressing rapidly, with transition state searching, spin polarization, charge calculations, orbital displays about to become available, followed by further property analysis. Further information on ONETEP, theory, implementation and applications is available in a number of publications, including an article in the recent psi-k newsletter [5].

4. GULP

The GULP [3] code has been implemented in Materials Studio for the Consortium as a leading-edge classical tool to complement the DFT methods. GULP provides important forcefield libraries and potentials for nanomaterials research, including shell model forcefields for oxides and other polarisable systems, embedded atom method forcefields for metals, the Tersoff bond order potentials for semiconductor systems, and the Brenner REBO potential for reactive systems. GULP provides access to a very wide range of properties, including elastic constants, bulk, shear, Young’s moduli, piezoelectric constants, dielectric constants and refractive indices with frequency dependence, phonon frequencies and density of states, Born effective charges, surface and attachment energies.

Amongst the capabilities of GULP that are being integrated into Materials Studio are interfaces to frequency dependent optical properties and to the powerful GULP forcefield fitting engine.

5. Adsorption Protocol

A key development direction of the Consortium is to enable a more flexible, task driven approach to simulations. The aim is to support workflows geared at the calculation of certain properties, or finding structures with certain property profiles. Typically such workflows involve a number of calculation and filtering tasks, using a variety of existing servers. In many cases there may also be additional algorithms required to complete the workflow.

As a first example, the Consortium is pursuing the development of an Adsorption protocol. Typical stages of such a protocol will be (a) the selection of a substrate and adsorbate structure, (b) the generation of adsorbate molecule conformers, (c) a tool which generates possible adsorbed configurations, (d) fast energy and geometry optimization calculations to serve as an initial filter, (e) further higher level energy and geometry optimization calculations to determine structures and adsorption energies. The final ‘product’ would be a customizable protocol including a range of different server codes.

6. Hybrid Simulations

Hybrid Simulations incorporate two levels of scale in an integrated fashion. Consortium Members have voted to pursue such methods as a matter of priority, as they are able to address the many examples found in advanced materials development where electronic level events and phenomena need to be described at a high level of theory, while it is still important to include the long range effect of a larger amount of surrounding material. The Consortium is involved in two methods, ‘traditional’ QM/MM and the novel LOTF (Learn-on-the-fly) [6] method, the former focusing on bridging length scales, the latter a novel method which addresses the time scale issue as well.

7. Summary and Outlook

The Nanotechnology Consortium has taken some major steps in actually delivering on new modeling tools called for in a number of roadmaps on nanotechnology. The current Phase 1 of the Consortium, which runs until 31 August 2007, will continue to deliver and enhance software such as ONETEP, GULP and QM/MM, but also start developing workflows aimed at complex property determinations.

Despite the advances of linear scaling and multiscale approaches, a major gap between a bottom-up approach fundamentally based on atoms and molecules, and a top-down, engineering modeling approach based on continuous units of matter remains. In complex systems as we encounter in nanotechnology, the solution may require a more flexible system modeling approach. A workflow of processes, linking modeling components through networks of data-pipelines in more flexible ways is now possible using software such as Pipeline Pilot™ [7], which enables the protocols incorporating a wide range of calculation and simulations components as well as data sources. The Consortium will be pursuing implementations and utilization of this type of technology. In particular, plans for a Phase 2, running to 2010, are starting to emerge with a strong emphasis on building workflow protocols to enable Computer Aided Nanodesign (CAN)™ of materials and devices.

References

[1] Materials Studio ® by Accelrys Software Inc, San Diego, CA. See http://www.accelrys.com/products/mstudio/ .

[2] C-K. Skylaris, P.D. Haynes, A.A. Mostofi, M.C. Payne, J. Phys.: Condens. Matter **17**, 5757 (2005).

[3] J.D. Gale and A.L. Rohl, Molecular Simulation, **29**, 291 (2003).

[4] Chemical Industry Vision2020 Technology Partnership Chemical Industry R&D Roadmap for Nanomaterials By Design: From Fundamentals to Function (2003).

[5] P.D. Haynes, C-K. Skylaris, A.A. Mostofi, M.C. Payne, Psi-k Newsletter, http://psi-k.dl.ac.uk, **72**, 78 (2005).

[6] G. Csányi, T. Albaret, G. Moras, M.C. Payne and A. De Vita, J. Phys.: Condens. Matter, **17**, R691 (2005).

[7] Pipeline Pilot ™ by SciTegic: http://www.scitegic.com/products/overview/index.html

Measurement and Rationalisation of Domain Periodicities in Nanoscale Ferroics and Multiferroics

J.M. Gregg

Queen's University, University Road, BT7 1NN, Belfast, United Kingdom

Rationalisation of the formation of domain structures, in ferroics of limited dimensions, has been a topic of interest since the 1940's [1], with early work, specifically in ferroelectrics, in the 1950's [2]. Experimental studies at that time primarily involved domain investigations using optical microscopy, on samples down to the order of hundreds of microns. More modern studies, extending domain research into the thin and ultrathin film regime [3], suggest that our understanding of certain aspects of domain behaviour remain relatively unchanged, despite the intervening decades. This might imply that reduction of scales into the nanometre range will not reveal anything new or interesting in ferroic domain research. In this talk, we hope to illustrate that this is not the case. We describe results from a recent research programme on the characterisation of ferroelectric domain structures in single crystal $BaTiO_3$ (BTO), and ferroelectric and ferromagnetic domain structures in single crystals of the multiferroic $YMnO_3$ using Scanning Transmission Electron Microscopy (STEM). Sample preparation was performed using a Focused Ion Beam Microscope (FIB) which allowed for careful control of the thickness of the specimen to be examined under STEM, and even allowed for an investigation of the accommodation mechanisms by which domain periodicity can adapt to changing specimen thicknesses. In BTO, the domain periodicity has been measured as a function of thickness of parallel-walled slabs from several hundred nanometres down to ~50nm. Early work [2] suggested that the domain width should vary as the square root of slab thickness, and this is consistent with our data. However, we find, in plotting data from several works on different ferroelectric materials, with differing surface boundary conditions, across six decades in thickness, that all data lie on the same parent function, with the same constants of proportionality. This is totally unexpected, as the proportionality constants should be material and surface boundary state dependent. In addition literature analysis of ferromagnets also shows broad adherence to a Kittel relation but that there is clearly a different coefficient of proportionality in the Kittel relation for ferromagnets than for ferroelectrics. Thus by inspection of literature data alone, it would appear that ferroelectrics adhere to one universal Kittel relation, and ferromagnets to another. This raises the interesting question of what governs domain periodicity in multiferroic materials, and this will be discussed with specific reference to the $YMnO_3$ system.

[1] C. Kittel, Physical Review, 70, 965 (1946)

[2] T. Mitsui and J. Furuichi, Physical Review, 90, 193 (1953)

[3] S. K. Streiffer et al. Phys. Rev Lett. 89, 067601 (2002)

Ab initio studies on the magnetic phase stability of iron

R. Iglesias[1] **and S. L. Palacios**[2]

[1]Nuclear Energy and Safety Research Department, Paul Scherrer Institut, CH-5232 VilligenPSI, Switzerland, e-mail: roberto.iglesias@psi.ch; [2]Departamento de Física, Universidad de Oviedo, E-33007 Oviedo, Spain.

ABSTRACT

The possible collinear magnetic configurations of the α– and γ–Fe phases have been analyzed using the full-potential linearized augmented plane wave (FLAPW) method and the fixed spin moment (FSM) procedure. From our calculations, the so-called AF-II antiferromagnetic phase is the collinear ground state of γ-Fe, while for α-Fe the well-known ferromagnetic ground state is found. At some volumes, a crossing or degeneration of two or more magnetic phases appears. This may be regarded as an indication of a true noncollinear magnetic ground state of the system that remains to be studied.

1. Introduction and background

The magnetism of iron and its alloys has been the subject of a continuing research effort in the field of Materials Science since its beginnings. Their functionality and technological relevance reflects in the fact that these alloys are prime candidate structural materials designed for use in extreme conditions for advanced nuclear applications. On the other hand, the rich diversity of phenomena showed by these materials makes them excellent test systems in which to analyze the coexistence of several magnetic phases. The aim of this work is to study the relative stability of the collinear magnetic equilibrium configurations of the bcc α and fcc γ phases of pure Fe. In recent years, this has been the subject of numerous studies, which have even raised a certain controversy. Band structure theoretical calculations have evidenced that the α–Fe ground state is undoubtedly ferromagnetic (FM). The situation for γ–Fe is rather complex, showing a competition in terms of energy among several spin configurations that may be excited as temperature rises. Using the FLAPW method within the generalized gradient approximation (GGA), Herper *et al.* [1] found an antiferromagnetic (AF) ground state for γ–Fe. However, they were unable to distinguish which of the two possible AF orderings described was the ground state. In agreement with experiments, γ–Fe was predicted by Knöpfle *et al.* [2] to have a high spin (HS) FM state and a low spin (LS) FM state at large and small volumes, respectively, by means of a modified augmented spherical wave (ASW) method. The AF state lies below the LS state and a lower energy spin spiral (SS) state was also found. The HS to LS transition takes place through successive noncollinear magnetic states [2, 3]. On the contrary, Kong and Liu [4] predicted very recently a LS FM γ–Fe ground state using the projector augmented wave (PAW) pseudopotential method, within the GGA. They also found an additional very low spin (VLS) phase that had been pointed out before by Marcus *et al.* [5], who described a non-magnetic (NM), two AF, a HS FM, a LS FM, a SS and even a ferrimagnetic (FIM) phase. They used the ASW method and the FSM procedure to find that the AF-II phase, considered below, was the ground state of γ–Fe.

2. Results and discussion

This work is devoted to carefully check the relative stability of the collinear magnetic configurations present in the α– and γ–Fe phases. The FLAPW method and the FSM procedure [6] implemented in the WIEN2k code [7] have been used. The minima of the energy vs. moment curves for a given volume found with the FSM procedure represent the true magnetic phases of the system. In addition to the common NM and FM states, we have performed calculations for two AF structures: the usual AF-I with alternating layers of up and down spins and the so-called AF-II phase made up of double layers that possess FM intralayer coupling, which can only exist in a four-atom unit cell (or larger). For α–Fe only the AF-I structure was used and using the FSM procedure the AF-I and FM solutions coincide.

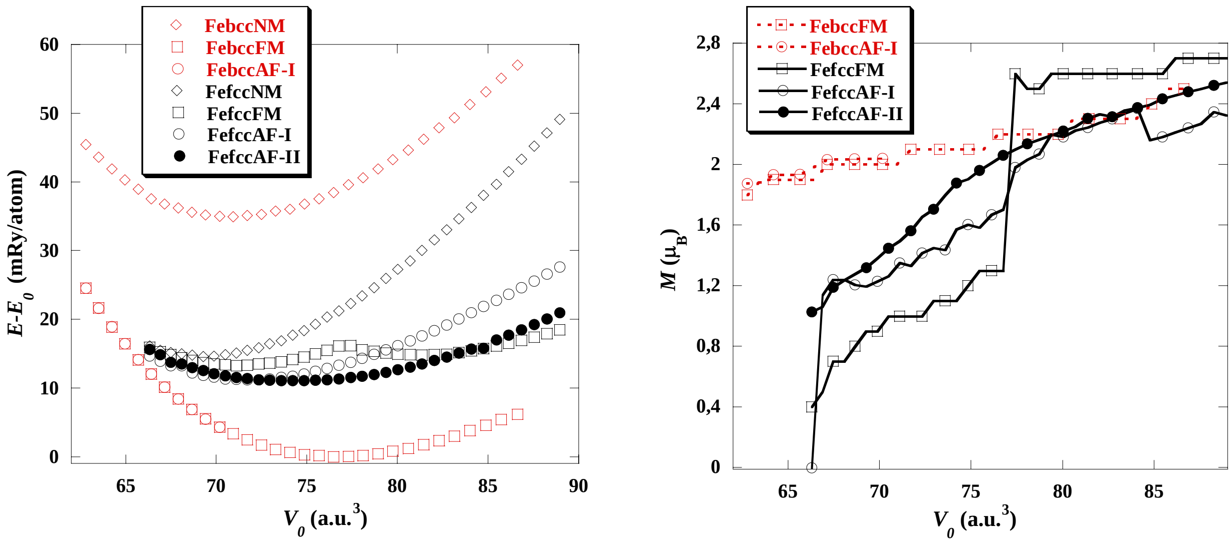

Figure 1. Total energies relative to the bcc minimum energy (E-E_0), left, and magnetic moments M, right, of α- and γ-Fe calculated with FLAPW-GGA.

The results of our calculations for cubic Fe appear in Fig. 1. In agreement with experiment we find a FM α phase ground state, characterized by a lattice constant a=2.83 Å and an atomic magnetic moment M=2.2 μ_B. The $E(M)$ curves calculated at fixed lattice constants have all only one FM minimum at a finite M throughout the whole range of lattice parameters studied. The NM solution is energetically unfavorable, about 35 mRy higher in energy than the FM phase. The α–Fe FSM AF-I solution is unstable and indistinguishable from the FM ground state (Fig. 1). For the sake of comparison, a set of non-FSM AF-I calculations has been performed. The AF-I solution is 32.3 mRy higher in energy than the FM state. Both these energy values for the NM and AF-I spin configurations compare favorably to the ones in Ref. 1, namely, 33.9 and 32.0 mRy, respectively. We turn now our attention to the magnetic configurations of γ–Fe. The AF-II ordering is the ground state, with M=1.90 μ_B. This is in agreement with the FSM results of Ref. 5 and also with the findings in Ref. 1. In contrast to these authors, we are able to discriminate in energy between the two AF states, though the difference is very low (0.1 mRy/at). It may well be that both states would converge in energy if the number of antiferromagnetic layers is increased, as they suggest. In any case, our results strongly disagree in this respect with the work by Kong and Liu [4], who predicted a LS FM ground state. They also found two distinct AF states, but both correspond to our AF-I. This is definitely not our case: we get only one minimum for the AF-I structure. For volumes below about V=66 a. u.^{3} all four magnetic states for γ–Fe tend to converge. This is already far from the energy minimum, in contrast to the PAW results [4] and early FSM calculations [5]. The first state to branch away from the coexistence region is the NM, which therefore would only be the most stable phase in a volume range below that shown in Fig. 1. The FM phase presents two distinct and separate minima, being the low-volume LS minimum flatter, while the high-volume HS minimum is sharply defined. The total energy minimum is 1.5 mRy/at lower for the LS state, in agreement with Refs. 1 and 4, but in contrast to Ref. 2. Our calculations reveal no VLS phase as in Refs. 4 and 5. The transition between the two FM states takes place at *a*~3.57 Å, in agreement with the literature [1, 4, 8], through a series of AF states [3]. At large volumes, first the AF-I and later the AF-II configurations become higher in energy than the HS FM state, which is found to be the γ–Fe ground state above *a*=3.68 Å, in accordance to Ref. 5. The coexistence of two or more magnetic phases in extended sections of the γ–Fe *E(V)* curves is regarded as an indication of a true noncollinear magnetic ground state of the system [2]. Nevertheless, the analysis of the collinear magnetic configurations of γ–Fe is in itself attractive. For instance, the γ–Fe precipitates present in ferromagnetic Fe_xCu_{100-x} mechanically alloyed solid solutions seem to have an HS FM ground state [8], with a magnetic moment close to our theoretical value of 2.6 μ_B. We find a good agreement between our results and other FLAPW-GGA calculations [1], except for a slight overestimation (~3.5 mRy/at) of the γ-Fe energies. On the other hand, the use of non-full potential methods leads to a HS FM ground state for the γ-Fe system [4 and references therein], and is for sure the reason for the lower magnetic moments in the AF-I (0.72 μ_B) and LS FM (0.62 μ_B) spin configurations as compared to full potential calculations (1.33 μ_B and 1.0 μ_B, respectively).

3. Conclusion

Ab initio FLAPW-GGA calculations in the frame of the FSM procedure represent an adequate approach to examine the possible collinear magnetic configurations of α– and γ–Fe. The experimental FM ground state of α–Fe has been obtained and both the NM and AF solutions lay at much higher energies. Using a four-atom unit cell, the collinear ground state of γ–Fe is found to be a double-layered AF configuration. Up to five different spin orderings have been described and seen to coexist at certain volumes. These competing magnetic states point to the existence of a noncollinear magnetic ground state for γ–Fe, which could possibly account for the transitions between stable collinear configurations. Our predictions imply that, in agreement with previous work, γ–Fe is expected to behave anomalously as temperature increases due to the many spin configurations that may become excited.

References

[1] H. C. Herper, E. Hoffmann, and P. Entel, *Ab initio full-potential study of the structural and magnetic phase stability of iron*, Phys. Rev. B **60**, 3839 (1999).

[2] K. Knöpfle, L. M. Sandratskii, and J Kübler, *Spin spiral ground state of γ–iron*, Phys. Rev. B **62**, 5564 (2000).

[3] P. James, O. Eriksson, B. Johansson, and I. A. Abrikosov, *Calculated magnetic properties of binary alloys between Fe, Co, Ni, and Cu*, Phys. Rev. B **59**, 419 (1999).

[4] L. T. Kong and B. X. Liu, *Correlation of magnetic moment versus spacing distance of metastable fcc structured iron*, Appl. Phys. Lett. **84**, 3627 (2004); L. T. Kong and B. X. Liu, *Distinct magnetic states of metastable fcc structured Fe and Fe-Cu alloys studied by ab initio calculations*, J. Alloys Comp. **414**, 36 (2006).

[5] P. M. Marcus, S. L. Qiu, and V. L. Moruzzi, *The magnetic phases of face-centred-cubic iron*, J. Phys.: Condens. Matter 1**1**, 5709 (1999).

[6] K. Schwartz and P. Mohn, *Itinerant metamagnetism in* YCo_5, J. Phys. F: Met. Phys. **14**, L129 (1984).

[7] P. Blaha, K. Schwartz, G. K. H. Madsen, D. Kvasnicka, and J. Luitz, *WIEN2k An augmented plane wave+local orbitals program for calculating crystal properties* (Technische Universität Wien, Austria, 2001).

[8] S. L. Palacios, R. Iglesias, D. Martínez-Blanco, P. Gorria, M. J. Pérez, J. A. Blanco, A. Hernando, and K. Schwarz, *High-temperature anti-Invar behavior of γ–Fe precipitates in* Fe_xCu_{100-x} *solid solutions: Ferromagnetic phases*, Phys. Rev. B **72**, 172401 (2005).

Ferroelectrics: Experiments, Micromechanics, and Constitutive Modeling

Marc Kamlah, Dayu Zhou, Bernd Laskewitz

Forschungszentrum Karlsruhe Institut für Materialforschung II, Postfach 3640, D-76021 Karlsruhe, Germany, kamlah@imf.fzk.de

ABSTRACT

In this paper, we will first discuss the typical hysteresis properties observed with ferroelectric materials in relation to the underlying domain switching processes. Then, we will present an experimental investigation determining the critical states of combined coaxial electrical and mechanical loading needed to initiate domain switching processes (switching criterion). Next, we will present a micromechanical finite element simulation of a ferroelectric volume element, where each grain exhibits single crystal behavior for the switching of its domains. Finally, we will introduce a micromechanically based constitutive model, which relies on internal variables representing an approximate distribution orientation function of the micro-dipoles. This constitutive model allows for the finite element analysis of the poling process of piezoceramic devices.

1. Introduction

Piezoelectricty is a phenomenon related to a distinct anisotropy of the microstructure, the *polar symmetry*, and, additionally, to a high degree of *order* of this anisotropy in the sample under consideration. Despite of the random orientation of their lattice axes, certain polycrystals possessing the so-called *perovskite structure* may exhibit piezoelectric coupling below the Curie temperature. Inside each grain of such a material, there are *domains* with different orientation of the polar symmetry and the capability for piezoelectricity is caused by *ferroelectricity.* This means that the orientations of these domains may be *switched* by electric or mechanical loads of sufficient magnitude. By the *poling process*, the orientation of domains is ordered in the direction of a strong electric field leading to a net *remanent* polarization and piezoelectric properties on the level of the polycrystal, see Fig. 1. For a detailed discussion see [1].

2. Experimental Findings

An important issue is the identification of critical electro-mechanical loading states for the onset of microscopic switching processes. For this purpose a coaxial electric field and a compressive mechanical stress have been applied as proportional loading histories, see the left panel of Fig. 2. Using an offset method, the onset of switching could be identified in the measured strains giving the bold dots at the right panel of Fig. 2. In view of these results, it turns out that an electro-mechanically extended Tresca or Drucker-Prager criterion, which are equivalent for this special loading history, appear to be closer to the experiments than an electromechanical von Mises criterion. For further details on this investigation see [2].

3. Micromechanical Volume Element

As shown in the previous section, there is a clear understanding of the microscopic domain switching processes underlying the macroscopic behaviour of ferroelectric materials. Microme-

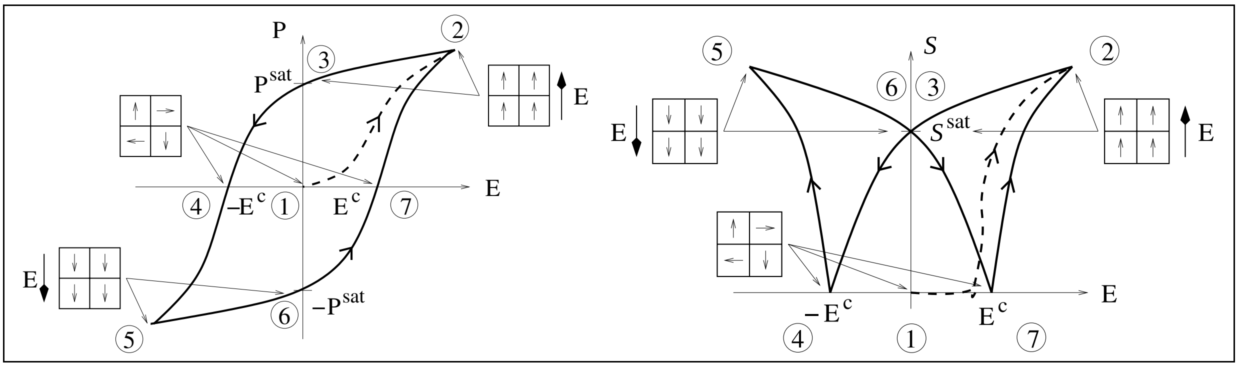

Figure 1: Schematic sketch with idealized domain states indicating the microscopic origin of the macroscopic dielectric and butterfly hystereses as the materials response to a cycling electric field with amplitudes of approximately twice the coerive field strength E^c. The ferroelectric material exhibits macroscopic piezoelectric properties in the poled states 2-3 and 5-6.

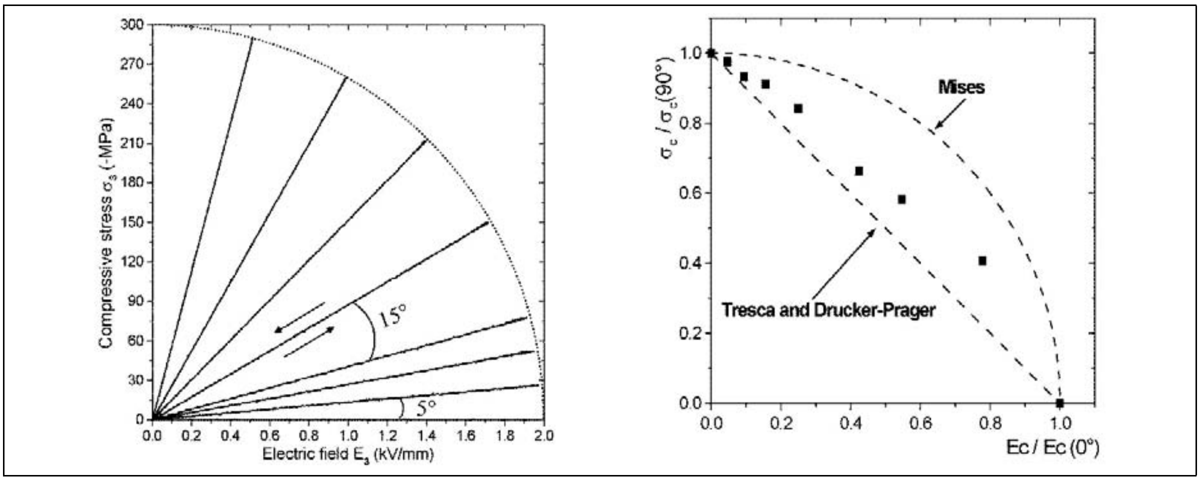

Figure 2: Left: Proportional loading paths of coaxial electric field and compressive mechanical stress. Right: Bold dots represent the onset of switching identified by an offset method.

chanical concepts allow for the physical modeling of processes on the grain level and their impact on the properties of the polycrystalline aggregate. In this sense, a two-dimensional volume element under plane strain conditions has been considered, see the left panel of Fig. 3. Grain to grain interaction and electromechanical field coupling are taken into account by the finite element method. Each finite element is identfied with a ferroelectric grain possessing single crystal properties for the switching of its domains according to the model by Huber *et al.* [3]. By means of this model, the influence of grain to grain interaction and of the orientation distribution of the lattice axes of the grains can be discussed, see [4]. As a example, the right panel of Fig. 3 shows the strain repsonse of the polycrystalline aggregate to the poling process.

4. Micromechanically Motivated Constitutive Model

In the literature, a general structure for macroscopic constitutive models based on the additive decomposition of polarization and strain into reversible (piezoelectric) and irreversible (remanent) parts has been established, see [1]. In an intermediate approach between pure phenomenological and micromechanical modeling, a step function approximation for the orientation distribution of the domains is introduced, where the parameters of this function serve as internal variables (left panel of Fig. 4). Exploiting the Clausius-Duhem inequality, thermodynamically conjugated driving forces for the internal variables are obtained. The normality rule is applied to a convex switching function to obtain the evolution equations for the internal variables in terms of ordinary differential equations. The right panel of Fig. 4 shows the butterfly hysteresis as it is simulated by this model. For a detailed description see [5]. Implementation of this model in a finite element code allows for the analysis of poling processes in piezoceramic tubes. It can be shown that, depending on the ratio of inner to outer radius, due to a ferroelectric Bauschinger effect, complete radial poling of tubes may be impossible, leading to inhomogeneous electromechanical fields in the tube wall.

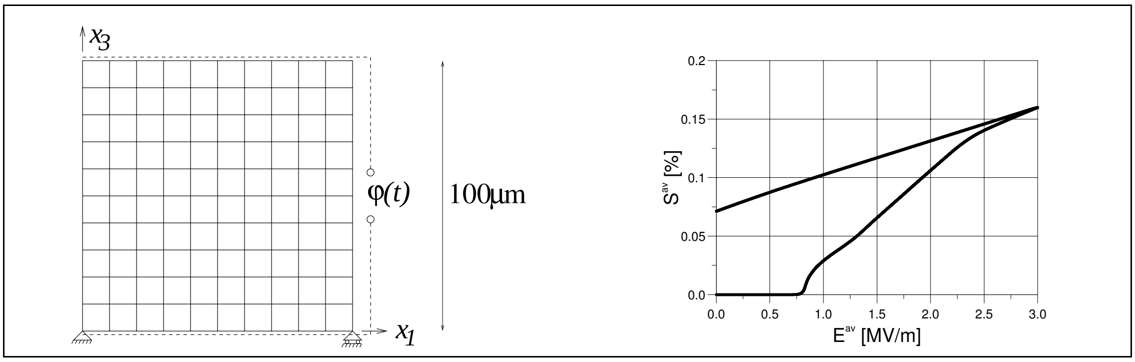

Figure 3: Left: polycrystalline volume element consiting of 10x10 ferroelectric grains. Right: Strain response to electric loading (poling).

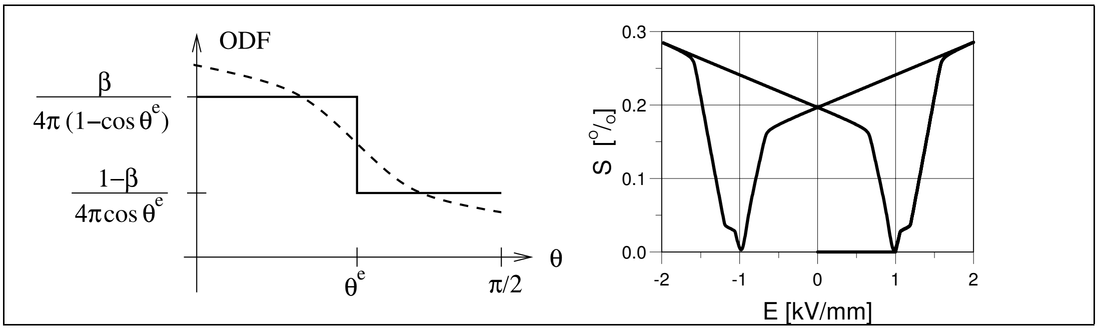

Figure 4: Left: Approximate orientation distribution function. Right: Butterfly hysteresis according to micromechanically motivated constitutive model.

Acknowledgement

Financial support by the Deutsche Forschungsgemeinschaft is gratefully acknowledged.

References

1. Kamlah, M., “Ferroelectric and Ferroelastic Piezoceramics – Modeling of Electromechanical Hysteresis Phenomena. Review Article,” Continuum Mech. Thermodyn. **13**(2001), 219 - 268

2. Zhou, D., Wang, Z., Kamlah, M., “Experimental investigation of domain switching criterion for soft lead zirconate titanate piezoceramics under coaxial proportional electromechanical loading,” J. Appl. Phys. **97**(2005), Art. No. 084105

3. Huber, J.E., Fleck, N.A., Landis, C.M., McMeeking, R.M., “A Constitutive Model of Ferroelectrics,” J. Mech. Phys. Solids **47**(1999), 1663 - 1697

4. Kamlah, M., Liskowsky, A. C., McMeeking, R. M., Balke, H., “Finite Element Simulation of Polycrystalline Piezoceramic Behavior on the Basis of a Multidomain Singe Crystal Switching Model,” Int. J. Solids Structures **42**(2005), 2949 - 2964

5. Kamlah, M., Wang, Z., “A Thermodynamically and Microscopically Motivated Constitutive Model for Piezoceramics under Uniaxial Loading,” In: Lagoudas, D. C. (ed.): Active Materials: Behavior and Mechanics. SPIE Vol. 5387, Bellingham 2004, 390 - 401.

Triple defect and constitutional vacancies in B2 binaries. Direct Bragg - Williams thermodynamics.

Andrzej Biborski, Rafał Kozubski

Interdisciplinary Centre for Materials Modelling, M. Smoluchowski Institute of Physics,
Jagellonian University, Reymonta 4, 30-059 Krakow, Poland,
e-mails: biborski@wp.pl, rafal.kozubski@uj.edu.pl

ABSTRACT

Thermal vacancy formation correlated with atomic ordering was modelled in B2-ordering A-B binary intermetallics. Bragg-Williams Hamiltonian was implemented with specific thermodynamic formalism for thermal vacancy formation. It has been demonstrated that for particular pair-interaction energetics assumed, equilibrium concentrations of vacancies and of A-antisites result mutually proportional in well defined temperature ranges. The effect observed both in stoichiometric and non-stoichiometric A-rich binaries is accompanied by a marked vacancy site occupation preference on A-sublattice and thus is interpreted as a tendency for triple defect formation. Correspondingly, in B-rich non-stoichiometric binaries vacancy concentration does not extrapolate to zero at $T \rightarrow 0$ K, which indicates the formation of constitutional vacancies. Energetic conditions for the occurrence of the effects are analysed in detail. The novelty of the calculation consists of direct minimisation of the thermodynamic potential without using any a priori assumptions for small vacancy concentration etc., as is usually done in literature.

1. Introduction

Recent experimental study revealed surprisingly slow B2-long-range-ordering (LRO) kinetics in stoichiometric NiAl [1]. In view of a very high vacancy concentration in NiAl [2], the proposed explanation of the result has been based on the triple-defect formation/elimination as a mechanism of the process. It is now intended to verify this hypothesis by means of Monte Carlo simulation, which, however, in contrary to the previous studies [3], must involve thermal vacancy formation. The present study of vacancy thermodynamics in B2-ordered binaries opens the project.

In most of the works devoted to modelling of vacancy and triple defect thermodynamics in B2 systems very strong a priori assumptions have been made: these are linearisation with respect to vacancy concentration (see e.g. the commonly used Wagner-Schottky model [4]) and sometimes even an a priori assumption of the existence of the triple defect [5]. In the present investigation the Ising-type binary B2-ordering system with thermal vacancies is modelled without the above restrictions. It is shown that the formation of triple defects and structural vacancies follows naturally from appropriate interatomic energetics assumed.

2. Model

The model stems from the one proposed by one of the present authors [6]. A B2-ordered A-B binary containing vacancies is modeled with an Ising Hamiltonian with nearest-neighbour (nn) pair interaction energies. The configurational thermodynamics is treated within the Bragg-Williams approximation at pressure p = 0. Vacancies are regarded as a ternary component. In this approximation the free energy f of the system per one lattice site is given by:

$$f = \frac{1}{4}\sum_{i,k=1}^{3}\sum_{\mu,\nu=1}^{2} Z_{\mu\nu} p_{i\mu} p_{k\nu} V_{ik} + \frac{1}{2} k_B T \sum_{i}^{3}\sum_{\nu}^{2} p_{i\nu} \ln p_{i\nu} \tag{1}$$

where: greek and latin indices enumerate sublattices and components, respectively (i=1 and i=2 means A- and B-atoms, respectively, i=3 means vacancies); Z is the nn co-ordination matrix for the B2 superstructure ($Z_{\mu\nu} = 8$ ($\mu \neq \nu$); $Z_{\mu\nu} = 0$ ($\mu = \nu$), see Fig. 1); $p_{i\mu}$ is the probability for an i-atom occupying a μ-th sublattice site; V_{ik} is the i-k nn pair interaction energy (it is assumed that $V_{33} = 0$); k_B and T are Boltzmann constant and absolute temperature, respectively.

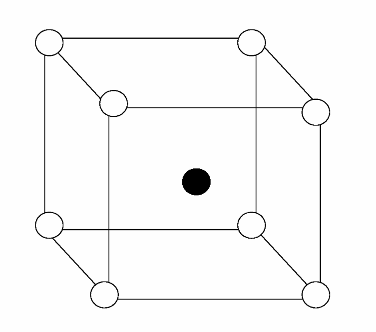

Fig. 1 Scheme of the B2-type superstructure: (open circles) sublattice 1 occupied by A-type atoms (solid circles) sublattice 2 occupied by B-type atoms.

Normalisation of $p_{i\mu}$ is assured by fulfilling a system of linear equations involving the concentrations of the component atoms (c_A, c_B) and vacancies (c_V) which yield two independent variables, for the sake of the present study defined as: $S = p_{11} - p_{12}$ (atomic LRO parameter) and $P = p_{31} - p_{32}$ (vacancy LRO parameter). Finally, the functional f (Eqn 1) is parameterised by S, P, the vacancy concentration c_V, the ratio c_A/c_B and 5 pair-interaction energy parameters defined as: $W = 2V_{12} - V_{11} - V_{22}$; $E_{asymm} = V_{11} - V_{22}$; V_{22}; V_{13} and V_{23} ; ($V_{33} = 0$).

It is then assumed that the A-B crystal is surrounded by vacuum considered as an infinite reservoir of vacancies. It is postulated that the equilibrium vacancy concentration corresponds to equal chemical potentials μ_V of vacancies in the crystal and in the reservoir, where in view of $V_{33} = 0$, $\mu_V = 0$.

Temperature dependencies of the equilibrium values of the parameters S, P and the vacancy concentration c_V in the system with particular values of the pair-interaction energy parameters were determined in two stages: (i) the functional f (Eqn 1) was minimised at given T with respect to S and P for a range of $0 < c_V < 1$; (ii) the equilibrium value of c_V (T) yielding $\mu_V = 0$ was found following the procedure described in [6].

3. Results

Tab. 1 shows three sets of the pair-interaction energy parameters used in the calculations and chosen in the way that: (i) B2 superstructure stability is almost fixed (W=const); (ii) vacancies form preferentially on sublattice 1 ($V_{11}<V_{22}$ [6]). The latter preference is gradually enhanced

by the consecutive sets of parameters: in the case of SET3 it is additionally increased by the non-zero values of V_{13} and V_{23}.

Table 1. Pair interaction energy parameters used in the calculations

	W [eV]	E_{asymm} [eV]	V_{22} [eV]	V_{13} [eV]	V_{23} [eV]
SET1	-0,08	-0,03	-0,05	0,0	0,0
SET2	-0,08	-0,07	-0,05	0,0	0,0
SET3	-0,08	-0,07	-0,05	0,051	-0,051

The triple defect is a cluster containing an antisite defect and two vacancies on the opposite sublattice. The tendency for its generation in the system was, therefore, tested by analysing the temperature dependence of a ratio between the antisite and vacancy concentrations $c_{ant}/c_V = (p_{12} + p_{21})/(p_{31} + p_{32})$.

Fig.2 shows the results obtained for a stoichiometric AB system using the particular pair-interaction energy sets (Tab. 1).

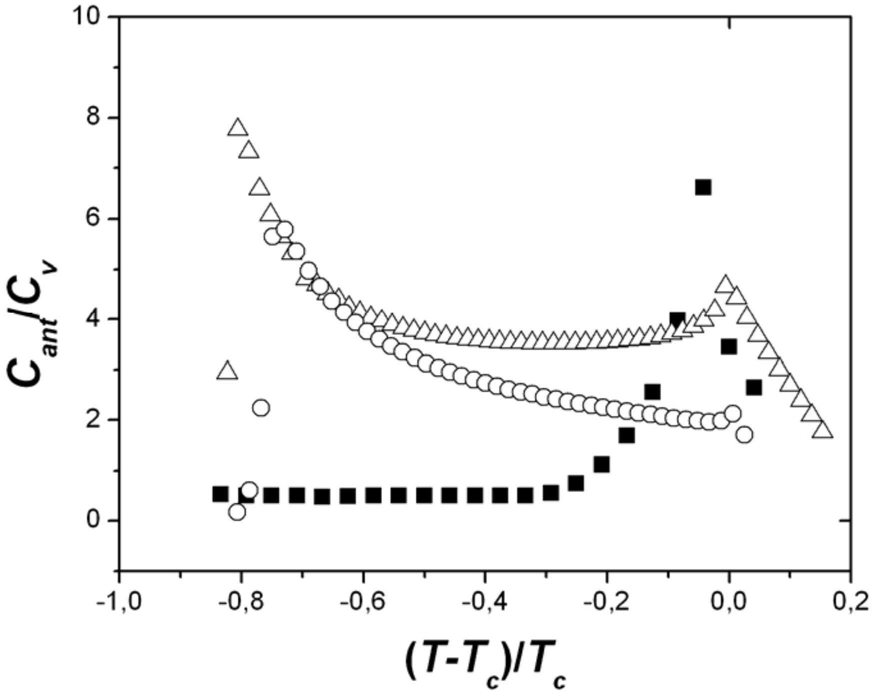

Fig.2. Ratio of antisite concentration over vacancy concentration in a stoichiometric AB binary against reduced temperature (T_C is the “order-disorder” transition point) calculated for the pair interaction energy of SET1 (open circles), SET2 (open triangles) and SET3 (solid squares).

Except for specific anomalies around $T = T_C$ (not discussed in this short report) the curves corresponding to SET2 and SET 3 show well defined plateau which indicate the proportionality between c_{ant} and c_V within the corresponding temperature range in the B2 domain. In the case of SET3 $c_v \approx 2\times c_{ant}$ up to $(T-T_C)/T_C \approx -0.3$ and almost all vacancies occupy sublattice 1. This corresponds to the disordering process running purely by creating triple defects. A decrease of vacancy formation preference on sublattice 1 (SET2 and SET1) reduces the temperature range of c_{ant}/c_V = const. and increases the value of this ratio. It is interesting that as long as the plateau appears c_{ant}/c_V always equals an odd multiple of ½. This result may be very much meaningful for the ordering kinetics and will be thoroughly studied by means of kinetic MC simulations.

The calculations performed for non-stoichiometric binaries using the energetics of SET3 revealed: (i) triple defect formation in A-atom-rich systems and (ii) structural vacancy formation in B-atom-rich systems.

The latter effect is illustrated by Fig.3.

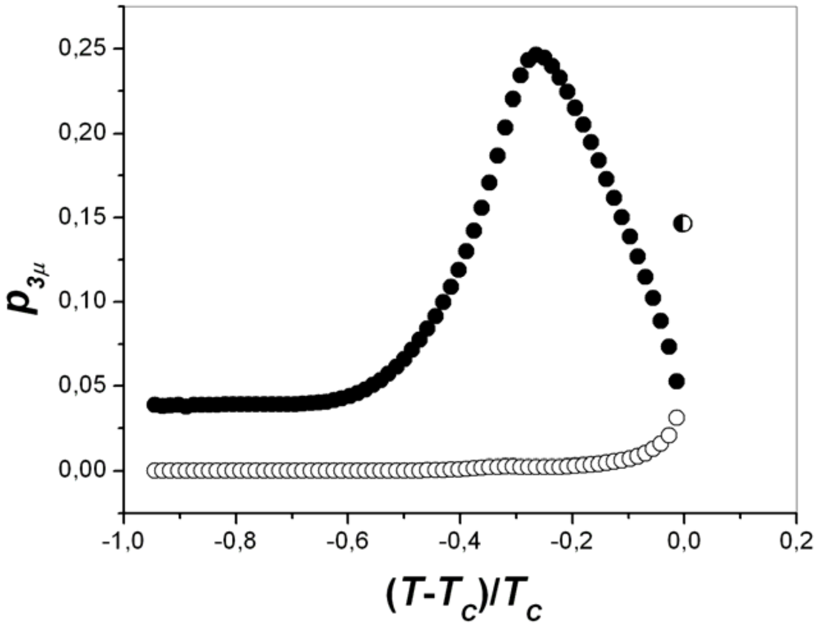

Fig.3. Probabilities for vacancy occupying 1-sublattice sites (solid circles) and 2-sublattice sites (open circles) in the off-stoichiometric B2-ordered binary system $A_{49}B_{51}$ with SET3 pair-interaction energy parameters. The point marked by a half-solid circle corresponds to $T > T_C$, where $p_{31} = p_{32}$.

It is definitely visible that vacancy concentration on the 1-sublattice of $A_{49}B_{51}$ does not extrapolate to zero for $T \rightarrow 0$ K, which indicates the presence of structural vacancies. It is also interesting to remark the anomalous temperature dependence of p_{31} in the vicinity of T_C – the effect will be discussed in a more extended paper, which is in preparation.

In conclusion it is stressed that two important features: formation of triple defects and presence of structural vacancies in B2-ordered A-B binaries were consistently modelled within the Bragg-Williams approximation with no a priori assumption of the existence of the defects.

References:

[1] R. Kozubski, D. Kmieć, E. Partyka, M. Danielewski, Intermetallics, **11**, 897, (2003).
[2] H.-E. Schaefer, K. Frenner, R. Würschum, Intermetallics, **7**, 277, (1999).
[3] P. Oramus, R. Kozubski, V.Pierron-Bohnes, M.C.Cadeville, W.Pfeiler, Phys.Rev.B, **63**, 174109/1-14, (2001).
[4] P.A. Korzhavyi, A.V. Ruban, A.Y. Lozovoi, Yu.Kh. Velikov, I.S. Abrikosov, B. Johansson, Phys. Rev. B, **61**, 6003, (2000).
[5] J. Breuer, F. Sommer, E.J. Mittemeijer, Metall. Mater. Trans., **32A**, 2157, (2001).
[6] R. Kozubski, Acta Metall.Mater., **41**, 2565, (1993).

The study of magnetism and the ideal tensile strength in Ni_3Al and Fe_3Al

Dominik Legut[1], *Mojmír Sob*[2]

[1]*Institute of Physics of Materials of the Academy of Sciences of the Czech Republic, Zizkova 22, 61600 Brno, Czech Republic*

[2]*Department of Theoretical and Physical Chemistry, Faculty of Science, Masaryk University, Kotlarska 2, 611 37 Brno, Czech Republic*

Both Ni_3Al and Fe_3Al intermetallic compounds are highly demanded for technological applications. The main advantages are high strength at the elevated temperature, very good creep and oxidation resistance. However, the main drawback concerns the brittleness of polycrystalline Ni_3Al at ambient temperature. The presented results were calculated within the framework of the fullpotential linearized plane wave method, using WIEN97 and Wien2k code employing both local density [1] and generalized gradient approximation [2]. The total energy calculations show that the ground-state of Ni_3Al, the $L1_2$ structure is ferromagnetic in spite the choice of the exchangecorrelation term [3]. We can confirm the possession of wrong ground-state in the case of Fe_3Al within the spin-polarized GGA calculation, giving the preference to the $L1_2$ structure, as reported in [4]. The LDA calculations give the right ground-state with or without the spin-polarization. The elastic properties, such as bulk modulus, trigonal C_{44} and tetragonal C′ shear moduli were determined for both Ni_3Al and Fe_3Al ground-state structures. In our investigation we also concern mutually reversed structures, i.e. the $L1_2$ structure for Fe_3Al and $D0_3$ structure in the case of Ni_3Al. The high-energy structure of $D0_3$ of Ni_3Al is found to be non-magnetic, whereas the $L1_2$ structure of Fe_3Al has ferromagnetic ground-state. The ideal tensile strengths of intermetallic compounds Ni_3Al and Fe_3Al were calculated for the ground-state and high-energy structures employing both LDA and GGA for the exchange-correlation term. The loading directions were [001] and [111] for the $L1_2$ structure and [111] for the $D0_3$ structure. The maximum accomodation of stress within the Ni_3Al in $L1_2$ structure reaches 28.5 (40.1) GPa along the [111] and 36.1 (43.7) GPa along the [001] loading direction within the GGA (LDA). The ideal strength of Fe_3Al is little bit lower, 20.2 (32) for the GGA (LDA) under the trigonal loading, respectively. The calculated maximum stresses were compared with the trigonal and tetragonal shear moduli obtained from displacive transformation paths [3]. We have also performed an analysis of the magnetic behavior during the tensile test with respect to the local atomic environment. The interpretation of lost/gained magnetic moment per atom is discussed on the basis of the Stoner model.

[1] J.P. Perdew and Y. Wang 1992, Phys. Rev., B 45 13244, 1992

[2] J.P. Perdew, K. Burke, and M. Ernzerhof, Phys. Rev. Lett., 77 3865, 1996.

[3] M. Sob, M. Friak, D. Legut, J . Fiala and V. Vitek, Mat. Sci. Eng. A 387-389 148, 2004.

[4] F. Lechermann, F. Welsch, C. Elsässer, C. Ederer, and M. Fähnle, Phys. Rev. B 65 132104, 2002.

The evolution of colloidal crystal microstructure during drying

Qin Li[1,2], *Ulrich Jonas*[1]

[1]*Max-Planck Institute for Polymer Research, Ackermannweg 10, 55128 Mainz, Germany*
[2]*Department of Chemical Engineering, Curtin University of Technology, GPO Box U1987 Perth, Australia*

The self-assembly strategy to form colloidal crystals has received a great deal of recent research interest due to its significant potential in the applications of photonics, catalysis, and bio-/chemo-sensors, as well as its simple and cost-effective procedures. Experimental studies and theoretical analysis have speculated that capillary forces play a pivotal role in forming the colloidal crystals during the crystal growth process, and that particularly during the drying stage the changing of the magnitude of capillary forces appear critical to the resultant microstructure. Our recent computational study has quantified and demonstrated the dynamic change of capillary forces between a pair of particles when the liquid bridge is evaporating. In this contribution we will provide an analysis on classification of different stages in colloidal crystal formation by vertical deposition, based on the varying predominant mechanisms. The focus of this study is computational simulations to illustrate the formation of various microstructures from a 'semi-dry' colloidal cluster due to the dynamic changes of liquid bridges in Drying Stage II. The simulation results may assist in designing refined strategies for controlling colloidal crystal formation.

Modeling Surfaces, Interfaces and Compositional Order in Ferroelectric Materials

Bernd Meyer

Ruhr-Universität Bochum, Lehrstuhl für Theoretische Chemie, 44780 Bochum, Germany

The cubic perovskite oxides ABO3 show great promise for the development of new materials having improved ferroelectric and electromechanical properties by tuning their chemical composition. The solid solutions with stoichiometric substitutions of the A or B metal atoms, like PZT, PZN or PMN-PT, are some of the promising examples. Based on ab-initio density functional calculations we propose that it may also be possible to optimize desired materials properties by additionally tuning the degree and type of compositional order in these compounds. Artificially layered structures with different cations which compositionally break the inversion symmetry of the perovskite structure might be especially exciting and fruitful in this regard. The resulting asymmetry of the ferroelectric double-well potential in such a material suggests the prospect of qualitatively new behavior, e.g., ``self-poling'' materials.

In the second part of the talk we will address how surfaces and interfaces, e.g., domain walls, influence the ferroelectric properties of prototype cubic perovskite compounds. In particular the question whether an intrinsic critical thickness exists below which ultrathin films loose their ferroelectric properties will be discussed, an issue which is very important for the application of ferroelectric thin films in semiconductor devices.

EFFECT OF SLIDING RATE ON FRICTION IN POLYTETRAFLUOROETHYLENE (PTFE)

Peter R. Barry, Inkook Jang, Susan B. Sinnott, Simon R. Phillpot*

Department of Material Science and Engineering
University of Florida, Gainesville, FL 32611
***sphil@mse.ufl.edu**

ABSTRACT

Polytetrafluoroethylene (PTFE) has been extensively studied for its oxidative and thermal stability as well as its low frictional coefficient. We report on the results of molecular-dynamics simulations of friction in PTFE and show that the tribological properties are independent of the rate of sliding.

1. INTRODUCTION

The dry vacuum of space is a very different environment from the humid, multi-gaseous environment of earth. This makes the testing of tribological systems for space applications extremely difficult on earth. The development of tribological systems that work equally well in terrestrial and space environments is thus highly desirable. Nanostructured polymer composites are good candidate materials for such systems. In particular, PTFE is being explored as either a filler or a matrix in such nanocomposites. The C-F bond in PTFE provides both thermal and oxidative stability, and the strong interchain interactions in PTFE confer resistance to almost all solvents [1]. However, PTFE is known to have poor wear resistance, a problem that can be ameliorated by incorporation with nanoscopic fillers of a low wear material. For example, Sawyer *et al.* created a nanocomposite of PTFE with alumina that has a reduction in wear rate of over two orders of magnitude compared with unfilled PTFE [2].

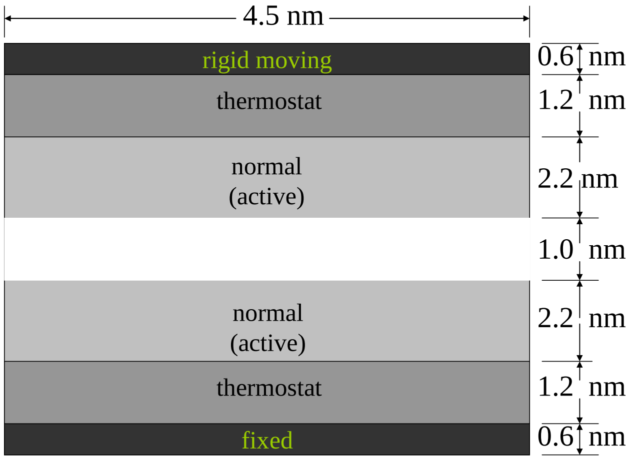

Figure 1 Schematic of the simulation set up. Both the top and bottom slabs of PTFE consist of three layers: the outer layers are held rigid with the relative atom positions fixed; the atoms in the thermostat layers are maintained at a temperature of 300K. The atoms in the normal (active) regions evolve over the course of the simulations without

We are currently using large scale molecular-dynamics (MD) simulations to identify the microscopic processes associated with the low-friction behavior in these materials. Here we report the results of systematic studies of the effects of the sliding rate on the simulated values of the friction coefficient, the forces on the system, and the atomic-level processes associated with friction.

Experimental sliding rates are typically of the order of millimeters per second; however such slow rates are not accessible to conventional MD simulation. The objective of this study is to establish that the simulation conditions in the range of sliding rates that is accessible to simulation (>1 m/s) can be expected to give reliable information on the frictional behavior.

2. METHODS

An illustration of the system setup is shown in Fig. 1. Each of the PTFE films used in the simulations consists of seven layers of chains (oriented horizontally) for a total thickness of 4 nm and sliding surface area of 4.5 nm x 4.5 nm. During the simulation, the bottom layer of the lower film is held fixed, while the top layer of the upper film moves as a single rigid unit, thus allowing for the consideration of both compression and sliding. The two layers adjacent to the fixed and moving rigid regions are thermostated with Langevin dissipative and stochastic forces [3] to maintain the temperature at 300K. The remaining two layers of atoms in each half of the system, designated as normal (active) atoms, are not constrained and can evolve freely under the forces produced across the tribological surface. Initially, the distance between the upper and lower films is set at 1 nm. Periodic boundary conditions [3] are applied within the plane of the film surface to mimic an infinite interface. After the system is thermally equilibrated at 300K, the two films are compressed by moving the upper film towards the lower film at a constant rate of 10 m/s. When the desired compression of a few hundred MPa is reached, the system is further equilibrated with the objective of producing a steady and constant normal force during sliding. Finally, the films are slid against each other by moving the upper film in a direction parallel to the plane of the lower film surface at a constant rate.

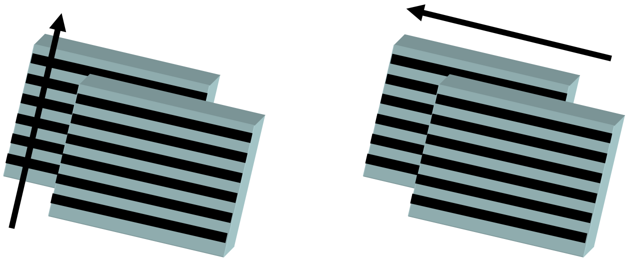

Figure 2a (left) Perpendicular sliding configuration. **Figure 2b** (right) Parallel sliding configuration. The arrow indicates the direction of sliding for the upper film.

This study is conducted using classical MD simulations that numerically integrate Newton’s equations of motion with a third-order Nordsieck predictor corrector [3] using a timestep of 0.2 fs. Short-range interatomic forces are calculated using the C-H-F reactive empirical bond order (REBO) potential [4] based on Brenner’s second generation REBO potential for hydrocarbon systems [5]. Long-range van der Waals interactions are included in the form of a Lennard-Jones (LJ) potential to calculate interchcain interaction [3]. The LJ potential is only active at distances greater than the covalent bond lengths.

3. EFFECT OF SLIDING RATE

To examine at the molecular level the effect of rate of sliding on the frictional behavior of the PTFE films, two different sliding scenarios are considered: (i) the chains in both the upper and lower films are perpendicular to the sliding direction (perpendicular configuration, Fig. 2a), and (ii) the chains in both the upper and lower films are parallel to the sliding direction (parallel configuration, Fig. 2b).

3.1 Normal and Frictional Forces

Frictional properties often vary strongly with temperature; therefore, before analyzing the frictional behavior, it is important to establish that the system's temperature is maintained despite the energy added by the friction and wear at the interface. It is found that for sliding rates of 5 – 20 m/s the temperature of the system remains within about 10% of the nominal 300K simulation temperature. However, for simulations with a sliding rate of 50 m/s, the system temperature is found to increase significantly for perpendicular sliding. We therefore conclude that 20m/s is the maximum rate of sliding for which reliable friction results can be obtained.

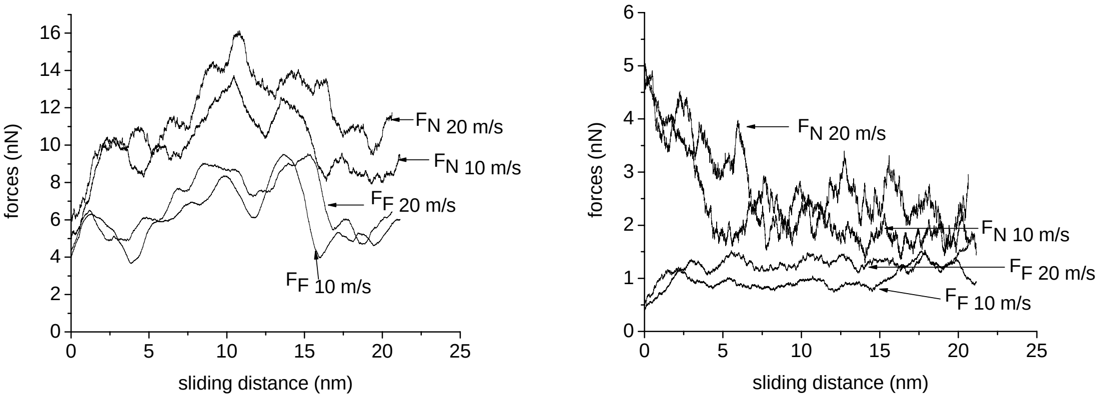

Figure 3a (left) and **Figure 3b** (right) show the normal (F_N) and frictional (F_F) forces for the perpendicular and parallel sliding configurations respectively, at 10 m/s and 20 m/s sliding speeds.

Fig. 3 shows the normal and tangential forces for both perpendicular and parallel sliding configurations for sliding rates of 10 and 20 m/s. For both configurations, the normal force is consistently higher than the tangential force; thus, giving coefficients of frictions that are less than unity. Furthermore, although the values of the normal forces for both the perpendicular and parallel sliding configurations are initially identical (approximately 5 nN),

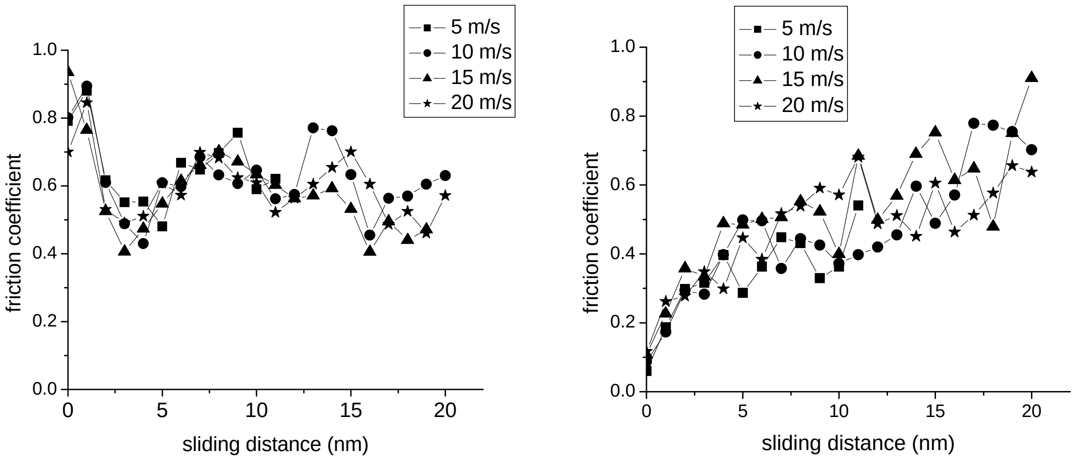

Figures 4a (left) and **4b** (right) show the coefficient of friction for the sliding of PTFE films at various speeds in the perpendicular and parallel configurations respectively. The data points, connected by lines to guide the eye are averaged over 1nm of sliding.

the normal force for the former fluctuates while that of the latter remains fairly constant after a gradual drop. This arises because in perpendicular sliding configuration, the normal force is larger when chains from the upper film are directly on top of chains in the lower film, and somewhat lower when the chains from the upper film fit in the interchain grooves of the lower film. In the case of parallel configuration sliding, the chains from the upper film remain in the interchain grooves of the lower film during sliding; hence, there are weaker variations in the normal force. Similar force curves are obtained at 5 m/s and 15 m/s. This finding illustrates the importance of molecular configuration on the evolution of the system.

3.2 Friction Coefficient

In analogy with the usual macroscopic definition, the microscopic coefficient of friction, μ, is defined as the ratio of the frictional to the normal force: $\mu = F_F/F_N$. Figs. 4a and 4b illustrate the evolution of the coefficient of friction with sliding distance at various sliding rates in the perpendicular and parallel configurations. Here μ is determined from the sliding distance averaged forces shown in Fig. 3; using this ratio of the averages significantly reduces the noise in the calculated values. Although there are small variations, the overall trends are remarkably similar at all four speeds, which suggests that the microscopic processes are also similar (see Sec. 3.3)

3.3 Microscopic Processes

The analysis above has been on spatially and temporally averaged properties of the system. To examine behavior at the microscopic level, Fig. 5 shows three snapshots from the perpendicular sliding simulation. Each is an edge-on view of the system in which the top layer of the top half is sliding to the left at a fixed rate. To clarify the atomic-level processes that are occurring, three initially vertical slices of atom are visualized. The positions of the same atoms in their initial positions are shown in the left-hand panel, and are shown after 10nm of sliding at 5 m/s and 20 m/s in the centre and right-hand panels. While there are clearly some microscopic differences between the two systems, the general level of damage (e.g., number of small polymeric fragments) and the roughness of the tribological surface are rather similar. This illustrates how the similarity in the evolution of the tribological properties is a reflection of the similarity of the evolution at the microscopic level.

4. DISCUSSION

The results presented here indicate that molecular-scale tribological behavior does not vary to any significant degree for sliding rates of 5 m/s to 20 m/s. This suggests that the dominant physical mechanisms identified in the simulations can be applied to the interpretation of experimental data despite differences in the sliding rates in simulations and experiments.

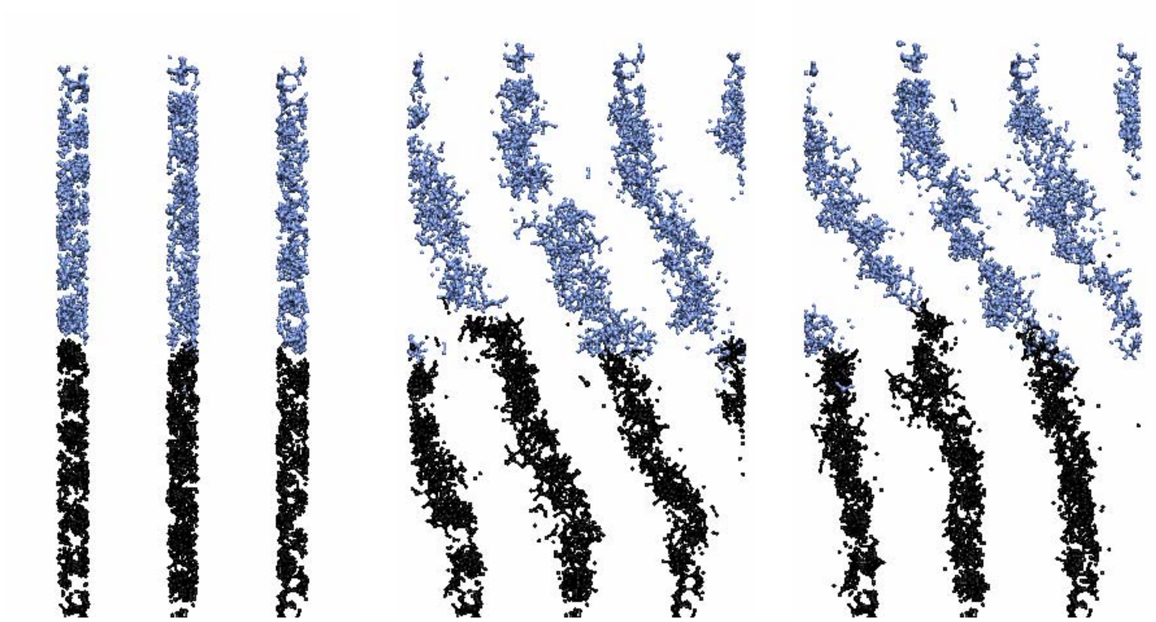

Figure 5 Edge on view for perpendicular sliding. The left panel shows the initial configuration with only three vertical stripes of atoms shown. After 10nm of sliding at 5m/s (left) and 20 m/s (right) of sliding, the surface has roughened to approximately the same degree.

ACKNOWLEDGEMENTS

We are happy to acknowledge many useful discussions with Drs. W. G. Sawyer and S. S. Perry. This work is supported by a MURI from the Air Force Office of Scientific Research through grand FA9550-04-1-0367.

REFERENCES

1. H. R. Allcock, F. W. Lampe, and J. E. Mark, Contemporary Polymer Chemistry, 3rd ed. (Pearson/Prentice Hall, Upper Saddle River, N.J., 2003)
2. W. G. Sawyer, K. D. Freudenberg, P. Bhimaraj, and L. S. Schadler, Wear **254**, 573 (2003)
3. M. P. Allen and D. J. Tildesley, Computer Simulation of Liquids (Oxford University Press, New York, 1987).
4. I. Jang and S. B. Sinnott, Journal of Physical Chemistry B **108**, 18993 (2004)
5. D. W. Brenner, O. A. Shenderova, J. A. Harrison, S. J. Stuart, B. Ni, and S. B. Sinnott, Journal of Physics-Condensed Matter **14**, 783 (2002)

Simulation of thermoelastic and electrical properties of sintered ceramics

Friedrich Raether

Fraunhofer Institut fuer Silicatforschung, Neunerplatz 2, 97082 Wuerzburg, Germany

Ceramic materials are composed of various phases which can differ in their individual thermal, elastic or electrical properties by orders of magnitude. The microstructural arrangement of the phases controls important material properties of the ceramics. To simulate these macroscopic material properties from the material properties of the constituting phases, a 3d FEM model is used. The key for an adequate description of real materials is the accurate three dimensional modelling of their microstructure. Basic morphological parameters of many ceramics are reflected by a modified Voronoi model, e.g.: the volume fractions, grain size ratios and contiguity of the phases. By automatically generating thousands of test structures and comparing them to quantitative data derived from image analysis of scanning electron micrographs, structures are selected which closely fit to the microstructure of experimental samples.

The model considerations are illustrated on two types of bi-continuous ceramic materials, a porous alumina (Al_2O_3) and a dense zirconia toughened alumina (ZTA) ceramic. Using different volume fractions of the phases many types of microstructures are exemplified. For these two ceramic systems, elastic moduli, thermal conductivity and electrical conductivity are calculated and compared to experimental data of samples of the respective microstructure. Differences between simulated and measured material properties are interpreted in terms of grain boundary and lattice strain effects.

CORRELATED OXIDE HETEROSTRUCTURES AND NANOSTRUCTURES

Ramamoorthy Ramesh

University of California, Berkeley, Department of Materials Science and Engineering, 210 Hearst Memorial Mining Building, 94720 Berkeley, USA

Complex perovskite oxides exhibit a rich spectrum of functional responses, including magnetism, ferroelectricity, highly correlated electron behavior, superconductivity, etc. The basic materials physics of such materials provide the ideal playground for interdisciplinary scientific exploration. Over the past decade we have been exploring the science of such materials (for example, colossal magnetoresistance, ferroelectricity, etc) in thin film form by creating epitaxial heterostructures and nanostructures. Among the large number of materials systems, there exists a small set of materials which exhibit multiple order parameters; these are known as multiferroics. Using our work in the field of ferroelectric and ferromagnetic oxides as the background, we are now exploring such materials, as epitaxial thin films as well as nanostructures. Specifically, we are studying the role of thin film growth, heteroepitaxy and processing on the basic properties as well as magnitude of the coupling between the order parameters. A very exciting new development has been the discovery of the formation of spontaneously assembled nanostructures consisting of a ferromagnetic phase embedded in a ferroelectric matrix that exhibit very strong coupling between the two order parameters. This involves 3- dimensional heteroepitaxy between the substrate, the matrix perovskite phase and spinel phase that is embedded as single crystalline pillars in this matrix. In this talk I will describe to you some aspects of such materials as well as the scientific and technological excitement in this field

Micro-Modeling of solid-oxide-fuel-cell electrodes

Bernd Rüger[1], *Daniel Fouquet*[1], *Vincent Heuveline*[2], *Ellen Ivers-Tiffée*[1], *André Weber*[1]

[1]*Institut für Werkstoffe der Elektrotechnik, Universität Karlsruhe (TH), Adenauerring 20b, 76131 Karlsruhe, Germany*
[2]*Rechenzentrum, Numerik auf Hochleistungsrechnern, Universität Karlsruhe (TH), Adenauerring 20b,*
76131 Karlsruhe, Germany

Modeling of solid oxide fuel cells includes different length scales, from the entire cell in the centimeter range down to its microstructure with dimensions in the order of microns, and different time scales, from the range of seconds (gas diffusion) down to the nanosecond regime (electrical phenomena). The electrical performance of the cell is determined by the composition and microstructure of the electrodes and the electrolyte /electrode interface.

In this paper, a modeling approach is presented which allows an evaluation of SOFC performance for cermet based anodes. The model is implemented in two different finite element method programs (HiFlow and COMSOL3.2) and provides the area specific resistance (ASR) of the electrode.

The modeling approach is used to examine the performance of Ni/YSZ and Ni/ScSZ cermet anodes. The complex electrode microstructure is approximated by a randomly generated geometry. Polarization losses are modeled with an ASRp. The model can be fitted to measured data by changing the value of ASRp. The two material systems Ni/YSZ and Ni/ScSZ show a different ASRp, exhibiting Arrhenius type temperature dependence. Based on the ASRp, the performance of an anode exhibiting different sized or even graded microstructures can be calculated.

New Studies of Ferromagnets, Ferroelectrics, and Magnetoelectrics

J. F. Scott

Earth Sciences Department, University of Cambridge, Downing Street, Cambridge, UK, CB2 3EQ: jsco99@esc.cam.ac.uk gcat05@esc.cam.ac.uk

ABSTRACT

I discuss some new results on ferroelectrics and magnetoelectrics: First an extension is given of the Kittel 1946 relation between domain widths and sample thickness; second, a discussion is presented of how the combined effects of magnetoresistance and Maxwell-Wagner space charge can produce large magneto-capacitance in materials that are not ferroelectric; third, I discuss the origin of unusual "critical" exponents in ferroelectrics and show that they can arise from defects; and finally I show the evidence for skyrmion emission of nano-domains in both ferroelectrics and ferromagnets.

1. Introduction

The study of magnetoelectric materials began in 1957 with the predictions by Dzyaloshinskii of a linear magnetoelectric effect in antiferromagnetic Cr_2O_3, soon verified by Astrov in 1960. The following fifteen years saw a flurry of activity on this topic, headed by Hans Schmid in Geneva and emphasizing the boracites. Unfortunately the boracites are complex in structure, with typically 96 atoms per primitive cell and triclinic symmetry; combined with an awkward growth habitat (small needles), they were unappealing to either theoreticians or experimentalists. More recently interest in magnetoelectrics (now usually termed "multiferroics") has resurrected, with emphasis upon Tb and Mn compounds.

2. Basic mechanisms

2.1 Fox-Scott model of ferromagnetism induced by ferroelectricity in $BaMF_4$

The magnetoelectric effect is a coupling between polarizations P in a ferroelectric or antiferroelectric and magnetization M in a ferro-, ferri-, or antiferro-magnet:

$$H = \alpha_{ij} <P_i><M_j> + \beta_{ijk} <P_i><M_jM_k>. \qquad (1)$$

Note that this Hamiltonian is not time-reversal invariant. Here the linear magnetoelectric effect due to a_{ij} vanishes above T_N (or T_c), since $<M> = 0$; however, the quadratic term due to b_{ijk} is proportional to $<M^2>$ -- the rms value of magnetization – and remains finite well above T_N (until $T \approx 3T_N$ in magnets such as $BaMnF_4$ with [2D] planar spin ordering).

If we wish to switch a magnetic domain with an electric field, we need to know how much the magnetization M depends upon the polarization P. Does reversing P influence M by 1%, 10%, or 100%? The idea that ferroelectricity could actually *cause* ferromagnetism (a 100% effect) was proposed by Fox and Scott (1) and independently by Janovec (2) and exemplified with the $BaMF_4$ family (M = Mn, Ni, Co, Fe and mixed $BaM_{1-x}M'_xF_4$ compounds). Janovec's article is group-theory based and therefore cannot predict magnitudes but shows which domain walls in which point groups can exhibit the effect. The Fox-Scott model gives predicted magnitudes, based upon a microscopic model of Dzyaloshinskii-Moriya anisotropic exchange. By producing a weak ferromagnetic moment (canting of antiferromagnetic spin sublattices) $M_i = a_{ij} P_j$ through the Dzyaloshinskii-Moriya anisotropic exchange, the ferroelectric polarization can produce this effect in some symmetry groups (e.g., 2' in $BaMnF_4$) but not others (e.g., 2 in $BaCoF_4$). The angle of spin canting (3 mrad = 0.17 degrees in $BaMnF_4$) implies a plausible value for the anisotropic exchange in comparison with off-diagonal a_{ij} in other Mn^{+2} compounds). This Fox-Scott model has recently been applied to $BaNiF_4$ and developed in the context of *ab initio* models by Ederer and Spaldin (3); it can also produce ferromagnetism within domain walls in antiferromagnets (Catalan, Daraktchiev, and Scott, unpublished), perhaps reconciling conflicting $BiFeO_3$ data, where the initial claim of strong magnetism was shown to be due mostly to Fe mixed valence and oxygen vacancies; the latter explanation does not seem to explain away all the measured value of M. The Fox-Scott model is a bulk effect; weaker coupling between magnetic and ferroelectric domain walls has been demonstrated by Cheong's group at Rutgers that is also of great theoretical interest.

2.2 Domain widths

The basic relationship between domain stripe widths w and crystal thickness d was first given by Kitten (4) for ferromagnets and extended to ferroelectrics by Mitsui and Furuichi (5) and to ferroelastics by Roytburd (6):

$$w^2 = a\, d \tag{2}$$

This equation works well for both ferromagnets and ferroelectrics, from 2 nm to 2 mm, as shown in Fig.1:

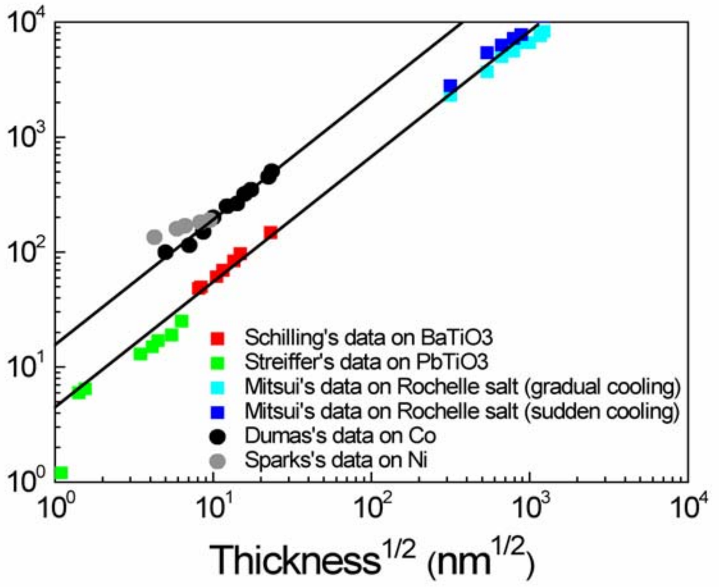

Fig. 1. Domain stripe width w in nm versus the square root of thickness d in nm. From A. Schilling et al., Phys. Rev. B (in press 2006).

More recently Catalan and Scott have shown (5) that

$$w^2 = a'd\delta, \quad (3)$$

where δ is the domain wall width and a' is given exactly by

$$a' = (2/3)\pi^3[\chi(a)/\chi(c)]^{1/2}/[7\ \zeta(3)] = 2.455\ [\chi(a)/\chi(c)]^{1/2}, \quad (4)$$

where $\chi(x)$ are the susceptibilities and $\zeta(3)$ the Riemann zeta function of power 3. This dimensionless equation works for magnets as well as ferroelectrics.

2.3 Magnetocapacitance

Catalan (7) and Catalan and Scott (7) have shown that magnetoelectricity is not required for large magnetocapacitance effects (change in dielectric constant ε when a magnetic field H is applied). In fact the material need not even be ferroelectric, let alone multiferroic. It can be cubic (as $CdCr_2S_4$ spinel probably is). All that is required is that the material be magnetoresistive and have some space charge. Assuming a Maxwell-Wagner description of the space charge – possibly due to Cl-ions from the growth flux -- Catalan and Scott have shown that this can explain the data published on Cd and Hg spinels from Augsburg. This may reconcile the latter reports with the theoretical model by Fennie and Rabe showing no ferroelectric phase transition (8) and the absence of magnetocapacitance effects in the Cl-free samples grown by Sang Cheol (9). The same arguments apply to the gigantic dielectric constants observed by Ramirez et al. in calcium copper titanate; the explanation of these effects as boundary layer capacitance in a ceramic by Sinclair et al. (10) and by Loidl et al. (11) met an attempted rebuttal by Ramirez that some of his samples were single crystals, but in the Catalan model, Maxwell-Wagner effects can still dominate at the electrode interfaces of single crystals, so we think the Ramirez conclusions are ill-founded.

3. Skyrmions

Dawber et al. (12) have shown this year that nano-domains nucleate in an applied field E in front of advancing domains in ferroelectric lead germanate above a threshold field. Similar effects in ferromagnetic iron garnet were shown much earlier by Randoshkin et al. The theory used to model these effects was the skyrmion description of Kudryavtsev, Piette, and Zakrzewski. This similarity of ferroelectrics and ferromagnets in emitting nano-domains as chiral topological defects is an interesting new analogy between magnets and ferroelectrics and indicates directions for further experiments on maximum switching speed at very high fields.

4. Critical exponents

There has been a burst of recent activity on fitting critical (fluctuation-dominated) exponents to behavior of ferroelectrics near their Curie temperatures. In O-18 valency strontium titanate Scott et al. (13) and Levstik and Filipic (13) showed however that these were erroneous and that the system is mean field. In the relaxor strontium barium niobate (“SBN”) Scott showed (14) that a defect model, originating with Larkin and Khmelnitskii and detailed by Levanyuk and Sigov appears superior in explaining existing data. The random field Ising model (RFIM) preferred by some others is known to violate thermodynamic hyperscaling. The key critical exponents from the defect theory are summarized in Tab.I. Here β describes the T-dependence of the order parameter P (polarization); α is the exponent describing specific heat $C_p(T)$ versus T; g is the T-dependent dielectric constant χ(T); and d, the dependence of P versus applied field E along the critical isotherm, $T=T_c$. The defect theory is invalid asymptotically near T_c and need not satisfy scaling relations. Tab. II is the dependence of the same exponents (14) for a universality class of dimension d=2.5, a number deduced experimentally by Paruch et al. (15) as the Hausdorff fractal dimension of switching dom,ain walls. The numbers in Tab. II are those of one of several possible sets. Table III shows (14) the dependence of the order parameter exponent β upon dimension d; the limited data suggest that β varies monotonically with d from 1/8 for [2D] to 5/16 for [3D] and ½ for infinite dimensions (quantum spherical model).

Table 1 Critical exponents in Levanyuk-Sigov defect theory

α	β	γ	δ
3/2	Ca. 0.4	5/2	2

Table 2 Critical exponents in d = 2.5 dimensions (one possible set satisfying scaling)

α	β	γ	δ
-1/2	1/4	2	9

Table 3 Critical exponent β as a function of dimensionality for Ising-like systems

Dimension d=2	d = 2.5	d = 3	d = infinity
1/8	1/4	5/16	1/2

The experimental values for SBN agree reasonably well with the defect values in Tab.I. Kalinin (private communication) reports new experimental data on domain nucleation and switching that agree with d = 2.5 assumed in Tab. II. A fuller description of β(d) as in Tab. III will be given by Zubko and Scott.

5. Nano-devices

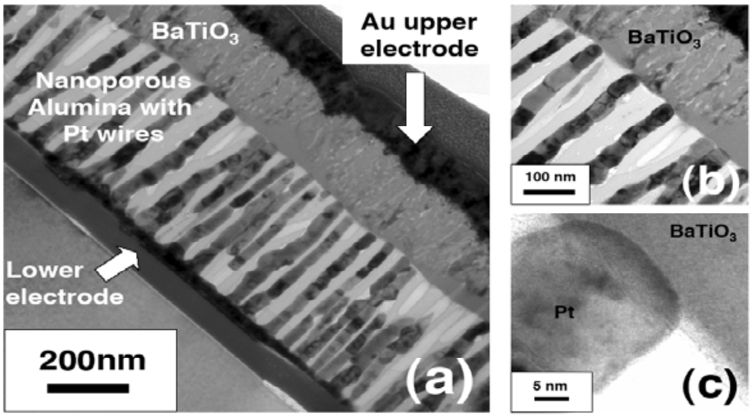

Fig.2. Electron micrographs of 0.3 GTb/sq.in. Pt nanowire array, terminated with ferroelectric barium titanate. Zhu et al., Appl. Phys. Lett. (in press 2006)

Most recently a Belfast-Cambridge collaboration has fabricated ferroelectric PZT (or barium titanate) arrays onto Pt nanowires, giving a bit density of 0.3 Tb/in.^{2} (300 Gb/sq.in.), several orders of magnitude greater than achieved before for ferroelectrics. This is shown in Fig.2. The present FRAM state-of-the-art FRAM is a 64 Mb PZT device from Samsung, for which an SEM cross section is shown in Fig.3. Note that this is 16x larger than the only magnetic RAM (MRAM) available to date (Freescale Co., July 2006).

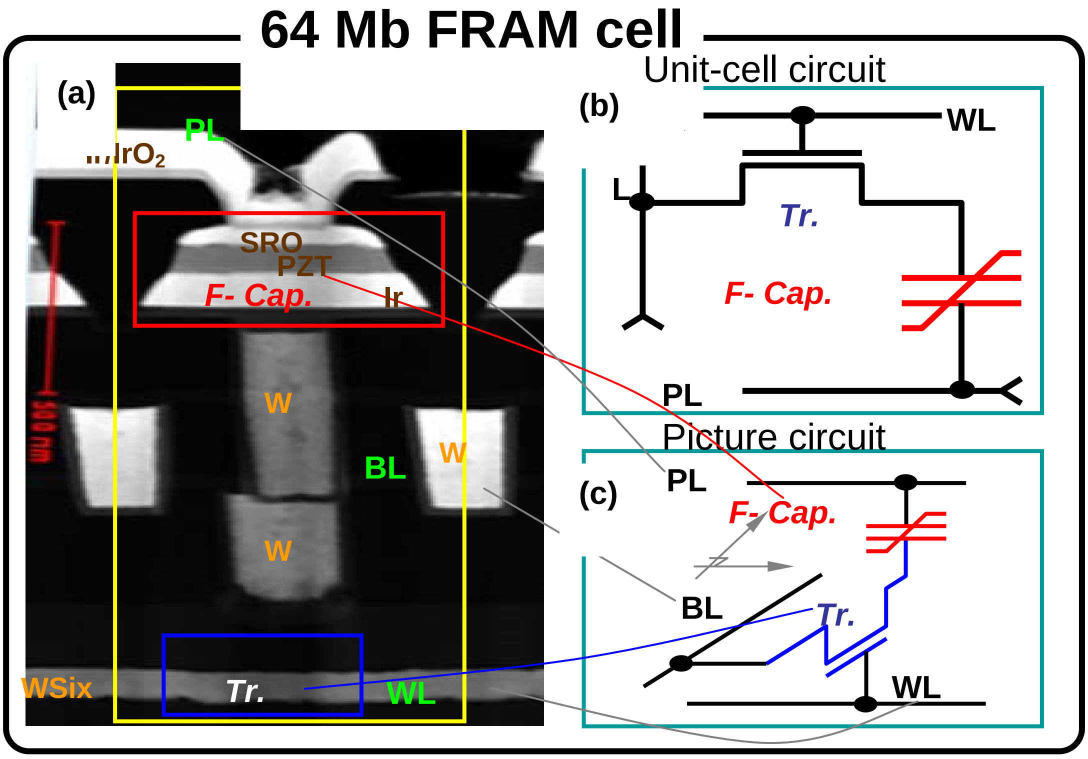

Fig. 3. A micrograph of a cross-sectional view showing a unit-cell structure of the 64 Mbit FRAM, recently developed in Samsung, 2006. (b) A schematic circuit diagram of one bit memory of 64 Mb FRAM with 1T1C cell configuration, consisting of both 1-transistor, one node of which is connected to bit-line (BL) to transfer data by accessing word-line (WL), and 1-capacitor, one of which is connected to plate-line (PL). (c) A schematic circuit diagram to become 1T1C memory such as (b), corresponding to the micrograph (a) . [Samsung Proprietary, used with permission.]

Acknowledgements

Work supported by the EPSRC.

References:

[1] D. L. Fox and J. F. Scott, J. Phys. C **10**, L329 (1977).
[2] J. Privratska and V. Janovec, Ferroelectrics **204**, 321 (1977).
[3] C. Ederer and N. A. Spaldin, Phys. Rev. **B74**, 020401 (2006); **B74**, 024102 (2006).
[4] C. Kittel, Phys. Rev. **70**, 965 (1946).
[5] T. Mitsui and J. Furuichi, Phys. Rev. **90**, 193 (1953).

[6] A. Roytburd, Physica Stat. Sol. **A37**, 329 (1976).
[7] G. Catalan, Appl. Phys. Lett. **88**, 102902 (2006); G. Catalan and J. F. Scott, Phys. Rev. Lett. (in press 2006).
[8] C. J. Fennie and K. M. Rabe, Phys. Rev. B **72**, 214123 (2005).
[9] K. M. Rabe (private communication).
[10] D. C. Sinclair, T. B. Adams, F. D. Morrison, and A. R. West, Appl. Phys. Lett. **80**, 2153 (2002).
[11] P. Lunkenheimer, R. Fichtl, S. G. Ebbinghaus, and A. Loidl, Phys. Rev. B **70**, 172102 (2004).
[12] M. Dawber, A. Gruverman, and J. F. Scott, J. Phys. Condens. Mat. **18**, L71 (2006).
[13] J. F. Scott, R. Pirc, A. Levstik, and C. Filipic, J. Phys. Condens. Mat. **18**, L205 (2006); C. Filipic and A. Levstik, Phys. Rev. **B73**, 092104 (2006).
[14] J. F. Scott, J. Phys. Condens. Mat. **18**, 7123 (2006).
[15] P. Paruch, T. Giamarchi, and J.-M. Triscone, Phys. Rev. Lett. **94**, 197601(2004).

Application of ab initio electronic structure calculations in construction of phase diagrams of complex systems

Mojmir Sob [1,2] *J. Vrestal* [1], *A. Kroupa* [2], *J. Houserova* [1,2]

[1] *Masaryk University, Faculty of Science, Brno, Czech Republic*
[2] *Institute of Physics of Materials, Academy of Sciences of the Czech Republic, Brno, Czech Republic*

We address the application of ab initio electronic structure calculations to modeling of phase equilibria and to construction of phase diagrams in binary and ternary iron systems containing complex intermetallic phases (e.g. sigma phase, Laves phases) in combination with the CALPHAD method. This approach is briefly outlined and utilization of ab initio total energy differences (lattice stabilities) for sigma phase is shown in Fe-Cr, Fe-Cr-Ni and Fe-Cr-Mo systems. Our description of sigma phase is included into a thermodynamic database for calculation of phase equilibria in steels, developed earlier by some of the authors. Theoretical results obtained by new and older models are compared with new experimental data for superaustenitic (high Ni and Cr) steels. In conclusion, some problems and challenges in application of ab initio results in the CALPHAD approach are outlined.

Proton Generation and Transport in the Fuel Cell Environment: Atomistic Computer Simulations

Author: Eckhard Spohr

Affiliation: Institut für Werkstoffe und Verfahren der Energietechnik (IWV-3), Forschungszentrum Jülich, D-52425 Jülich, Germany e-mail: e.spohr@fz-juelich.de

ABSTRACT

Hydrogen atoms in direct methanol fuel cells are produced 'in situ' by dissociation of methanol on precious metal catalysts (Pt, Pt/Ru) in an aqueous environment. The abstraction of the first hydrogen atom via C-H bond cleavage is generally considered to be the rate-limiting step of dissociative methanol adsorption on the catalyst surface. This oxidation reaction on platinum particles in a fuel cell is investigated by means of a combined approach of classical molecular dynamics (MD) simulations and ab initio calculations in order to obtain an understanding of the role of the solvent for the stabilization of intermediates and for the enhancement of proton desorption from the catalyst surface and subsequent transfer into the nearby polymer electrolyte membrane (PEM). The anodically generated protons need to migrate efficiently through the membrane to the cathode were they are consumed. At the same time water and methanol (in a direct methanol fuel cell) transport should be slow. Humidified PEMs are considered to consist of a nanometer-scale phase-separated bicontinuous network of polymer regions providing structural integrity and of aqueous regions providing the pathways for proton conduction. MD simulations provide a powerful theoretical tool for the investigation and clarification of the relationship between molecular structure and these transport phenomena. In order to atomistically model larger fractions of a humidified PEM, a coarse-grained model of humidified polymer electrolyte membranes has been developed.

1. Introduction

Low temperature fuel cells such as the hydrogen-fed polymer electrolyte membrane fuel cell (PEFC) and the direct methanol fuel cell (DMFC) are regarded as promising technologies to replace combustion engines and batteries in portable, mobile and stationary applications. Fuel cells convert chemical energy of combustion directly into electricity by spatial separation of the anodic oxidation of fuel and of the cathodic reduction of oxygen. Protons generated at the anode migrate to the cathode, where they recombine with oxygen anions to form water. The reactions lead to the non-toxic products H_2O and CO_2. The anodically generated electrons perform useful work in the external circuit. In practice, however, many substantial barriers still have to be overcome prior to a broad introduction of fuel cell technology into the energy market. These are all associated at the molecular level with transport processes in and between the various component materials of a fuel cell (see., e.g., Ref. [1]). From a thermodynamic viewpoint, fuel cells are open chemical systems whose performance depends strongly on the rate of electrocatalytic oxidation and reduction reactions *on the surface* of catalyst particles and of transport properties of various gases (e.g., O_2, H_2, CO_2, CH_4), ions (most notably protons) and liquids (water, methanol) *into* and *within* the materials from which a fuel cell is constructed.

Simulations of continuum models are able to describe fuel cells and their operation as a whole, as macroscopic electrical machines. They need the magnitude of dynamic parameters in order to aid in the optimization of the operating conditions for a given set of materials. However, most available experimental techniques are unable to investigate atomic level processes *in situ* during fuel cell operation. While progress is being made with the development of novel in situ techniques, characterization of materials and compounds is only one aspect of the technological challenge. The second aspect derives from the fact that present fuel cell materials for membranes, catalysts, and electrodes are far from being perfectly suited to fuel cell operation, due to their structural and dynamic properties. Consequently there is a large need for understanding molecular processes in such open thermodynamic systems, which occur on various time scales, to aid the development of ideas and concepts for designing new, improved materials with higher performance and stability and lower prices. Such processes concern the electrocatalytic oxidation and reduction reactions on the fuel cell anode and cathode, the ionic transport through the membrane and in the mixed three-phase region, where the electronically conducting metal and graphite phases, the proton conducting polymer phases and gas-permeable open spaces connect and interpenetrate. Here, atomistic computer simulations on various time and length scales play an increasingly important role. In the following some results obtained in our group are briefly discussed.

2. Methanol Oxidation on Noble Metal Catalysts

While hydrogen oxidation in PEFCs is kinetically fast on platinum catalyst particles, the oxidation of methanol on Pt is to some extent performance limiting in the DMFC. At the very least, the low turnover rate mandates high noble metal loadings and concomitant high costs. This reaction, however, does not take place in vacuo but in an aqueous environment, near a perfluorinated sulfonic acid such as the commonly used membrane material Nafion® and furthermore depends on the electrode potential (and thus the surface charge).

As a first step towards modeling this situation, we have investigated the electrocatalytic oxidation of methanol at the interface between water and regular Pt(111) and Pt(211) surfaces [2,3] using quantum mechanical density functional theory and employing the VASP computer code. The charge on the platinum particle, modeled as a periodic slab consisting of 3 or 4 atomic layers, was varied systematically. In the absence of water methanol physisorbs to the uncharged platinum surface via interaction of the oxygen atom with the surface. A configuration in which a CH bond points towards the surface has a significantly higher energy. The presence of only one water molecule almost balances the energetic differences, thereby increasing the likelihood of activating a CH bond. Furthermore, the hydroxyl proton of methanol can be transferred into the aqueous phase, a process which is impossible in vacuum. Thus, on positively charged surfaces the presence of water does not only influence the reaction pathway as compared to the gas phase reaction, but rather actively changes the sequence of reactive events by directly, i.e., without intermediate adsorption, incorporating the hydroxyl hydrogen atom into the aqueous hydrogen bond network, as illustrated in Fig. 1.

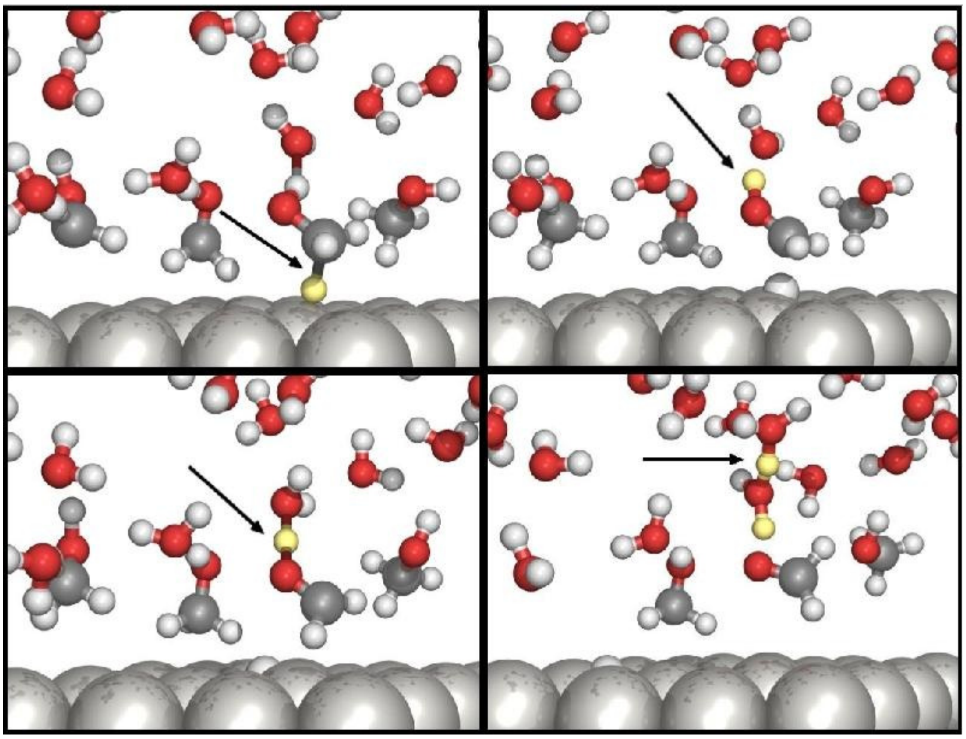

Figure 1: Chemical reaction dynamics of methanol oxidation to formaldehyde: One of the C-H bonds of the methyl group becomes elongated (top left) and eventually breaks (top right). The adsorbed hydroxy-methyl group stabilizes by forming a hydrogen bonded complex to a water molecule (bottom left) and dissociates rapidly into adsorbed formaldehyde and a hydronium ion (bottom right), which further stabilizes by undergoing structural diffusion steps to form Zundel ions. (Taken from Ref. [2].)

3. Proton Transport in Polymer Electrolyte Membranes

Polymer electrolyte membranes (PEMs) like Nafion are phase-separated on the nanometer scale into a polymer phase, which consists of a polytetrafluoroethylene backbone with pendant end-sulfonated side chains, and an aqueous phase. The continuous polymer phase provides structural stability and separates anodic and cathodic compartments of the fuel cell. Above a percolation threshold, when the embedded aqueous phase becomes continuous, the proton conductance of the membrane increases significantly with increasing water content λ, which is defined as the number of water molecules per sulfonic acid group of the polymer. The sulfonaic acid groups are strongly acidic and transfer the proton into the aqueous phase, which thus becomes a proton conductor. From the magnitude and the temperature dependence of fully humidified Nafion membranes it has been concluded that the proton transport mechanism follows the well-established bulk Grotthus or structural diffusion mechanism, according to which protons are continuously transferred from a hydronium ion to a neighbouring water molecule. At low water content ($\lambda \approx 3$-5) proton transport in the membrane is considered to be due to an interplay of the bulk Grotthus and a surface mechanism (transfer along an array of sulfonate groups). An empirical valence bond (EVB) model, which classically mimics the structural diffusion mechanism for molecular dynamics has been developed to study proton transport in Nafion [4,5,6,7].

Individual proton hops take place on the picosecond time scale. On the other hand, large scale polymer motions occur on much longer time scales. Thus, taking an extreme viewpoint, the polymer can be regarded as an immobile framework containing pores of simple slab or cylinder shape. Such a pore model is simple enough to allow the investigation of proton transport as a function of a variety of *generic* structural and dynamical features of the polymer (such as acid strength, head group and side chain mobility, and equivalent weight), and of *operational* parameters of the working fuel cell (such as temperature and water content). For this purpose a model with tethered sulfonate groups on a rigid slab surface was found to provide a reasonably realistic description. As an example, Fig. 2 shows the calculated dependence of proton conductance on water content for different equivalent weights of the polymer (expressed in terms of the surface charge density of sulfonate groups on the slab wall). It demonstrates how the single pore mobility leads qualitatively to the same water content dependent proton conductance as is experimentally observed for the entire membrane. The dependence on surface charge density (which correlates with polymer equivalent weight) also describes qualitatively some experimental trends of proton conductance in different polymers with varying equivalent weight.

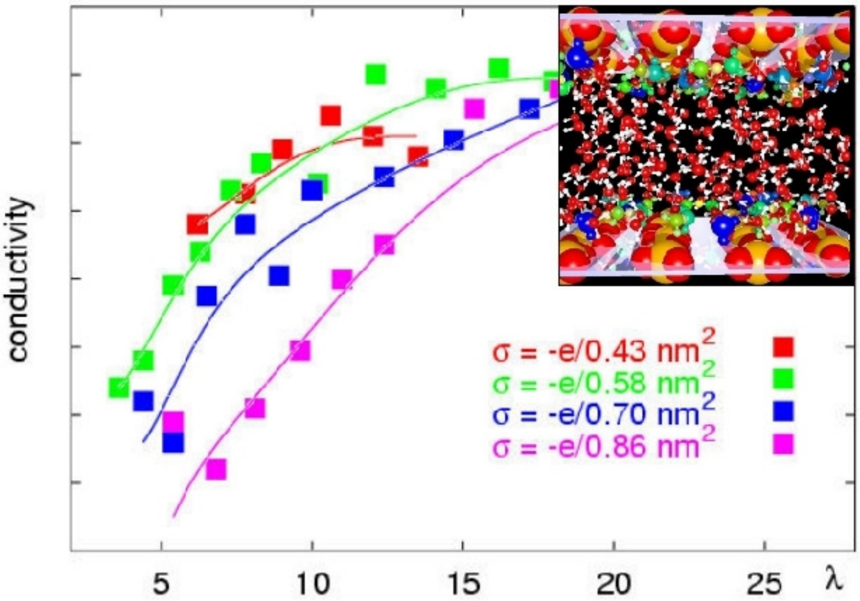

Figure 2: Dependence of proton conductivity (scaled units) on water content λ for several slab pores with different surface charge densities (spacings) of sulfonate groups. Note that the variance of instantaneous proton states (blue: hydronium-like, yellow-green: Zundel-like) in the snapshot is characteristic for the aqueous pores, and their easy interconversion is essential for proton mobility, thus warranting the use of complex molecular models.

On the basis of the temperature dependence of proton mobility in single pores it was concluded that the experimentally observed increase of activation energy for proton transport in dry membranes is most likely associated with the dynamics of the polymer at low water content. Local pore structure and dynamics was investigated using fully atomistic models of the Nafion polymer [8,9,10]. In Ref. [9] the aqueous phase was described by a simple classical force field which treats hydronium and water like rigid molecular ions or molecules interacting through standard force fields. As a representative result of these studies, Fig. 3

shows snapshots of aqueous domains at λ=5 at two different times which are consistent with the view of activated fluctuative bridging of disconnected aqeous pores, which leads to a small but finite proton conductance and an increased activation energy as compared to humidified membranes.

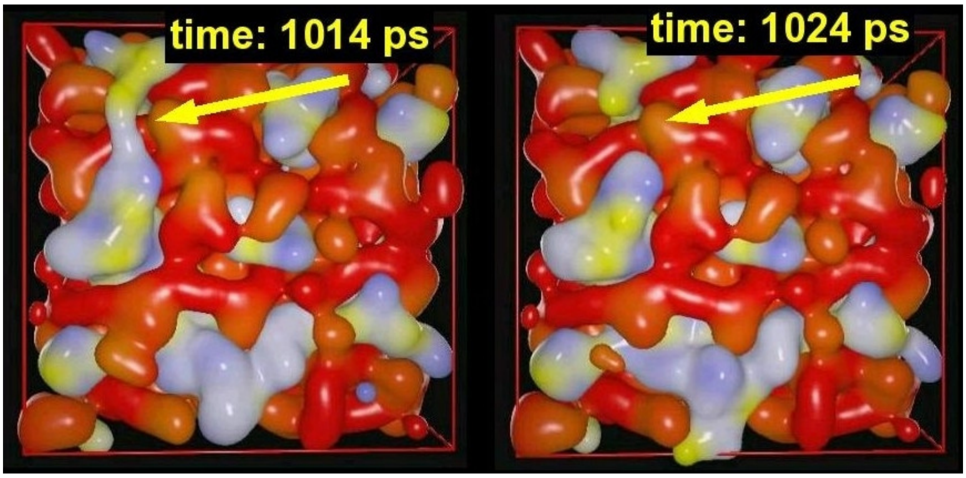

Figure 3: Snapshots at different times of a jelly-bean representation of a simulated mixture of water and Nafion in protonated form (at water content λ=5). Red regions denote polymer, grey, blue and yellow regions denote water, hydronium and sulfonate groups, respectively, in the aqueous phase. The indicated box corresponds to a length of 4.5 nm. Note that the jelly-bean surfaces hide a large number of molecules

With atomistic simulations on the united-atom level, where only the essential topological features of the Nafion base unit are retained, morphological transitions between inverse micellar aqueous pores at low water content to channel like structures at high water content are currently studied. Snapshots of these simulations are shown in Fig. 4. The scattering factor calculated from such simulations can be compared to small angle neutron and X-ray scattering experiments.

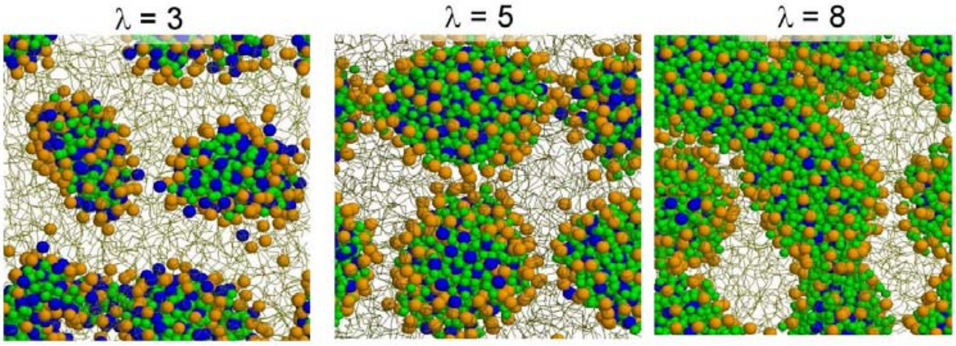

Figure 4: Snapshots of coarse-grained (fused-atom) simulations of water/Nafion mixtures with water content λ as indicated. Aqueous regions are shown as spheres. With increasing water content inverse micelles (λ=3) first merge (λ=5) and then form channels (λ=8).

4. Summary

Atomistic simulation methods have become an important tool to investigate the molecular dynamics in the complex multiphase fuel cell environment on a variety of time and length scales. Further development is needed for a true multiscale modeling approach to this topic. In particular, connecting the atomistic level with successful phenomenological and continuum models of fuel cells [11] will provide a challenge in the near future.

References

[1] K.-D. Kreuer, S. J. Paddison, E. Spohr and M. Schuster, *Transport in Proton Conductors for Fuel-Cell Applications: Simulations, Elementary Reactions, and Phenomenology*, Chem. Rev. **104**, 4637-4678 (2004).
[2] C. Hartnig and E. Spohr, *The role of water in the initial steps of methanol oxidation on Pt(111),* Chem. Phys. **319**, 185-191 (2005).
[3] C. Hartnig, J. Grimminger and E. Spohr, *The role of water in the initial steps of methanol oxidation on Pt(211), Electrochim. Acta.*, in press (2006).
[4] S. Walbran and A. A. Kornyshev, *Proton Transport in Polarizable Water*, J. Chem. Phys. **114**, 10039-10048 (2001).
[5] E. Spohr, P. Commer and A. A. Kornyshev, *Enhancing Proton Mobility in Polymer Electrolyte Membranes: Lessons from Molecular Dynamics Simulations,* J. Phys. Chem. B **106**, 10560-10569 (2002).
[6] P. Commer, A. G. Cherstvy, E. Spohr and A. A. Kornyshev, *The Effect of water content on proton transport in polymer electrolyte membranes*, Fuel Cells **2**, 127-136 (2002).
[7] P. Commer, C. Hartnig, D. Seeliger and E. Spohr, *Modeling of Proton Transfer in Polymer Electrolyte Membranes on Different Time and Length Scales,* Mol. Simulation **30**, 775-763 (2004).
[8] S. J. Jang and V. Molinero and T. Cagin and W. A. Goddard III, *Nanophase-Segregation and Transport in Nafion 117 from Molecular Dynamics Simulations: Effect of Monomeric Sequence,* J. Phys. Chem. B **108**, 3149-3157 (2004).
[9] D Seeliger, C. Hartnig and E. Spohr, *Aqueous Pore Struture and Proton Dynamics in Solvated Nafion Membranes,* Electrochim. Acta **50**, 4234-4240 (2005).
[10] N. P. Blake, M. K. Petersen, G. A. Voth and H. Metiu, *Structure of Hydrated Na-Nafion Polymer Membranes,* J. Phys. Chem. B **109**, 24244-24253 (2005).
[11] M. Eikerling, A. A. Kulikovsky and A. Kornyshev, *Can Theory Help to Improve Fuel Cells?*, The Fuel Cell Review, December 2004/January 2005, 15-24.

Grain boundaries in silicon - a new look at an old problem

Adrian Sutton [1], *G. Pruessner* [1], *P. D. Haynes* [2], *K. K. Kaski* [3], *S. von Alfthan* [3]

[1]*Imperial College London, Department of Physics, Exhibition Road, SW7 2AZ, London, United Kingdom*
[2]*Cavendish Laboratory, Madingley Road, CB3 0HE, Cambridge, United Kingdom*
[3]*Laboratory of Computational Engineering, Helsinki University of Technology, 02150, Finland*

In the late 80s and through the 90s there were repeated claims that high- angle twist boundaries in silicon in their ground states at absolute zero show varying degrees of disorder. In some notable cases claims were made that the ground state boundary structures resemble films of amorphous silicon. We have re-examined some high-angle twist boundaries in Si using molecular dynamics simulations. There are 2 aspects to our simulation methods that are new. The first is that we consider boundary configurations that have not been simulated before in Si, namely those obtained by removing atoms from the boundary plane. Secondly we allow much longer simulated anneals, by up to two orders of magnitude. These two differences have enabled us to find new low energy ordered configurations of the boundaries at absolute zero [1]. Our findings are more consistent with experimental observations than earlier simulations. We have also carried out simulations in which these low energy structures are annealed to the melting point. We see that the boundaries remain ordered with well-defined excitations that may be described in terms of structural units until about 0.8 TM. At higher temperatures the boundary becomes increasingly wider and disordered. We discuss our work in the context of the recently published phase-field modelling of grain boundaries in single-component systems as a function of temperature [2].

* Supported by the EU under grant CEC NMP3-CT-2005-013862, „INCEMS“.

1. „Are the structures of twist grain boundaries in silicon ordered at 0K?“, S von Alfthan, P D Haynes, K Kaski and A P Sutton, Phys. Rev. Letts. 96, 055505 (2006).
2. „Diffuse interface model for structural transitions of grain boundaries“, M Tang, W C Carter and R M Cannon, Phys. Rev. B 73, 024102 (2006).

Analytical Effective Coefficient for Flow Equations in Porous Media by homogenization theory

Rosangela F. Sviercoski[*] and Bryan J. Travis[†]
Los Alamos National Laboratory MS D401,
Los Alamos, NM 87545, USA

Abstract

In this paper, we present an analytical form for the effective coefficient to linear flow equations defined in $\Omega \in R^n$, with smooth boundary. The approach comes from classical homogenization theory applied to heterogeneous coefficients that are periodic and rapidly oscillating and belong to $L^p(\Omega), 1 \leq p \leq \infty$. The result comes from assuming an approximation for the analytical solution of the periodic cell problem, obtained by the two-scale asymptotic expansion of the respective heterogeneous equations. The numerical results are applied to heterogeneous coefficients, defined as step functions describing inclusions of square shapes, such that the ratio between the inclusion and the matrix are 10:1, 100:1 and 1000:1. We demonstrate, numerically, the strong convergence in L^2-norm of the approximations by applying the results to specific problems of interest for flow in porous media.

1 Introduction

A major problem in porous media is to perform an accurate description of flow behavior, in spite of the intrinsic heterogeneity of materials or geological formations. The effective or equivalent property, derived from homogenization, represents the heterogeneous medium in a simplified description. The homogenization approaches are without doubt the most robust, but to use them, one has to develop a code for numerically solving the cell-problem of the auxiliary variable [3]. Because of a such constraint, obtaining a homogenized coefficient becomes computationally expensive.

To make precise the fact that the medium varies rapidly on the small scale l and may also vary slowly on the large scale L, we assume that the solution of a multiscale problem has the form $u\left(x,y\right) = u^{\varepsilon}(x) = u^0\left(x,y\right) + \varepsilon u^1\left(x,y\right)$ with $y = \frac{x}{\varepsilon}$, where $\varepsilon = \frac{l}{L}$. Consider $K^{\varepsilon}(x) = K(y) \in L^p(\Omega)$. In here, the homogenization procedure consists in making the substitution of $u^{\varepsilon}(x)$ into the boundary value problem (BVP):

$$\begin{cases} \nabla \cdot \left(K^{\varepsilon}\left(x\right)\nabla u^{\varepsilon}\left(x\right)\right) + f\left(x\right) = 0 & x \in \Omega \\ u\left(x\right) = g(x) & x \in \partial\Omega \end{cases} \tag{1}$$

---

[*] *email: rsvier@lanl.gov*

[†] *email: bjtravis@lanl.gov*

and determining what equation $u^0(x,y)$ satisfies, where $u^0(x,y) = \lim_{\varepsilon\to 0} u^\varepsilon(x)$. See [1], [2], and [4], among others. Then one has the following result:

> **H-Convergence** A constant matrix K^0 is the homogenized limit of K^ε, if and only if, for any bounded domain $\Omega \subset R^n$ and for any $f \in H^{-1}(\Omega)$ the solutions $u^\varepsilon \in H^1(\Omega)$ of (1) possess the properties, as $\varepsilon \to 0$,:
>
> $$\begin{gathered} u^\varepsilon \rightharpoonup u^0 \quad \text{in} \quad H^1(\Omega) \\ K^\varepsilon(x)\nabla u^\varepsilon(x) \rightharpoonup K^0 \nabla u^0(x) \quad \text{in} \quad H^1(\Omega) \end{gathered} \tag{2}$$
>
> where $u^0 \in H^1(\Omega)$ is the solution of: $\nabla \cdot (K^0 \nabla u^0(x)) + f(x) = 0$

Using the *Kronecker delta* $\delta_{i,j}$, the homogenized coefficient K^0 is defined as

$$K^0_{ij} = \int_Y K(y)\left(\delta_{i,j} + \partial_{y_i} w_i(y)\right) dy \tag{3}$$

where $w_i(y)$ is the solution of the periodic problem in $Y = [0,1]^n$:

$$\nabla \cdot (K(y)\nabla_y w_i(y)) = -\nabla \cdot (K(y) e_i) \qquad \text{for } y \in Y \tag{4}$$

where e_i is the unit vector. By having a solution for (4) one can compute the effective coefficient in (3) and the homogenized approximation $u^0(x)$ in (2).

The goal here is to present an analytical procedure for obtaining (3) and demonstrate numerically the convergence properties in $L^2(\Omega)$. The results are achieved by assuming an analytical approximation for (4) and applying a corrector to it.

It is known that in the 1-D case, the harmonic average is the effective coefficient. For the n-dimensional case, when $K(y)$ is a separable function, i.e., $K(y) = \Pi_{i=1}^n k_i(y_i)$, K^0 is given as the arithmetic average of the harmonic average in each direction [2].

Many numerical approaches in the literature have been proposed in order to obtain numerical values for (3), when the heterogeneous coefficient, $K(y) \in L^p(Y)$ is of the form:

$$K(y) = \begin{cases} \zeta_1 & x \in Y_1 \\ \zeta_2 & x \in Y \backslash Y_1 \end{cases} \tag{5}$$

where $Y = [0,1]^2$ and $Y_1 \subset\subset Y$ are inclusions of shapes like squares, circle and lozenge. See tables on [5] and [6] and citations herein.

2 Analytical Approximation for K^0

To obtain the analytical approximation, we assume the solution of (4), be given as:

$$w_i(y) = \int_0^{y_i} \frac{d\tau}{K(y_1,..,\tau,..,y_n)} \left(\int_0^1 \frac{d\tau}{K(y_1,..,\tau,..,y_n)}\right)^{-1} - y_i \tag{6}$$

by letting $\int_Y K(y)\frac{\partial w_j}{\partial y_i} dy = 0$ for $i \neq j$ and setting $R_i = \left(\int_0^1 \frac{d\tau}{K(y_1,..,\tau,..,y_n)}\right)^{-1}$, it leads to K^0_a, which agrees with the separable case, i.e.,

$$K^0_a = diag\left(\int_Y R_1 dY, ..., \int_Y R_i dY, .. \int_Y R_n dY\right) \tag{7}$$

It has been shown in [5] and [6] that, by using (7) as the analytical form for K^0, leads to values within 10% agreement with numerical results for $K(y)$ as in (5). Therefore a corrector can be applied to (7) to obtain the H-convergence.

Table 1: Summary for the ratio 10:1 on $[0,2]^2$ domain

ε	ER	rate	EGRAD	EFLUX	mesh (nodes)
$(0.5)^1$	4.62e-2	n/a	1.28e-1	5.13e-1	8321
$(0.5)^2$	2.11e-2	4.56e-1	1.16e-1	4.23e-1	16641
$(0.5)^3$	9.78e-3	4.64e-1	1.12e-1	3.57e-1	16095
$(0.5)^4$	4.92e-3	5.03e-1	1.10e-1	3.28e-1	32018
$(0.5)^5$	2.39e-3	4.70e-1	1.03e-1	3.10e-1	32558
$(0.5)^6$	9.5e-4	3.96e-1	9.64e-2	3.10e-1	64932

2.1 Defining the Corrector

To obtain the corrector, and therefore K^0, we look for the matrix $C^\varepsilon = (C^\varepsilon_{ij})$, with $1 \le i, j \le n$, defined by:

$$C_{ij}(y) = \delta_{ij} + \frac{\partial w_j}{\partial y_i} \qquad a.e. \text{ on } \quad Y \tag{8}$$

with $w_i(y)$ as in (6) and assuming that for $i \neq j$, $\frac{\partial w_j}{\partial y_i} = 0$ a.e. in Y. Moreover, one has the following properties:

Theorem 1 Let $C^\varepsilon(x)$ as in (8) and I the identity matrix in R^n. Then

$$(i) \;\; C^\varepsilon \rightharpoonup I \quad \text{in } (L^2(\Omega))^{n\times n} \text{ and } (ii) \;\; C^\varepsilon K^\varepsilon \rightharpoonup K^0_a \quad \text{in } (L^2(\Omega))^{n\times n} \tag{9}$$

Proof: By substitution of $w_i(y)$ from (6) and K^0_a in (7).

Corrector We define K^0, the corrector of K^0_a as

$$K^0 = ||C^\varepsilon||_2 \, K^0_a = C K^0_a \tag{10}$$

Mathematically it just means that the approximated solution of the cell problem has being "corrected" by a multiplicative constant C.

3 Numerical Results

We illustrate the convergence for the coefficient functions defined in (5) where the ratio 10:1 is meant that $\zeta_1 = 10$ and $\zeta_2 = 1$, likewise for the ratios 100:1 and 1000:1. In the definition Y_1 represents square inclusion occupying 1/4 of the area of an unit cell. In the Tab. 1, 2 and 3, we approximate $u^\varepsilon(x)$ by $u^0(x)$, where they are the respective solutions for the equation (1), with $f(x) = -1$ and $g(x) = 0$ over $\partial\Omega$.The heterogeneous coefficient, $K^\varepsilon(x)$, is such that ε take values on the sequence $s = (0.5)^n$, for $n = 1, 2, 3, 4, 5, 6$ meaning that Y_1 in (5) describes $1, 4, 16, 64, 256, 1024$ square inclusions in $[0,1]^2$, respectively. When the ratios are 10:1, 100:1 and 1000:1, (7) gives $K^0_a = 1.4091$, $K^0_a = 1.4901$ and $K^0_a = 1.5$. By using (10) we have: $K^0 = 1.1188 \times 1.4091 = 1.5765$, $K^0 = 1.2345 \times 1.4901 = 1.8395$ and $K^0 = 1.2519 \times 1.5 = 1.8779$, respectively. In what follows, $ER = ||u^\varepsilon(x) - u^0(x)||_2$, $ECH = ||C\nabla u^\varepsilon(x) - \nabla u^0(x)||_2$, and $EFLUX = ||K^\varepsilon(x)\nabla u^\varepsilon(x) - K^0\nabla u^0(x)||_2$.

Table 2: Summary for the ratio 100:1 on $[0,1]^2$ domain

ε	ER	rate	EGRAD	EFLUX	mesh (nodes)
$(0.5)^1$	1.44e-2	n/a	8.78e-2	2.41e0	289
$(0.5)^2$	6.65e-3	4.61e-1	8.14e-2	1.88e0	545
$(0.5)^3$	3.10e-3	4.65e-1	7.79e-2	1.62e0	1064
$(0.5)^4$	1.56e-3	5.05e-1	7.68e-2	1.55e0	2139
$(0.5)^5$	5.84e-3	3.73e-1	7.58e-2	1.35e0	4194

Table 3: Summary for the ratio 1000:1 on $[0,1]^2$ domain

ε	ER	rate	EGRAD	EFLUX	mesh(nodes)
$(0.5)^1$	1.48e-2	n/a	8.44e-2	2.22e+1	145
$(0.5)^2$	6.70e-3	4.53e-1	7.13e-2	1.68e+1	289
$(0.5)^3$	3.17e-3	4.73e-1	6.58e-2	1.42e+1	766
$(0.5)^4$	1.43e-3	4.50e-1	5.51e-2	1.12e+1	1361
$(0.5)^5$	7.92e-4	5.55e-1	5.48e-2	1.12e+1	5409

References

[1] Bensoussan, A., Lions, J.L., Papanicolau, G. *Asymptotic Analysis for Periodic Structures*, Noth-Holland (1978).

[2] Jikov, V. V., Kozlov, S.M., Oleinik, O.A. *Homogenization of Differential Operators and Integral Functionals*. Springer Verlag (1994).

[3] Renard, Ph. and De Marsily, G. *Calculating Equivalent Permeability: a Review.* Adv. Water Resources, Vol. 20, nos 5-6, pp. 253-278 (1997).

[4] Cioranescu, D., Donato P. *An Introduction to Homogenization*, Oxford Lecture Series in Mathematics and its Application, Vol. 17 (1999).

[5] Sviercoski, R. F. *Multiscale Analytical Solutions and Homogenization of n-Dimensional Generalized Elliptic Equations*, Ph.D. Dissertation, University of Arizona, (2005).

[6] Sviercoski, R. F., Warrick, A.W., Winter, C. L., (2005) *Multiscale Analytical Solutions and Homogenization of n-Dimensional Generalized Elliptic Equations* . in: Numerical Upscaling: Theory and Applications. pp. 37-39. MFO Report 20/2005.

A Quasicontinuum for Complex Crystals

M. Dobson[1], R. S. Elliott[2] and E. B. Tadmor[2,3]

[1] School of Mathematics, University of Minnesota, Minneapolis, MN 55455, USA

[2] Aerospace Engineering and Mechanics, University of Minnesota, Minneapolis, MN 55455, USA

[3]Department of Mechanical Engineering, Technion – Israel Institute of Technology, 32000 Haifa, Israel

July 15, 2006

ABSTRACT

The quasicontinuum (QC) method is extended to materials possessing complex crystal structures. This requires a generalization of the Cauchy-Born (CB) kinematics, which is used in the continuum region to relate atomic motions to continuum deformation gradients, to account for the shuffles of the crystal sub-lattices. In addition, in order to prevent failures of the CB kinematics, it is augmented with a phonon stability analysis that detects lattice period extensions and identifies the minimum required cell size. This augmented approach is referred to as *cascading Cauchy-Born kinematics*. To prevent the formation of degenerate symmetry-related structures and to introduce a physical lengthscale into the continuum, an estimate for the interfacial energy is added to the total energy. The method is demonstrated for a number of one-dimensional test problems.

1 Introduction

The quasicontinuum (QC) method [1, 2, 3] is a multiscale method coupling an atomistic region with a surrounding continuum modeled within a nonlinear finite element formulation. The constitutive response in the continuum is obtained by the application of Cauchy-Born (CB) kinematics to the underlying lattice and calculation of the energy and necessary gradients using the same inter-atomic potentials applied in the atomistic region. This together with built-in automatic mesh refinement lend to QC a seamlessness and adaptivity that facilitates the simulation of complex boundary-value problems (BVPs).

In the application of QC to multifunctional materials, such as ferroelectrics or shape-memory alloys, it must be recognized that these materials have complex crystal structures. This means that CB kinematics, which for simple lattices simply states that the atoms are mapped according to the continuum field, must be extended to account for the shuffling of the sub-lattices making up the crystal [4]. This is straightforward to do, however a question arises as to which description of the crystal structure should be used. Traditionally, CB kinematics has been interpreted as being applied to the essential description of the lattice, i.e., the simplest periodic structure that reproduces the crystal. However as pointed out by Zanzotto [5, 6], with

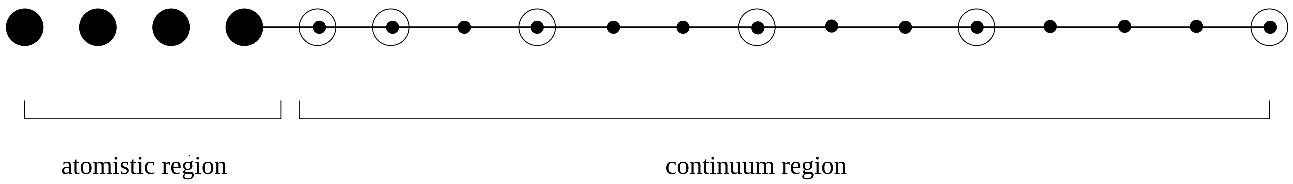

Figure 1: A 1D QC. The black circles are atoms, the white circles are nodes and the dots denote the underlying lattice. The lines represent the elements defined in the continuum region.

this definition CB kinematics can fail since some deformations require an increase in the periodic size of the unit cell. The problem is that the appropriate cell-size for a particular BVP cannot be known *a priori*. Detection of such period extensions can be critical in many cases where phase transformations occur in the material. Additionally, in these situations degenerate random structures, such as anti-phase boundaries (APBs) can occur, due to the existence of energetically equivalent variants of the new material phase.

These issues are addressed within a new implementation of QC in two ways. (1) A phonon stability analysis, along the lines proposed by Elliott et al. [7, 8] is performed locally within each finite element in the continuum region at the end of each load step. This analysis detects the onset of period extension and identifies a new physically appropriate lattice description. (2) A physical lengthscale is introduced into the continuum via the addition of an interfacial energy between elements.

As a result of these additions to the QC formulation, careful attention needs to be paid to coupling between the atomistic and finite-element regions and to the definition of a criterion for mesh refinement. These issues, as well as their straightforward extension to higher dimensions, are currently being pursued.

In the remainder of this report a more detailed discussion of these issues and our techniques for addressing them are presented. In Section 2, a brief review of QC for simple and multilattices is presented. Section 3 introduces the "Cascading Cauchy-Born" kinematics technique and presents a simple one-dimensional material model that clearly illustrates its necessity. The issue of degenerate structure formation, including APBs, is addressed in Section 4. An atomistically informed inter-element interface energy is developed that couples the element multilattice shifts to provide an energy penalty to the formation of degenerate structures. Finally, in Section 5, a brief discussion of related issues left to future work is presented.

2 1D Quasicontinuum method

In this section we present a brief overview of the QC methodology. The reader is referred to [2, 3] for more details. Since this paper deals a with a one-dimensional (1D) implementation of QC, we limit the discussion to that simplified special case.

2.1 Simple lattices

In QC, a simulation domain containing N atoms is divided into atomistic and continuum regions. In the atomistic region, all atoms are retained for a total of n_a atoms. In the continuum region only a small number, n_n, of nodes are retained (Fig. 1). These nodes serve as the vertices in a finite element mesh containing m elements. In order to facilitate mesh refinement and motion of the continuum/atomistic interface, the nodes in the continuum region are constrained to occupy lattice sites in the reference configuration:

$$X(m) = ma, \tag{1}$$

where a is the lattice parameter in the reference configuration and m is an integer index.

The total number of points in the QC model is $n = n_a + n_c$, where normally $n \ll N$. These points have positions X^i ($= m^i a$) in the reference configuration. They move in response to the applied loading to new positions:[1]

$$x^i = X^i + u^i, \tag{2}$$

where u^i are point displacements. Equilibrium configurations are obtained by minimizing the total QC potential energy,

$$\Pi = \sum_{i=1}^{n_a} E^i(u) + \Omega \sum_{e=1}^{m} \nu^e W(F^e) - \sum_{j=1}^{n} \left(f^j_{\text{ext}} + f^j_{\text{ghost}} \right) u^j, \tag{3}$$

with respect to the set of point displacements, $u = \{u^1 \ldots u^n\}$, subject to prescribed boundary conditions.

The first term in (3) is the energy of the atomistic region taken as a sum over individual atom energies E^i. For example, for a pair potential model $\phi(r)$ of inter-atomic interactions the atomic energy is:

$$E^i = \sum_{j \neq i}^{n_a} \phi(r^{ij}), \tag{4}$$

where $r^{ij} = |x^j - x^i|$ is the distance between atoms i and j and as usual a cutoff for inter-atomic interactions is applied.

The second term in (3) is the energy of the continuum region taken as a sum over the strain energy of the elements. Here W is the strain-energy density (SED) that is a function of the deformation gradient F in the element:

$$F = 1 + \Delta u / h, \tag{5}$$

where Δu is the change of displacement across the element and h is its length. In addition, ν^e is the number of atoms in element e represented by continuum nodes[2] and Ω is the unit cell volume in the reference configuration. In QC, $W(F)$ is computed using the same inter-atomic potential applied in the atomistic region by assuming CB kinematics to relate atomic motion in the lattice underlying the continuum to F:

$$x(m) = FX(m) = Fma. \tag{6}$$

---

[1] We adopt the standard continuum mechanics convention of using capital letters for measures in the reference configuration and small-case letters for the deformed configuration.

[2] For elements whose vertices are all nodes, $\nu = h/a$. However, for elements at the continuum/atomistic interface ν will only contain a fraction of the atoms in the element (see [2] for details).

The resulting SED function for a pair potential is:

$$W(F) = \frac{1}{a} \sum_m \phi(Fma). \tag{7}$$

The third term in (3) is the potential of the external loads f^i_{ext} along with the ghost-force correction terms f^i_{ghost} [2] that cancel out the atomistic-continuum mismatch error at the interface.

2.2 Multilattices

For multi-lattices, the lattice positions represent the location of the unit cell, and the atomic positions are given in terms of additional shifts Δ_α relative to these positions:

$$X(m,\alpha) = ma + \Delta_\alpha, \qquad \alpha \in \{1...N_B\}, \tag{8}$$

where N_B is the basis size. Cauchy-Born kinematics for multilattices states that

$$x(m,\alpha) = FX(m,\alpha) + \delta_\alpha. \tag{9}$$

All the sublattices deform as a simple lattice, but they are free to displace relative to one another under the deformation. As a result, the SED function will depend on element shifts as well as the deformation gradient, $W = W(F,\delta)$, where $\delta = \{\delta_1, \ldots, \delta_{N_B}\}$. The dependence on δ can be minimized locally by requiring,

$$\tilde{W}(F) = W(F, \delta(F)), \tag{10}$$

$$\text{s.t.} \left. \frac{\partial W}{\partial \delta_\alpha} \right|_F = 0. \tag{11}$$

Alternatively, the shifts can be relegated along with the point displacements as global degrees of freedom. This is mandatory when interfacial energy corrections, as explained in section 4, are included.

As noted above, the description of the multilattice is non-unique. In addition to freedom in the choice of lattice vectors (for the multi-dimensional case), there is a choice of the basis size. A basis larger than the essential one allows for descriptions of more complicated deformations, including many phase transformations.

3 Cascading Cauchy-Born (CCB) kinematics for multilattices

When using Cauchy-Born kinematics one inevitably must make a decision about the crystal structure basis that will be used. Most often an essential basis is chosen because of its special properties, as discussed above. In some cases though, such as when translation-symmetry breaking phase transformations occur, it is important to use a non-essential basis (as in [8]). Usually in these cases, an arbitrary fixed choice of basis is made at the outset, and often an investigation or discussion of the consequences of this choice is not presented.

In general, the appropriate basis is *a priori* unknown and, in fact, it usually depends on the applied boundary conditions and the evolving deformation of the crystal. Therefore, in this work a new strategy is employed, based on the procedure outlined in [8], that treats the basis as an evolving entity that responds to the physical environment to which the crystal is subjected. This strategy, which we call the "Cascading Cauchy-Born" kinematics, starts with an essential basis for the crystal and monitors the phonon stability (see [7]) of the crystal structure as its deformation evolves in response to applied loads. Once an instability is identified, the critical phonon-mode wave-vector is used to systematically identify the appropriate new basis with which to describe the crystal. Initially, this basis will be a non-essential basis for the crystal, but in light of the identified instability, a subsequent energy minimization procedure will result in a crystalline configuration for which the new basis is an essential basis—a configuration that is not obtainable with the original basis.

3.1 A period doubling example

As an example of a physical system where CCB kinematics are required, consider a one-dimensional biatomic crystal with long-range Lennard-Jones (LJ) pair interactions. There are three LJ potentials needed to describe the atomic interactions: (1) interaction between two 'a' atoms $\phi_{aa}(r)$, (2) interactions between two 'b' atoms $\phi_{bb}(r)$, and (3) interactions between an 'a' atom and a 'b' atom. The LJ pair-potential is given by[3]

$$\phi(r) = 4\epsilon\left[\left(\frac{\sigma}{r}\right)^{12} - \left(\frac{\sigma}{r}\right)^{6}\right], \tag{12}$$

and the interaction parameters are: $\epsilon_{aa} = 1.0, \sigma_{aa} = 1.0$, $\epsilon_{bb} = 0.1, \sigma_{bb} = 0.85$, and $\epsilon_{ab} = 0.1, \sigma_{ab} = 0.48$.

The stress-free reference configuration for the crystal can be described by an essential basis that contains two atoms, one of each type. Each atom is symmetrically positioned between its nearest neighbors (which are of opposite species). To get an idea of how this material model behaves, a bifurcation diagram is generated following the technique in Elliott et al. [8]. Figure 2 displays the resulting stress-strain behavior. The applied stress σ is normalized by the reference Young's modulus E. The solid red line segment in Fig. 2 is the primary equilibrium path that the crystal follows upon initial tensile loading. This path corresponds to a 2-lattice crystal (with essential basis consisting of two atoms) and is stable until a bifurcation point is encountered near $\epsilon = 0.057$. The bifurcation is a translation-symmetry breaking bifurcation and the emerging (blue) equilibrium path has a 4-lattice structure (i.e., an essential basis that contains four atoms, two of each type). For strains between $\epsilon = 0.057$ and $\epsilon = 0.094$ this 4-lattice configuration is the only stable structure, and no stable structures exist for higher strains, indicating that the crystal fractures at a strain of $\epsilon = 0.094$. Other equilibrium paths (yellow, cyan, green, and purple) exist in Fig. 2, but they are always unstable.

Thus, the crystal's behavior may correctly be described with a 2-lattice CB kinematics up to the bifurcation point at $\epsilon = 0.057$, at which point the CCB technique will detect the instability, identify the 4-lattice kinematics as the new physically relevant description, and switch to the appropriate 4-lattice CB kinematics. In this way the period-doubling phase transformation in

---

[3] Here, subscripts indicating the type of species interaction, eg. aa, bb, or ab, are suppressed.

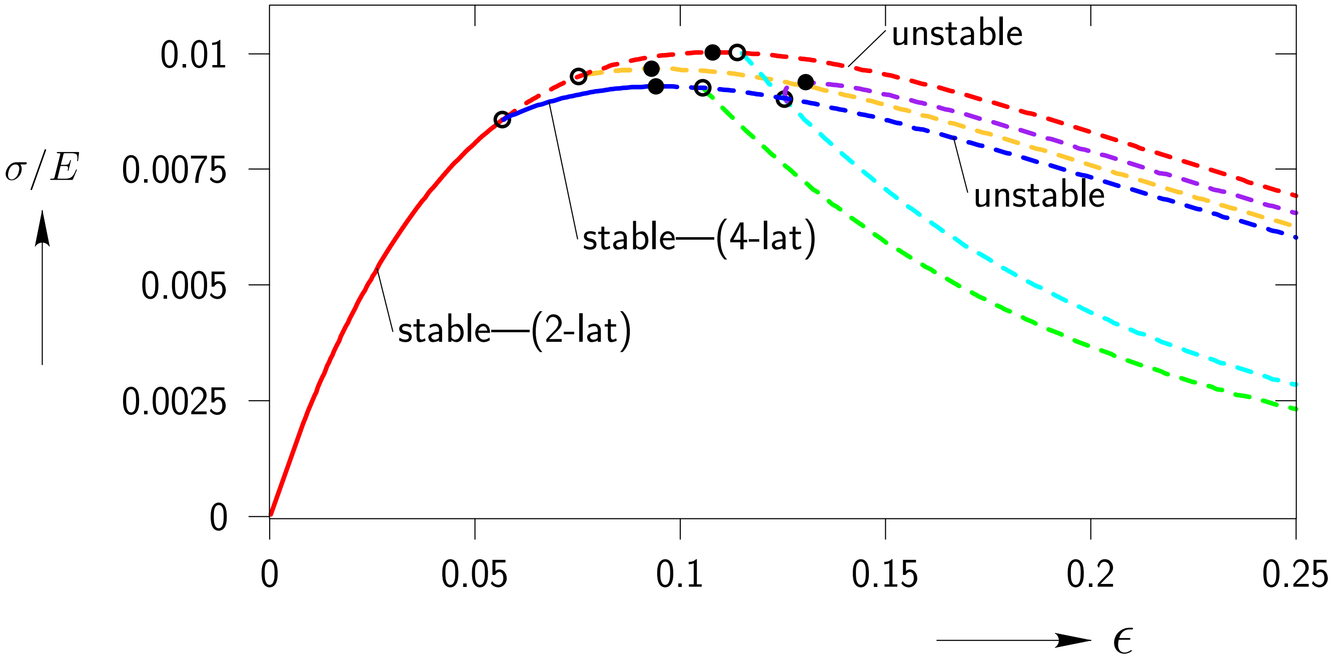

Figure 2: Normalized stress vs. strain behavior for the bi-atomic one-dimensional crystal, showing two stable path segments corresponding to a 2-lattice configuration (red) and a 4-lattice configuration (blue).

this material model is correctly captured—a behavior that a fixed CB kinematics technique would utterly miss.

The CCB technique is implemented within QC by performing the phonon stability calculation at the end of each QC energy minimization step. If an instability is identified, and therefore a new multilattice basis adopted by CCB, then a second QC energy minimization step will be performed under the same loading conditions. Thus, it is assured that at the end of each load step a true local potential energy minimum has been obtained.

4 Interfacial energy

Often when phase transformations occur the associated multilattice shifts are degenerate in the sense that the direction of deviation from their previous (parent phase) configuration is ambiguous from an energy standpoint. For QC, this is a problem since the multilattice shifts for each element are completely uncoupled. To eliminate this degeneracy the element shifts are coupled through the use of an inter-element interfacial energy penalty term.

Here, the interfacial energy is derived from the explicit underlying atomic configuration associated with each element in the problem.

Consider the QC finite-element region shown in Fig. 3, showing an inter-phase boundary between elements 1 and 2. In this illustrative example, the elements use a two-atom basis CB kinematics with lattice spacings F^1a, F^2a and shifts δ_1^1, δ_1^2 respectively. The interface between these elements is constructed (as shown) by placing all atoms on the left-hand side of the

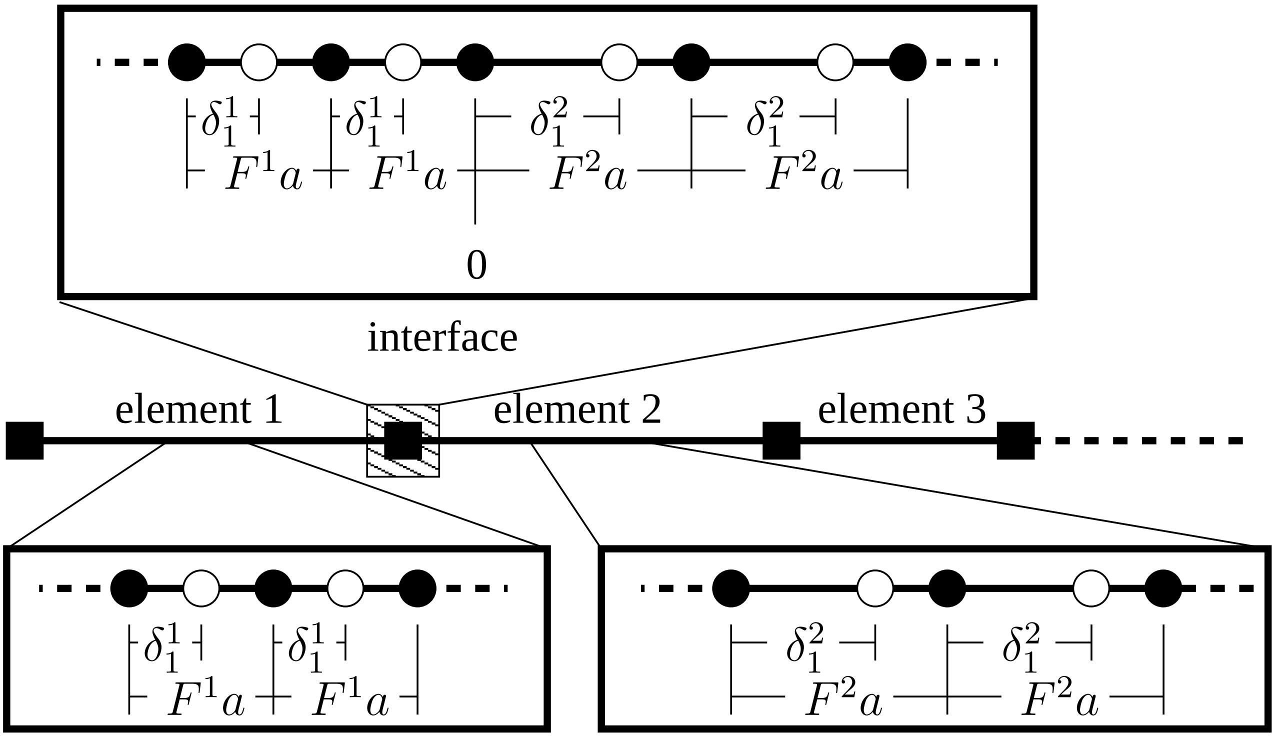

Figure 3: Interface between two elements. The extra atoms are in gray.

interface according to the periodic structure represented by element 1 and placing all atoms on the right-hand side of the interface according to the periodic structure represented by element 2. Using this configuration, the total energy of the interface (i.e., the energy of all atoms on either side of the interface that are located within the cutoff radius of the atomic potentials) is calculated and the bulk energy of each involved atom is subtracted[4] to obtain the interfacial energy. This provides a consistent definition of the interfacial energy that is a function of the lattice spacings and shifts associated with elements 1 and 2.

With the introduction of the interfacial energy, a physical lengthscale is introduced into the QC continuum region. As a result, this new QC implementation will be able to study physical phenomena such as APBs, twinning, and needle-like martensite microstructure formation; all of which have an associated characteristic lengthscale that is governed by the interplay between interfacial and elastic energy contributions.

5 Future Work

The new complex crystal QC formulation described above is in its initial stages of development and a number of issues remain that must be addressed. For instance, further work is needed to determine how to handle interfacial energy at the atomistic to continuum interface, as well

---

[4] Special care must be given to the atom located directly on the interface. When determining the bulk energy of this atom, it is important to treat half of the atom as belonging to element 1 and half as belonging to element 2. If this is not done, the interfacial energy will not be symmetric with respect to elements 1 and 2.

as dealing with special boundary conditions associated with the multilattice shifts for elements on the computational boundary. Additionally, the interplay between the CCB technique and the effects of interfacial energy deserves careful scrutiny to ensure a robust and stable energy minimization technique results.

Another complication is encountered when implementing adaptivity in light of the CCB multilattice formulation. In standard QC for simple lattices, in order to change from continuum to atomistic treatments, the finite element formulation ensures that all nodes for continuum elements are located on atomic sites. Therefore, as refinement progresses a meshing of all atoms represented is eventually obtained, and fully-refined regions can easily change from continuum to atomistic simply by changing the nature of the calculations. The current QC formulation needs a way to ensure that increasing the basis according to the CCB technique interacts appropriately with adaption. In particular, period increase should be prevented if it would cause the new multilattice basis to contain more atoms than is appropriate for the size of the element. In this case, the identification of an instability should cause the atomistic structure contained within the element to be fully refined and converted to an atomistic region.

All of these issues (and more) are actively being investigated with an eye toward applications to phase transforming materials, such as quartz and shape memory alloys, undergoing fracture and other failure events.

References

[1] E. B. Tadmor, M. Ortiz and R. Phillips, "Quasicontinuum Analysis of Defects in Solids", *Phil. Mag. A*, **73**, 1529-1563 (1996).

[2] V. B. Shenoy, R. Miller, E. B. Tadmor, D. Rodney, R. Phillips and M. Ortiz, "An Adaptive Finite Element Approach to Atomic-Scale Mechanics : The Quasicontinuum Method", *J. Mech. Phys. Solids*, **47**, 611-642 (1999).

[3] R. E. Miller and E. B. Tadmor, "The Quasicontinuum Method: Overview, Applications and Current Directions", *J. Computer-Aided Materials Design*, **9**, 203-239 (2002).

[4] E. B. Tadmor, G. S. Smith, N. Bernstein and E. Kaxiras, "Mixed Finite Element and Atomistic Formulation for Complex Crystals", *Phys. Rev B*, **59**, 235-245 (1999).

[5] G. Zanzotto, "On the Material Symmetry Group of Elastic Crystals and the Born Rule", *Arch. Rational Mech. Anal.*, **121**, 1-36 (1992).

[6] G. Zanzotto, "The Cauchy-Born Hypothesis, Nonlinear Elasticity and Mechanical Twinning in Crystals", *Acta Cryst.*, **A52**, 839-849 (1996).

[7] R. S. Elliott, N. Triantafyllidis and J. A. Shaw, "Stability of Crystalline Solids – I: Continuum and Atomic Lattice Considerations", *J. Mech. Phys. Solids*, **54**, 161-192 (2006).

[8] R. S. Elliott, J. A. Shaw and N. Triantafyllidis, "Stability of Crystalline Solids – II: Application to Temperature-Induced Martensitic Phase Transformations in a Bi-Atomic Crystal", *J. Mech. Phys. Solids*, **54**, 193-232 (2006).

Developments in precision product manufacturing for laser-sintering

E. Westkämper[1], D. Tolksdorf[1]
[1]Institute of Industrial Manufacturing and Management (IFF)
University of Stuttgart, Germany

E. Westkämper, Nobelstraße 12, D-70569 Stuttgart, wke@iff.uni-stuttgart.de
D. Tolksdorf, Nobelstraße 12, D-70569 Stuttgart, det@iff.uni-stuttgart.de

ABSTRACT

Laser sintering is often used for design studies, prototypes and in tooling and moulding, i.e. in automotive and air industry applications. However, limitations in accuracy, surface quality, material properties, and process reliabilities still remain today and narrow the range of applications. Among other things, these reasons prevent clients in solving their needs. An add-on solution, in terms of an additional Micro-Mixing-Dosing (MMD)-system is proposed to be assembled into the laser sintering machine to accomplish a localized property distribution. This paper describes a new state-of-the-art route in manufacturing precision parts with various selected property profiles and an outlook in forecasting final product properties.

1. Introduction

Since the first stereolithography machine has become out of the market in 1982, the Rapid-Prototyping technology are often used for design studies, prototypes and for tooling and moulding applications for several years now. However, technical innovations in enhancing accuracy, surface quality, material properties and process reliabilities are still often not adequate and due to this fact the range of applications are limited. Also, the selection of materials for those systems has to be carefully carried out, since insufficient numbers of different materials has been tested. Specifically for laser-sintering machines, only a few metal and ceramic based powders are commercially provided by OEM´s.

2. Present State of Laser-Sintering Technology

2.1. Overview

The method for the solidification of powder material by using a heat source, such as a laser system was first invented and patented by Ciraud and Householder and further developed for building parts. In the year 1989 the first commercial prototype machine under the designation selective laser-sintering (SLS) was introduced. For the production of metal parts by the SLS process, three variants exist today: The indirect metal laser sintering (IMLS), laser melting (SLM) and the direct metal laser sintering (DMLS). With SLS a material mixture from a polymer and a metallic powder is used. The energy of the laser beam melts the polymer. This encloses the metallic powder and works as a binder component. This so-called Gruenling is post treated by thermal heating that the polymer is burned out. The body shrinks and a porous metal part remains, designated as the Braunling. This part can be infiltrated e.g. with a copper alloy finally [1]. The SLM process uses a single-phase metal material, e.g. stainless steel or tooling steel powders. The material is melted thereby locally and the part is generated directly

[2]. In contrast to this the third variant, by means DMLS, the part is made of metallic material components, by using a low melting binder component and a higher melting structural component. The energy of the laser beam melts the binder component during the process locally that the binder material flows around the structure component [3]. Quite common for all types of laser-sintering machines is building the part layer-by-layer by using homogenous material during the running cycle. The building cycle ends, until the last layer of the part is laser-sintered. The main application area for DMLS lies up till now in the production of function prototypes, the production of tools, e.g. for the plastic injection moulding and with the more temperature stable tool steel for light metal castings. Besides from these operational areas of rapid tooling at the present stage intensive investigations are continuing for direct production of metallic functional parts.

2.2. Process parameters

The most important factors of laser sintering process can be classified after Lohner and Niebling [4] into material, machine, part, laser, environment and exposure. Certain factor, i.e. laser or environment are coupled and thus depends of the system. Therefore these factors have to be taken into account for the system and materials. Beyond this process specific factors the selection of the material components, e.g. mean density or optical characteristics has to be considered and possibly adapted. The most important process controlled variables are:

- Laser energy,
- Layer thickness,
- Scan velocity,
- Beam offset and
- Exposure strategies.

From these characteristics the necessary energy per unit length and the surface energy can be derived. The laser energy and the power density are one of the most important process variables since by increasing the laser energy higher temperatures in the powder can be achieved. Thus the proportion of the liquid phase, the density and the mechanical strength of the laser-sintered part rises. The beam offset and the scan velocity have a crucial influence on the building speed, the strength of the part and beyond that it determines together with the particle sizes of the applied powders also the surface roughness of the horizontal surfaces. The surface quality of the vertical surfaces can be affected by a special exposure strategy.

The degree of the solidification by the laser beam and the resulting mechanical properties are essentially determined by the interaction time, the power density and the absorption behaviour of the powder. The general approach can be distinguished that the surface and volume in the part must fulfill different functions. The exposure of the differentiated ranges can be accomplished by optimized parameters and filling algorithms respectively. The surface and the volume ranges of the part can be adjusted up till now only insufficiently by different exposure strategies and exposure parameters in respect to the requirements. Moreover, the attainable characteristics of the part depend on the coordinate system of the building area and the orientation of the part.

2.3. Data flow chain

Before a manufacturing process can be initiated quite a few important pre-conditions have to be fulfilled, as shown in Fig. 1. From the definition of the surface normal the CAD data are converted into the standard triangle language (STL) format. With the standardized triangulation algorithm the volume model is approximated with a polygonal traverse draft. In the final step, the data file is transformed into usually equal distant layers, common known as slicing. The received data files contain geometrical information and generated supporting geometry of the part. It also contains layer information with defined layer thickness. The prepared layer file can then be fetched into the machine.

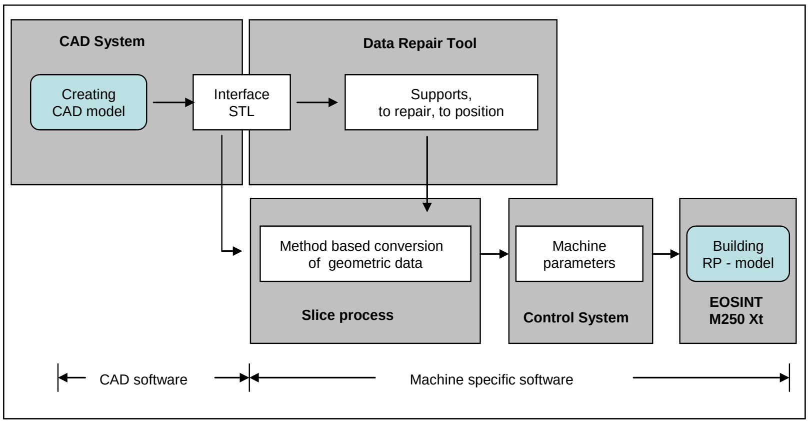

Figure 1: Data flow chain

3. Introducing the concept

The following concept, as illustrated in Fig. 2, introduces a possible route for precision product manufacturing. The main aim of this concept is to achieve localized defined multi-functional product property distributions.

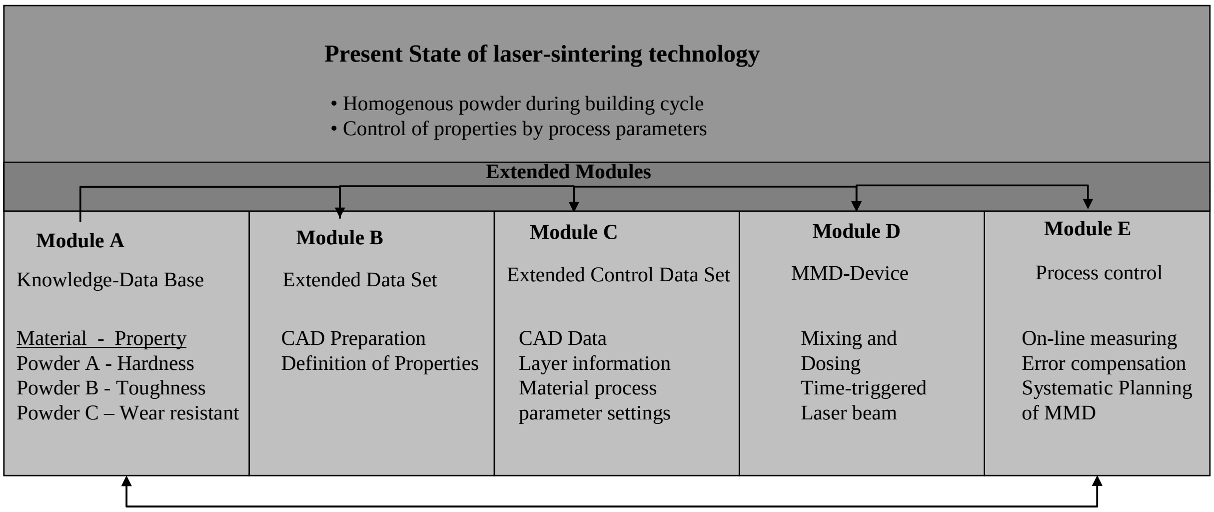

Figure 2: Concept with extended Modules

As shown in Fig. 2, the laser sintering process represents the initial core process, which is functionally extended by several modules. Usually technical parts, such as a bearing house needs different kind of mechanical properties depending on the target applications. It can be differentiated between structural, purely mechanical requirements and the functional requirements for the part. To be able to resist high changes in pressure demands of the rotary axle in the ball bearing the housing possess a very high-load carrying capacity and rigidity. Building the part by using laser sintering technology, i.e. the bearing house needs internal and outside basic supporting structures. The heat source introduced by the laser beam causes internal residual tensile stresses in the part, which must be reduced by these supporting structures. The internal and outside surface of this part may not exhibit any internal defects. From this fact, the supporting structures must possess a low strength, in order to easily remove it from the part surface. In addition the lateral surfaces of the bearing house must possess a smooth and wear-resistant surface in order to prevent a penetration of impurities and ensure thus a perfect function of the camps. At the bearing surfaces of the camps high static and dynamic alternating stresses arise by the rotations of the axes. In order to work against this changing load, materials with a high toughness and a high strength are demanded. Thus all specifications for this part are characterised in this simplified representation.

In order to select suitable powder materials a knowledge-based data base are necessary, as shown in Fig. 2, in Module A. Information regarding the correlation relationships between the materials, the laser beam and the mechanical-technological characteristics are stored and can be fetched on demand. According to the requirements for a part, a system dependent selection of materials is taken place.

On the basis of an analytic evaluation, an extended data file in the Module B from the knowledge-based data base is generated. This data file contains besides volume data also nominal data, such as the defined mechanical properties and the characteristics of the laser beam penetrating the powder materials. A suitable interface format from the computer-assisted application system is conceived and has to be developed for the extended data file.

After generating the new extended data set, a data transformation takes place into a control data set, which is shown in the Module C. The system dependent control data set contains the outline data of individual part layers, material-specific process parameters for the laser beam. The extended control data set is then passed to the MMD-device as well as at the existing re-coater system and needs to be synchronized with the optical and mechanical components. As shown in the Module D in Fig. 2, a proportioning and mixing of different powder material components in quantitative proportions are taken place with the time-triggered laser beam. The control settings from the MMD-device are linked to the control module, so that a fully automatic laser beam process is possible.

In order to achieve the product properties as previously defined, an on-line measuring and video monitoring system integrating into the machine is necessary, as referred to Module E in Fig. 2. It is therefore possible to determine and to balance deviations that arise during the building cycle and an uncontrolled dosing by previous planning can be excluded. These Modules are linked with the knowledge-based data base for setting up an adaptive self-learning knowledge system.

4 References

[1] Seefried, M.; Sigl, M.: Rapid-Technologien – Status Quo. In: Zäh, M.F. (Publisher); Reinhart, G. (Publisher): Rapid-Technologien. München: Herbert Utz 2002, (iwb Forschungsberichte 62), S. 1 - 23.

[2] Schwarze, D.: SLM Selective Laser Melting. In: Bayerische Laserseminare, Lasergestütztes Rapid Prototyping, 12.9.2002.

[3] Wohlers, T.: Wohlers Report 2000 – Rapid Prototyping & Tooling State of the Industry. Annual Worldwide Progress Report. Wohlers Associates, Inc., Fort Collins, Colorado, USA (2000).

[4] Niebling, Frank: Qualifizierung einer Prozesskette zum Laserstrahlsintern metallischer Bauteile. Bamberg: Meisenbach, 2005.

Ab initio DFT study on ferroelectricity on perovskite surfaces and in thin-film capacitors

Y. Umeno[1,2], **C. Elsässer**[3,1], **B. Meyer**[4], **P. Gumbsch**[1,3], **T. Shimada**[2], **T. Kitamura**[2]

[1]IZBS, Universität Karlsruhe, Kaiserstr. 12, 76131 Karlsruhe, Germany; [2]Dept. of Mechanical Engineering and Science, Kyoto University, Kyoto 606-8501, Japan; [3]Fraunhofer Institute for Mechanics of Materials IWM, Wöhlerstr. 11, 79108 Freiburg, Germany; [4]Theoretische Chemie, Ruhr-Universität Bochum, 44780 Bochum, Germany

ABSTRACT

Ab initio DFT calculations based on the local density approximation were performed to study (a) in-plane polarized ferroelectricity (FE) at $PbTiO_3$ (001) surfaces and (b) thin Pt/$PbTiO_3$/Pt capacitors with perpendicular FE, and their relation with the lateral lattice parameter. A significant influence of lattice parameter on ferroelectricity was found in both cases. At $PbTiO_3$ (001) surfaces, the in-plane FE in [110] direction is stable in both TiO_2 and PbO terminations, and it is enhanced by a larger lattice parameter. Antiferrodistortive (AFD) rotation emerging at the PbO-terminated surface is suppressed by a lattice expansion by the competition with FE. Perpendicular FE polarization in Pt/$PbTiO_3$/Pt films is suppressed by a lattice expansion. The critical thickness for ferroelectricity, whose stability is different for TiO_2 and PbO terminations of $PbTiO_3$, is obtained as a function of the lateral lattice parameter.

1. Introduction

Perovskite materials with ABO_3 structure have been attracting growing attention because their ferroelectricity paves the way for technological application such as MEMS/NEMS actuators or nonvolatile data-memory devices. As these devices are often realized in the form of thin epitaxial films grown on bulk substrates, the perovskite inherits the geometry of the substrate, and this can affect their ferroelectricity. In this work, ferroelectricity (FE) in $PbTiO_3$ surfaces and thin Pt/$PbTiO_3$/Pt capacitor films and its response to the in-plane lattice parameter were investigated by ab initio density functional theory (DFT) calculations.

2. Methodology

The ab initio DFT calculations in this work were based on the local density approximation (LDA).

The VASP package using the projector augmented wave (PAW) method [1] was employed for the surface model, which consists of 9 atomic layers of $PbTiO_3$ with (001) planes exposed to vacuum. Both surface terminations, TiO_2 and PbO of $PbTiO_3$, were studied. While (1x1) periodicity was applied for the former case, a c(2x2) periodicity model was employed for the latter because antiferrodistortive (AFD) rotation coexists with FE polarization in the PbO-terminated surface [2]. The boundaries are periodic and vacuum layers separate the top and bottom surfaces of $PbTiO_3$. With given lateral lattice parameters, the atomic coordinates are fully relaxed with centrosymmetry in the *z* direction to confine the ferroelectricity only in the lateral directions until all the forces are less than 10 meV/Å.

The thin Pt/$PbTiO_3$/Pt capacitors were studied with the mixed-basis pseudopotential (MBPP) code [3]. Close consistency of results by MBPP and VASP-PAW was confirmed. The ultrathin (001)-oriented $PbTiO_3$ film is sandwiched by 3 atomic layers thick Pt electrodes on both sides. Vacuum region is included to separate the top and bottom electrodes in order to enable efficient relaxation of atoms normal to films. Paraelectric (PE) and FE configurations are obtained by full relaxation of atomic positions with and without centrosymmetry in the z direction, respectively. Relaxation tolerance is the same as in the case of the surface model; i.e. all the forces less than 10 meV/Å.

3. Ferroelectricity at $PbTiO_3$ surface: In-plane polarization

Firstly we compared stabilities of polarizations in [100] and [110] directions. We found the polarization in [110] is energetically favored in both TiO_2 (FE) and PbO (FE+AFD) terminations (see Fig. 1(a)). The energy difference between the two FE directions per (1x1) cell is only 5.3meV for the former termination but it is 70meV for the latter. The preference for [110]-oriented polarization is independent of lateral lattice parameter.

Figure 1(b) shows the change in FE distortions with respect to lateral lattice parameter in the case of TiO_2-termination. Here, the magnitude of FE polarization is denoted by $\delta_{FE}=[\delta(M)-\delta(O)]/2^{1/2}a$, where δ is the atomic displacement of metal and oxygen. δ_{FE} increases smoothly with increasing lattice parameter, showing the enhancement of ferroelectricity by tangential stretch. On the other hand, ferroelectricity is suppressed under compression and vanishes at $a\approx3.77$ Å, indicating the existence of a critical compressive strain for ferroelectricity. When the surface is further compressed the ferroelectricity emerges again. This is accounted for by FE enhancement in bulk under extreme compression [4]. The response of δ_{FE} to the lattice parameter in the PbO-terminated surface is similar (see Fig. 1(c)). Under compression, however, δ_{FE} does not completely vanish because the polarization of the surface PbO layer tends to be less suppressed.

The change in the AFD rotation angle, ϕ_{AFD}, is shown in Fig. 1(d). AFD at the PbO-terminated surface with a=3.891 Å is found to be larger than that reported in Ref. [2] where only FE+AFD[100] was investigated. In the FE+AFD phase, FE and AFD compete with each other, resulting in the opposite responses of FE and AFD to lateral lattice parameter: increasing lattice parameter enhances FE and suppresses AFD.

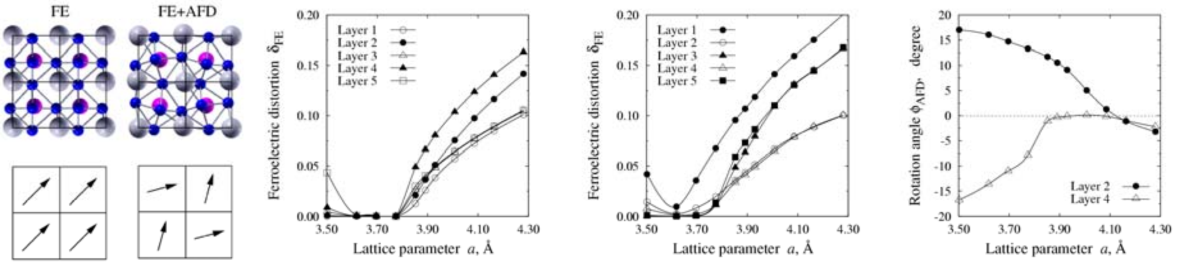

(a) [110] polarization (b) δ_{FE}, TiO_2(1x1) (c) δ_{FE}, PbO c(2x2) (d) ϕ_{AFD}, PbO c(2x2)

Figure 1. (a): Schematic view of [110] polarization at $PbTiO_3$(001) surface. (b) and (c): Ferroelectric polarization for TiO_2 and PbO terminations, respectively. (d): Antiferrodistortive rotation angle for PbO termination. “Layer 1” means the surface layer.

4. Ferroelectricity in thin Pt/PbTiO$_3$/Pt capacitors: Out-of-plane polarization

Figure 2 shows the energy difference between PE and FE, $\Delta E=E(\text{FE})-E(\text{PE})$, per perovskite unit cell versus lateral lattice parameter a for different film thicknesses, where, m denotes the number of unit cells in the PbTiO$_3$ layer. The limit for $m=\infty$ is also plotted which is obtained from bulk calculations imposing the respective value of a. ΔE strongly increases as a function of a, until it finally becomes positive, which means the loss of ferroelectricity. A pronounced difference in the stability of the FE states for the two different oxide terminations at the metal-oxide interface is found. For the PbO-terminated films ferroelectricity is supported up to a larger lattice constant than for the TiO$_2$-terminated films. We determined the critical thickness to stabilize a FE ground state of the PbTiO$_3$ films. At the theoretical equilibrium lattice constant of SrTiO$_3$ of a=3.845 Å, which is a typical substrate for epitaxial growth of perovskite films, we find that the m=4 PbO-terminated films is ferroelectric. The m=4 TiO$_2$-terminated films is paraelectric unless the lattice parameter is compressed below 3.815 Å. Using the extrapolation formula with the DFT results for m=2 and $m=\infty$,

$$\Delta E_{\text{est}}(m=4)=\{2\Delta E(m=2)+2\Delta E(m=\infty)\}/4,$$

we calculated an estimate of ΔE for the m=4 geometry. The result, plotted by short-dashed lines in Fig. 2, is almost identical to the DFT results for m=4. This indicates that only the outermost unit cell of the perovskite layer is significantly affected by the metal layer whereas the inner unit cells already possess the bulk-like properties. Hence, we can refrain from doing full DFT calculations for larger film thicknesses and use the extrapolation scheme instead. Extrapolating correspondingly the ΔE results from m=2 and m=4 to m=6 (long-dashed lines) and m=8 (dot-dashed lines) we find that at a=3.845 Å, ΔE has become negative for both surface terminations, indicating that the critical thickness of the TiO$_2$-terminated film is around m=6 or 24 Å.

Our DFT-LDA results are in contradiction to those by Sai *et al*. [5] based on DFT-GGA claiming the persistence of ferroelectricity for Pt/PbTiO$_3$/Pt films down to one unit cell, i.e., 4 Å. We performed GGA-based calculation using not only PW91 but also PBE functionals, which are in excellent agreement with the results of [5] The GGA and LDA give significantly different quantitative results for the stability of the FE states of the films. However, our results for the FE structure and stability of the bulk tetragonal PbTiO$_3$ phase confirm earlier reported results [6] that the GGA significantly overestimates the FE stability of PbTiO$_3$. The LDA results are therefore considered to be more reliable than the GGA results.

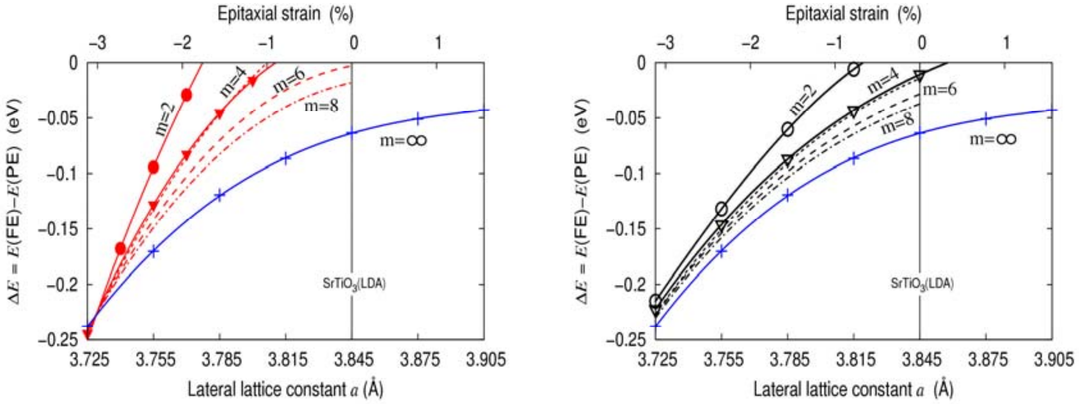

(a) TiO$_2$−termination. (b) PbO−termination.

Figure 2. Ferroelectric stability per perovskite unit cell as a function of PbTiO$_3$ thickness, m, and lateral lattice parameter, a.

Conclusion

We performed ab initio DFT calculations to elucidate ferroelectricity (FE) on perovskite surfaces and in thin-film capacitors. We demonstrate that the lateral lattice parameter significantly influences ferroelectricity in both cases. Increasing lateral lattice parameter, or in-plane tension, enhances FE parallel to the PTO_3 surfaces and suppresses FE normal to thin-film capacitors. Antiferrodistortive (AFD) rotation, which coexists with FE polarization on the PbO-terminated surface, shows the opposite response to the in-plane strain owing to competition between FE and AFD. In contrast, perpendicular FE in the thin-film capacitors is suppressed by in-plane tension. Profound differences in ferroelectricity depending on the termination layer, TiO_2 or PbO, are found both on the surfaces and in the thin-film capacitors. Critical thicknesses of ferroelectricity in the capacitors are theoretically evaluated depending on the perovskite thickness, the termination layer and the in-plane lattice parameter.

Acknowledgments

We acknowledge financial support for YU from the Grant-in-Aid for Scientific Research of the Japan Society of the Promotion of Science (JSPS) and the Center of Excellence for Research and Education on Complex Functional Mechanical Systems (COE program of the Ministry of Education, Culture, Sports, Science and Technology, Japan), for CE from the German Research Foundation (project EL 155/17-1 in the DFG priority program SPP 1157 "Integrated electroceramic functional structures"), and for PG from the European Commission (contract Nr. NMP3-CT-2005-013862 (INCEMS)).

References

[1] G. Kresse and J. Furthmüller, “Efficient iterative schemes for ab initio total-energy calculations using a plane-wave basis set”, Phys. Rev. B 54, 11169 (1996).
[2] C. Bungaro and K.M. Rabe, “Coexistence of antiferrodistortive and ferroelectric distortions at the $PbTiO_3$(001) surface”, Phys. Rev. B 71, 035420 (2005).
[3] B. Meyer, F. Lechermann, C. Elsässer and M. Fähnle, Fortran90 Program for Mixed-Basis Pseudopotential Calculations for Crystals, Max-Planck-Institut für Metallforschung, Stuttgart.
[4] I. A. Kornev, L. Bellaiche, P. Bouvier, P.-E. Janolin, B. Dkhil and J. Kreisel, “Ferroelectricity of Perovskites under Pressure”, Phys. Rev. Lett. 95, 196804 (2005).
[5] N. Sai, A.M. Kolpak and A.M. Rappe, “Ferroelectricity in ultrathin perovskite films”, Phys. Rev. B72, R020101 (2005).
[6] Z. Wu, R.E. Cohen and D.J. Singh, “Comparing the weighted density approximation with the LDA and GGA for ground-state properties of ferroelectric perovskites”, Phys. Rev. B 70, 104112 (2004).

Metal-ceramic interfaces from first-principles

Goran Wahnstrom[1], Mikael Christensen [1], Sven A. E. Johansson [1]

[1]Department of Applied Physics, Chalmers Univ. of Technology, 412 96 Goteborg, Sweden

Understanding stability and adhesion properties of interfaces between dissimilar materi- als is one of the most significant issues of contemporary materials research. Such inter- faces are prevalent in numerous industrial applications including e.g. heterostructure devices, corrosion protection, and thermal barriers, where their functions and properties are of vital importance. Theoretical tools such as density-functional theory (DFT) have during the last years been used to calculate interface energies of various metal-ceramic interfaces. However, almost exclusively in these studies, only the chemical part of the interface energy in the coherent interface approximation has been assessed. Real inter- faces are often more complicated. Here we will present results for interfaces in two different systems, sintered WC-Co cemented carbides [1] and ferritic steels [2].

WC-Co cemented carbides are a class of hard composite materials of great technologi- cal importance. The microstructure of the material consists of a hard WC grain skeleton embedded in a tough metal binder phase. The internal surfaces, grain boundary and het- erophase interfaces, determine to a large extent properties of the material. We have per- formed a quantitative analysis of WC grain shape using the density-functional theory (DFT) and transmission electron microscopy (TEM) [1]. The grains are found to be truncated triangular prisms and the measured grain morphology is adequately repro- duced by the ab-initio calculations. The difference in energy between interfaces formed by the two non-equivalent set of WC prismatic planes is due to the formation of stronger bonds with more covalent character between low coordinated W and Co atoms at one of the type of prismatic interfaces.

Precipitate strengthening in ferretic steels is of high technological importance. We have considered VN precipitates which form platelets in ferrite due to a small (2%) relative misfit parallel to the platelet and a appreciable (44%) misfit perpendicular to the platelet [2]. The small misfit (2%) results in a well-defined semi-coherent interface structure but despite the smallness of the misfit we demonstrate that the small deviation from coher- ency has a large influence on the interface energy. We also propose a simple procedure to investigate semi-coherent interfaces quantitatively by a combination of atomic-scale DFT calculations and elasticity theory.

[1] M. Christensen, G. Wahnstrom, C. Allibert, and S. Lay, Phys. Rev. Lett. 94, 066105 (2005).

[2] S.A.E. Johansson, M. Christensen, and G. Wahnstrom, Phys. Rev. Lett. 95, 226108 (2005).

Properties of ultra-dispersed lithium manganate

XingHua Xie[1], XiaoJie Li[2], Shilong Yan[1], Hongbo Wu[1] and Meng Wang[1]

[1]Department of Chemical Engineering, Anhui University of Science and Technology, Huainan 232001, China (xxh1963@163.com)

[2]State Key Laboratory of Structural Analysis for Industrial Equipment, Dalian University of Technology, Dalian 116024, China (dalian03@vip.sina.com)

ABSTRACT

Nanostructured spherical spinel lithium manganese oxide (LiMnO) with about 20nm in diameter was synthesized for the first time by explosive method. The water-solubility explosive was prepared using a simple facility at room temperature. The growth of lithium manganate via detonation reaction was investigated with respect to the presence of an energetic precursor, such as the metallic nitrate and the degree of confinement of the explosive charge. The detonation products were characterized by scanning electron microscopy. Powder X-ray diffraction and transmission electron microscopy were used to characterize the products. Lithium manganate with spherical morphology and more uniform secondary particles, with smaller primary particles of diameters from 10 to 20 nm and a variety of morphologies were found. Lithium manganate with a fine spherical morphology different from that of the normal spinel is formed after detonation wave treatment due to the very high quenching rate. It might also provide a cheap large-scale synthesis method. Explosive detonation is strongly nonequilibrium processes, generating a short duration of high pressure and high temperature. Free metal atoms are first released with the decomposition of explosives, and then theses metal and oxygen atoms are rearranged, coagulated and finally crystallized into lithium manganate during the expansion of detonation process.

Keywords: Nanostructures, lithium compounds, Manganites, detonation synthesis, epispastic polystyrene (EPS)

1. Introduction

A. Singhal et al. [1] thought that nanostructured intercalating electrodes offer immense potential for significantly enhancing the performance of rechargeable rocking chair. Shuhua Ma et al. [2] said that Spinel structure Li–Mn–O compounds are the most promising lithium ion insertion electrode materials for rechargeable lithium ion batteries because of a number of advantages over their alternatives. The split is presumably considered relating to the disproportionation dissolution of stoichiometric spinel intensified by the elevated temperatures in slightly acidic electrolyte due to residual water impurity. Li-Mn-O can selectively insert Li from an aqueous solution [3]. Mitsuharu Tabuchi et al. [4] reported that the excess Li could substitute the Mn ion on the 16d site in the spinel structure. And they introduced excellent cycling behavior for nonstoichiometric $Li_{1.0}Mn_{1.93}O_4$. Jong-Uk Kim et al. [5] investigated characteristics of charge/discharge cycling of LiMn2O4. I.J. Davidson et al. [6] reported that using solid-state reactions method, however, the powder preparation route is also quite complicated, for example, several times calcination and subsequent physical grindings. Moreover, its electrochemical properties are greatly dependent on its crystalline particle size [7]. Zhanqiang Liu et al. [8] synthesized nanostructured spherical spinel lithium manganese oxide (Li-Mn-O) with about 200nm in diameter for the first time by mild hydrothermal method, and studied systematically the influence of the reaction temperature and the time of formation of the nanostructures.

2. Experimental

After annealed at 450℃ for 6 hours, the detonation soot was studied by use of XRD.

Scanning electron microscopy (SEM) analysis was performed with JEOL JEM-1200EX for detonation synthesized Lithium manganate. XRD analysis was carried out on an XRD-6000 Shimadzu diffractometer using Cu Kα irradiation with input power of 50 kV and 150 mA. The divergence slit angle, scattering slit angle and receiving slit height were selected as 2, 2°, and 0.3 mm. The diffraction intensities were measured every step 0.028° for 1 s in the 2θ range from 10 to 80° at room temperature (293 K). The shape and size of the as-obtained particles were observed by transmission electron microscope (TEM, Tecnai G2 20 S-twin).

3 Results & Discussion

Fig. 1 shows an XRD pattern of the dynamically synthesized lithium manganate. We obtained a nanosized texture containing spinel lithium manganate. It is obvious that the Bragg reflection peaks of the dynamically synthesized Lithium manganate are broadened, which may result form small grain size and/or presence of microstrain. Here the mean grain size for detonation synthesized lithium manganate refers to the mean size of crystallites of polycrystalline particles. XRD analyses were conducted at a fixed temperature in the present study; a precise determination of the structural parameters need more experiments including both high temperature and low temperature experiments. The pattern represents the peak positions expected for $Li_{1.24}Mn_{1.72}O_4$ (JCPDS file n. 89-0753).

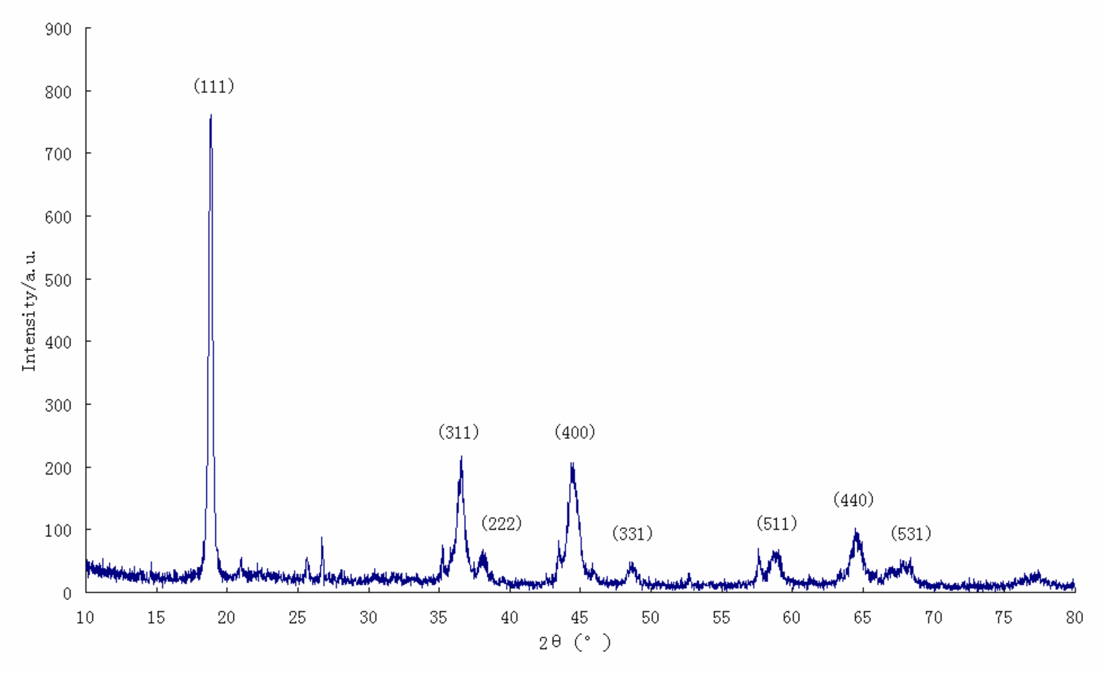

Fig. 1: XRD pattern of lithium manganate.

Although TEM picture shows smaller particles, which are aggregated further to form agglomeration, varied sizes, it is necessary to obtain the information regarding smallest primary particles. For this purpose, the TEM study and selected area electron diffraction (SAED) were shown in Fig. 2(a). The SAED pattern of zinc oxide nanometer powders shows a clear diffraction ring and varied points corresponding to the crystal planes of phase.

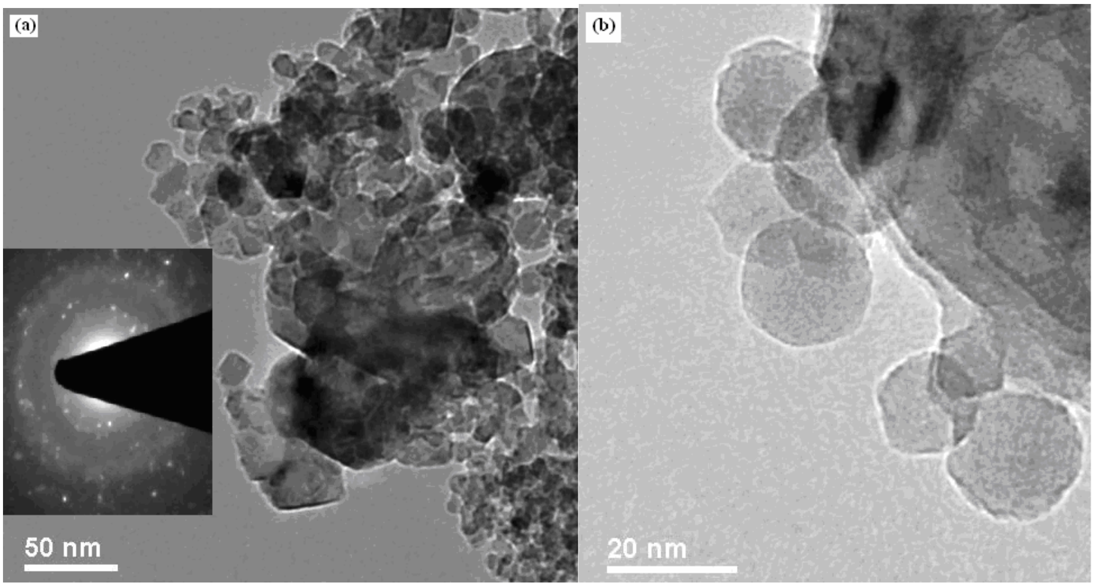

Fig. 2: TEM image of detonation synthesized lithium manganate.

4 Conclusions

Lithium manganate with a fine spherical morphology different from that of the normal spinel is formed after detonation wave treatment due to the very high quenching rate. It might also provide a cheap large-scale synthesis method. Explosive detonation is strongly nonequilibrium processes, generating a short duration of high pressure and high temperature. Free metal atoms are first released with the decomposition of explosives, and then theses metal and oxygen atoms are rearranged, coagulated and finally crystallized into lithium manganate during the expansion of detonation process. The inherent short duration, high heating rate (1010 – 1011 K/s) and high cooling rate (108 – 109 K/s) prevent the lithium manganate crystallites from growing into larger sizes and induce considerable lattice distortion.

Acknowledgements

The research described in this paper was made possible in part by the grant 10572034 from the Chinese National Natural Science Foundation and the grant from the Anhui Provincial Educational Office.

References

[1] A. Singhal, G. Skandan, G. Amatucci, F. Badway, N. Ye, A. Manthiram, H. Ye, J.J. Xu. Nanostructured electrodes for next generation rechargeable electrochemical devices. Journal of Power Sources 129 (2004) 38–44.
[2] S.H. Ma, H. Noguchi, M. Yoshio. An observation of peak split in high temperature CV studies on Li-stoichiometric spinel $LiMn_2O_4$ electrode. Journal of Power Sources 125 (2) (2004) 228-235.
[3] M. Morcrette, P. Barboux, J. Perrie`re, T. Brousse. $LiMn_2O_4$ thin films for lithium ion sensors. Solid State Ionics 112 (3-4) (1998) 249-254.
[4] M. Tabuchi, C. Masquelier, H. Kobayashi, R. Kanno, Y. Kobayashi, T. Akai, Y. Maki, H. Kageyama, O. Nakamura. Characterization of $Li_{1-\delta}Mn_{2-2\delta}O_4$ defect spinel materials by their phase transition, magnetic and electrochemical properties. Journal of Power Sources 68 (2) (1997) 623-628.
[5] J.U. Kim, I.S. Jeong, S.I. Moon, H.B. Gu. Electrochemical characteristics of $LiMn_2O_4$-polypyrrole composite cathode for lithium polymer batteries. Journal of Power Sources 97-98 (2001) 450-453.
[6] I.J. Davidson, R.S. McMillan, H. Slegr, B. Luan, I. Kargina, J.J. Murray, I.P. Swainson. Electrochemistry and structure of $Li_{2-x}Cr_yMn_{2-y}O_4$ phases. Journal of Power Sources 81–82 (1999) 406-411.
[7] S. Komaba, S.T. Myung, N. Kumagai, T. Kanouchi, K. Oikawa, T. Kamiyama. Hydrothermal synthesis of high crystalline orthorhombic $LiMnO_2$ as a cathode material for Li-ion batteries. Solid State Ionics 152–153 (2002) 311-318.
[8] Z.Q. Liu, W.L. Wang, X.M. Liu, M.C. Wu, D. Li, Z. Zeng. Hydrothermal synthesis of nanostructured spinel lithium manganese oxide. Journal of Solid State Chemistry 177 (4-5) (2004) 1585-1591.

Numerical Simulation of Hydrogen Isotopes Diffusion and Permeation in Stainless Steel

Huang Zhiyong[1], *Chen Changan*[1], *Liu Chongxian*[1]

[1]*China Academy of Engineering Physics, P.O. Box 919-71, 621900, Mian yang, China*

The effects of trapping and surface oxide layer on hydrogen isotope diffusion and permeation in stainless steel were analyzed. A modified hydrogen isotopes diffusion and permeation equation was put forward. The finite difference method was used to simulate the diffusion and permeation behavior of hydrogen isotopes for tubular or cylindrical geometry of stainless steel. By using gaseous permeation technique and etch technique, the hydrogen isotopes permeation flux and concentration distributions through a structure wall were measured. The experimental results were in accord with theoretical deduction. It was indicated that the modified hydrogen permeation equation can explain various hydrogen permeation curves and that the multi-dimensional diffusion problem can be simplified to some one-dimensional ones in numerical method.